The thermal properties, temperature structure and thermal evolution of the Eastern Ghats, India.

Andrew Richard Barker 2010
The University of Adelaide
Thesis submitted in partial fulfilment of the Honors degree of BSc Geology

I Abstract

The role of the portable gamma ray spectrometer has become a fundamental addition for gathering heat production data to constrain stochastic thermal modelling of the crust. Numerous sensitivity and calibration analyses have been undertaken to verify the validity of the output, and to aid in more efficient and effective use for future users. When applied to a heat flow study of the Eastern Ghats, it was established that the predominantly granulite-facies rocks such as khondalites, K-feldspar megacrystic granites and quartzo-feldspathic gneisses have high average heat production values of 3.76 ± 0.53μWm^{-3}, 2.79 ± 0.53μWm^{-3} and 5.49 ± 0.69μWm^{-3} respectively, whereas the UHT granulites have a low heat production of 0.69 ±0.23 μWm^{-3}. The contribution of uranium to the total heat production was considered low when compared to the input from thorium, which was almost four times higher. The average concentrations of thorium were also approximately fifteen times more than the concentrations of uranium. In this research, thermal conductivity testing was conducted to better constrain parameters for stochastic thermal modelling. Coupled with previous seismic studies, four crustal sections were analysed by one-dimensional steady-state finite difference models using the results of this project. Conclusions drawn from this study indicate that there is a possibility the Eastern Ghats is currently a UHT region, whereas burial of these high heat-producing rocks during orogenesis could have readily heated the crust to produce UHT granulite-facies metamorphism.

II Contents

I Abstract 2
II Contents 3
III List of tables 5
IV List of figures 5
V List of Appendices 6
1. Introduction 8
2. Regional background 10
3. Background theory and methods
3.1 Heat flow 12
3.2 Heat production 14
3.2.1 Background 14
3.2.1.1 Methods for estimating heat production 15
3.2.1.2 Depletion of heat-producing elements in granulite facies rocks 15
3.2.1.3 Crustal distribution of radiogenic heat producing elements 16
3.2.2 Measuring radiogenic heat production: Portable gamma ray spectrometers 16
3.2.2.1 Background 16
3.2.2.2 Calibration process 19
3.3 Thermal conductivity of rocks 19
3.3.1 Background 19
3.3.2 Estimating thermal conductivity 21
3.3.3 Measuring thermal conductivity 22
3.4 Numerical heat flow modelling 23
4. Results
4.1 Heat production 24
4.2 Thermal conductivity 25
4.3 Heat flow modelling 26
4.4 Gamma ray spectrometer calibration results 29
5. Discussion 30
6. Conclusions 32

7. Acknowledgments 34
8. References 35
9. Figure and table captions 40
10. Tables 49
11. Figures 53
12. Appendices 74

III List of tables

Table 3.1 - Energy range of detectable ragiogenic isotopes
Table 4.1 - Heat production values for the Eastern Ghats
Table 4.2 – Estimated thermal conductivity values
Table 4.3 – Thermal conductivity results from the Eastern Ghats
Table 4.4 – Input parameters for stochastic heat flow modelling (0Ma)
Table 4.5 – Input parameters for stochastic heat flow modelling (550Ma)

IV List of Figures

Figure 1.1 – Distribution of heat producing elements in the Earth's crust
Figure 1.2 – Thermal boundary layer between the asthenosphere and the lithosphere
Figure 2.1 – Geological map of the Eastern Ghats Belt
Figure 2.2 – Gridded heat flow map of India
Figure 2.3 – Transect of paths taken
Figure 3.1 – Graph depicting GRS problems
Figure 3.2 – Graph of initial GRS assays from the Eastern Ghats.
Figure 3.3 – Graph showing uranium cpm against uranium ppm, depicting GRS problems
Figure 3.4 – Graph depicting concentrations calculated for uranium against thorium
Figure 3.5 – Assays 189 & 190 from the Eastern Ghats
Figure 3.6 – Comparison of GRS data with XRF chemistry (uranium)
Figure 3.7 - Comparison of GRS data with XRF chemistry (thorium)
Figure 3.8 - Comparison of GRS data with XRF chemistry (potassium)
Figure 3.9 – Comparison of GRS data with Foden *et al*. (2002).
Figure 3.10 – Calibrated data comparison
Figure 3.11 – The effect of differing pressure and temperature on thermal conductivity
Figure 4.1 – Heat production comparison from the Eastern Ghats
Figure 4.2 – Uranium data from the Eastern Ghats
Figure 4.3 – Thorium data from the Eastern Ghats
Figure 4.4 – Heat production results of all lithologies from the Eastern Ghats.

Figure 4.5 – Probability density graph for Khondalites
Figure 4.6 - Probability density graph for Charnockites
Figure 4.7 - Probability density graph for quartzo-feldspathic gneiss
Figure 4.8 - Probability density graph for K-feldspar megacrystic granite
Figure 4.9 - Probability density graph for Quartzite
Figure 4.10 - Probability density graph for the UHT granulite
Figure 4.11 - Probability density graph for Gt/Sill/Crd gneiss
Figure 4.12 - Probability density graph for Gt/Sill gneiss
Figure 4.13 - Probability density graph for felsic gneiss
Figure 4.14 – Probability density graph (with histogram) of the total of all heat production values for the Eastern Ghats
Figure 4.15 – Surface heat production distribution of the Eastern Ghats
Figure 4.20 – Conductivity plot for the Eastern Ghats
Figure 4.30 – Seismic profile of SEGB
Figure 4.31 – Seismic profile of the Mahanadi Graben
Figure 4.32 – Crustal contribution profiles to surface heat flow
Figure 4.33 – Stochastic heat flow results from NEGB
Figure 4.34 – Stochastic heat flow results from SEGB
Figure 4.35 – Stochastic heat flow results from the Mahanadi Graben
Figure 4.36 – Stochastic heat flow results from SEGB
Figure 4.37 – Probability density graph of heat production @ 550Ma
Figure 4.38 – Stochastic heat flow results for SEGB @ 550Ma
Figure 4.39 – Stochastic heat flow results for SEGB @ 550Ma
Figure 5.1 – All stochastic heat flow results for the SEGB @ 550Ma
Figure 5.2 – All stochastic heat flow results for the SEGB @ 550Ma

V List of appendices

Appendix 1- Samples from the Eastern Ghats, India
A1.1 – Sample descriptions 76
A1.2 – Photographic record 80
Appendix 2 – Calibration of portable gamma ray spectrometers
A2.1 – Background and theory 86
A2.2 – Calibration 90

A2.3 – Comparative data 92
A2.4 – Sensitivity analysis 96
A2.5 – South Australian Heat Flow Anomaly 'ground correlation' 101
Appendix 3 – Heat production data 106
Appendix 4 – Thermal conductivity measurements and data
A4.1 – Sample preparation 109
A4.2 – Portable electronic divided bar principles 111
A4.3 – Calibration of the portable electronic divided bar 113
A4.4 – Taking thermal conductivity measurements 114
Appendix 5 – Error Propagation 119

1. Introduction

The thermal properties (thermal conductivity, thermal diffusivity and radiogenic heat production (RHP)) of rocks are essential when constraining the thermal structure and rheology of orogens (McKenzie *et al*. 2005, Stüwe 2007, Clauser 2006), and become a valuable tool when examining rocks from hand samples through to a crustal scale. Heat flow variations in old, tectonically stable regions essentially reflect variations in heat produced and conducted throughout the crust, whereas in tectonically active regions the measured heat flow includes effects of thermal transients (Roy & Rao 2003).

This project required raw data to be collected from the Eastern Ghats in the form of radioelement concentrations and thermal conductivity measurements of representative formations. This data was analysed by converting elemental concentrations into heat production values, and in addition to thermal conductivity readings, were utilised in stochastic heat flow modelling.

Present radiogenic heat production by the earth is 18 TW, and currently radiogenic heat contributes to 41% of the Earth's total surface heat flow (Hofmeister & Criss 2005, Clauser 2006). The major radiogenic heat producing elements (RHPE) uranium, thorium and potassium, are used when determining the total heat production for a sample. Ray *et al.* (2003 & 2008) define heat production as:

$$HP(\mu Wm^{-3}) = 10^{-3}\rho(0.035C_K + 0.097C_U + 0.026C_{Th}) \qquad \text{(Equation 1.1)}$$

Where C_K, C_U and C_{Th} denote the concentration of each element in wt% and ppm, and ρ is the density in kgm^{-3}. Uranium, thorium and potassium are incompatible large-ion-lithophile elements (LILE), and are strongly partitioned into the crust and residual mantle (Figure 1.1). Crustal radioactivity contributes a major component to surface heat flow values (Gupta *et al*. 1982), and the abundance of RHPE generally decreases

with increasing depth due to differentiation of minerals throughout the crust (Abbady *et al*. 2006). The Earth's mantle contains about two orders of magnitude less RHPE than the crust, but it is this radiogenic heat that has an important influence on enhancing convective flow, and therefore the heat flux from the mantle to the lithosphere (Figure 1.2). Crustal stabilisation requires differentiation of the RHPE, and is a self-regulating system due to the differing vertical distribution of high heat production, which gives rise to elevated temperatures in the lower crust favouring melting and therefore differentiation of RHPE (Jaupart & Mareschal 2007).

Vilá *et al*. 2010 has identified that one of the most difficult yet critical tasks in thermal modelling is assigning reliable RHPE values to various lithological units. Of particular relevance to this study - granulite facies rocks, which comprise a large portion of the mid to lower crust, are important in heat flow studies as they contribute a significant component to crustal heat flow. Many authors have examined the RHPE concentrations in granulites and have reached the conclusion that in general there is an increasing depletion in RHPE with increasing metamorphic grade (Kumar & Reddy 2004, Kumar *et al* 2007, Roy *et al.* 2008), although there are some important exceptions in the Australian Shield (Ray *et al*. 2008), the Eastern Ghats (Kumar *et al*. 2007) and Brazil (Ray *et al*. 2003). The Eastern Ghats RHPE concentrations are somewhat of an enigma, and their high heat production may be due to the high concentrations of thorium-rich monazites (Ray *et al*. 2008).

Quantifying the thermal properties, temperature structure and evolution of the Eastern Ghats is the focus of this study; in particular this study aims to:

1) Develop methodologies to determine the thermal structure and evolution of the crust. Specifically to accurately measure the heat production and thermal conductivity, and then numerically model the thermal structure of the crust.

2) Apply these methodologies to understand the origin and evolution of the high geothermal gradient in the Eastern Ghats Orogen.

3) To understand hot orogens; with the eventual aim of using this data set in the identification of potentially exploitable geothermal resources in the region.

2. Regional Background

The Eastern Ghats Belt (EGB) is a deeply eroded Mesoproterozoic orogenic belt that is juxtaposed against the Dharwar, Bastar and Singhbhum cratons via the Sileru Shear Zone (SSZ) (Bhattacharya 1996 & 1997, Kumar *et al.* 2007) (Figure 2.1). It is 900km in length and has a varying width between 50km in the south to a maximum of 300km in the north (Chetty 2010). It has exposed granulite facies rocks such as charnockites, khondalites, metasedimentary and metaigneous rocks, plus a host of intermediate to mafic gneisses, with less abundant mafic granulites. Chetty (2001) identifies a collage of juxtaposed tectonic domains that are delineated by a network of major shear zones, which have been reactivated during the late Neoproterozoic. Alternatively, Kumar *et al*. (2007) divides the EGB into north and south domains, split by the Vamsadara Shear Zone (VSZ) and dissected by the Godavari and Mahanadi Grabens, in view of the fact that Nd model ages of the granulites from the north are largely Proterozoic (2.2 – 1.8 Ga), whereas the Southern Granulites have Archaean (3.9 – 2.5 Ga) Nd model ages.

Various tectonometamorphic events have been described in the Eastern Ghats region, including alkaline plutonism associated with rifting at 1.3 -1.5 Ga, two Grenvillian metamorphic pulses at 1 – 1.1 Ga, and metamorphism linked with the assembly of Rodinia (.94 - .98 Ga) coeval with 940 Ma plutonism (Bhattacharya

1997, Chetty 2001, Das *et al*. 2008, Mukhopadhyay & Basak 2009, Chetty *et al*. 2010, S. Marshall pers. comm., 2010). The orogenic event that resulted in juxtaposition of the EGB against the Archaean cratons has been the subject of considerable examination, with several authors suggesting the thrusting of 'hot' granulites of the EGB over the 'cold' Archaean cratons to the west, occurred during the Pan-African orogeny (550 Ma) which assembled Gondwana (Chetty 2001, Kumar *et al*. 2007, Das *et al*. 2008, Mukhopadhyay & Basak 2009, Chetty *et al*. 2010). Chetty (2010) suggests the transpressive nature of shear zones, the extrusion of granitic material in the axial zone, high angle thrusting and the geometry of the shear zones all combined, make the terrane a classic orogen of oblique convergence during the Neoproterozoic. During the orogenic event, the middle and lower crust reached some of the hottest crustal temperatures (>1000^{o}C) observed in the world, where high concentrations of radioactive elements in the metasedimentary rocks are thought to have contributed to the high geothermal gradients (Dasgupta *et al.* 2010) (Figure 2.2). Understanding how the crust in this region attained such high temperatures (> 900^{o}C) is a key question for our understanding of ultra-high temperature (UHT) orogens globally.

Extensive studies of heat production and heat flow in the Indian shields and Proterozoic basins have been undertaken (Rao *et al*. 1970, Rao & Rao 1980, Gupta 1982, Rao & Rao 1983, Roy & Rao 2000, Ray *et al*. 2003, Roy & Rao 2003, Kumar & Reddy 2004, Manglik 2006, Rai & Thiagarajan 2006, Kumar *et al*. 2007, Ray *et al*. 2008, Roy *et al*. 2008 and Kumar *et al*. 2009), which have indicated that there is high mantle heat flow in the Southern Granulite Terrain (15 – 35 mWm^{-2}), low mantle heat flow in the Archaean Dharwar craton (7 – 12 mWm^{-2}), and relatively high radiogenic heat production in the Eastern Ghats Belt (≈ 2.9 μWm^{-3}). This study will further

constrain the crustal scale heat flow of the Eastern Ghats, and for the first time thermal conductivity measurements of rocks from the Eastern Ghats will allow for more accurate predictions of the thermal structure and evolution of this area.

Therefore, I have conducted a study of the heat production and thermal conductivity in each major lithology, and determined whether mineralogical differences within the lithologies contribute to differences in thermal conductivity (and anisotropy of conductivity). Having constrained the thermal properties of the region, I present one-dimensional steady-state stochastic models to constrain the conditions necessary to produce the metamorphic conditions observed during the Pan-African reconstruction.

The location of this study is two transects located in Andhra Pradesh, India, from Vishakhapatnam to Araku, and Vizianagaram to Paderu (Figure 2.3), and fieldwork was undertaken in January 2010.

3. Background Theory and Methods

3.1 Heat Flow

Fourier's law of heat conduction states that in one dimension and at steady state:

$$q = -k\frac{dT}{dz} \qquad \text{(Equation 3.1)}$$

In this equation q is heat flow measured in Wm^{-2}, k is thermal conductivity measured in $Wm^{-1}K^{-1}$, and the ratio dT/dz is the temperature gradient measured in KKm^{-1}. Heat flow is therefore a product of thermal conductivity and the temperature gradient. Following Stüwe (2007), this equation can be expanded to include heat production, advection and time dependant temperature:

$$\frac{\partial T}{\partial t} = \kappa\left(\frac{\partial^2 T}{\partial z^2}\right) + u\left(\frac{\partial T}{\partial z}\right) + \left(\frac{S}{\rho C_p}\right) \quad \text{(Equation 3.2)}$$

Where κ is the thermal diffusivity ($k/\rho C_p$), u is the transport velocity, S is the RHP in Wm^{-3}, and ρC_p are the petrophysical properties density and specific heat capacity respectively. This equation (3.2) is the basis for heat flow calculations, and it states that heat flow is governed by thermal conductivity and RHP; both of which will be determined in this project. I will be assuming zero advection in this project, hence this equation simplifies to:

$$\frac{\partial T}{\partial t} = \kappa\left(\frac{\partial^2 T}{\partial z^2}\right) + \left(\frac{S}{\rho C_p}\right) \quad \text{(Equation 3.3)}$$

Therefore at steady state when $\frac{\partial T}{\partial t}$ equals zero:

$$\kappa\left(\frac{\partial^2 T}{\partial z^2}\right) = -\left(\frac{S}{\rho C_p}\right) \quad \text{(Equation 3.4)}$$

From equation 3.4 it becomes apparent that three parameters are necessary to accurately constrain the thermal structure of the crust at depth in a region: (1) regional heat flow measurements, (2) thermal conductivity of the crust and (3) estimates of crustal RHP.

Crustal contributions to surface heat flow can be determined by characterising lithological units, and using exposed outcrops to aid in constraining the heat production distribution throughout a region. Heat production of surface geology varies extensively, and lateral heterogeneity in the crust cannot be described suitably by a simple one-dimensional numerical model. Better estimates of crustal contributions to surface heat flow in thermal equilibrium can be better constrained by using dense and reliable heat flow coverage, a cross section of lithological units, and an accurate heat production data set (Roy & Rao 2003, Jaupart & Mareschal 2007).

In this project my principal focus is on the use of recently acquired portable gamma ray spectrometers to estimate the crustal heat production. I will then apply the results to a detailed study of the thermal structure of the Eastern Ghats examining the crustal-scale heat flow. Thermal conductivity measurements collected on samples from India allow constraints to be placed on the thermal structure and evolution of the crust in this region of elevated surface heat flow, with a particular focus on the evolution of the crust during UHT granulite facies metamorphism.

3.2 Heat production

3.2.1 Background

From equations 3.2 and 3.4 it is clear that an important parameter in determining the crustal temperature is *S*, the volumetric heat production, which depends on concentrations of RHPE (equation 1.1). In choosing averages of concentrations for RHPE values to represent rock units involves large uncertainties due to rock classification imposing arbitrary subdivisions in a continuous medium, and consequently variations of heat production are due to these subdivisions. Rock classification is usually based on vague interpretations, and is usually too condensed; hence the only true method for assigning RHPE abundances is by mineralogy, which is usually too broad for most models (Vilá *et al*. 2010). For all intents and purposes, in this project I will be dividing concentrations of RHPE into lithological units.

The distribution of RHPE in minerals is as follows: Uranium and thorium are concentrated in zircon, monazite, allanite, apatite, xenotime and sphene. Potassium is concentrated in micas and K-feldspar (Kumar & Reddy 2004, Kumar *et al*. 2007, Vilá *et al*. 2010).

3.2.1.1 Methods of Estimating heat production

The distribution of RHPE can be found by using an empirical relationship with p-wave velocities (Rao & Rao 1983, Rai & Thiagarajan 2006), however this formula becomes obsolete in the upper crust because of its heterogeneous nature. Vilá *et al*. (2010) refute this claim, suggesting that there is only a general decrease in RHPE with depth, and by linking p-wave velocities to lithological units and therefore RHPE estimates, results in great uncertainties. Hence, in this study I will adopt the 'block distribution' for the vertical division of RHPE, and determine radioelemental abundances using gamma ray spectrometry analysis in the field, coupled with seismic data, and comparisons with X-ray Fluorescence (XRF) chemistry analysis in the lab (e.g. Roy *et al*. 2008).

3.2.1.2. Depletion of heat-producing elements in granulite facies rocks

The evolution of the continental crust into a more radiogenic-rich composition is due to the sink of dense RHPE depleted crustal material into the upper mantle, along with intrusions of melts where RHPE are concentrated.

The formation of granulites in the lower crust is accomplished by large scale streaming of dry metamorphic fluids that have displaced H_2O-rich fluids from the lower crust to the upper crust. These H_2O-rich fluids purged from the lower crust facilitate migration of RHPE to the middle and upper crust, and result in a strong depletion in LILE of the lower crust (Kumar & Reddy 2004). Vilá *et al*. (2010) also suggests that granulite metamorphism aids in this depletion by breaking down accessory mineral phases, and causes the partial melting and removal of melt fluids. This depletion of RHPE causes the subsequent low heat production values that are now established for granulites.

3.2.1.3. Crustal distribution of radiogenic heat producing elements

The distribution of RHPE in the crust is often assumed to follow a model of continuous exponential reduction in RHPE with depth. This model states that there is no discontinuity in the heat production of the crust (Gupta & Roy 2007 and Stüwe 2007). Ketcham (1996b) utilises the reconstruction of metamorphic core complexes of the upper and middle crust of the Arizona Basin and Ranges to conclude that exponential and 'block' models are sufficient for estimates of heat production in the upper and middle crust, but inadequate for levels below 15-20km.

3.2.2. Measuring RHP: Portable Gamma Ray Spectrometers

3.2.2.1 Background

Portable gamma ray spectrometers (GRS's) are commonly used to map the radioelement concentrations of in-situ rock formations to gain an insight into the RHP and possible heat-flow structure of the subsurface geology (IAEA 2003, Serra 1984b). The initial intention of this project is to understand the processes undertaken by the Radiation Solutions Inc. RS-230 BGO Super-spec GRS when calculating radioelement concentrations, in part due to concern of anomalously low Uranium assays obtained from an instrument in the Eastern Ghats, India (Figure 3.1). This is of the upmost importance as verification of the data output from the University of Adelaide's GRS's is imperative for the confident interpretation of the results and their use in further studies.

Gamma Ray Spectrometers measure the intensity and energy of gamma radiation, enabling the source of the radiation to be diagnosed (IAEA, 2003). Only radiogenic isotopes from the decay series of ^{40}K, ^{238}U, ^{235}U and ^{232}Th emit gamma

rays of sufficient energy and intensity to be measured by a GRS (Table 3.1). Neither ^{238}U nor ^{232}Th emit gamma rays during radiogenic decay, however gamma ray emissions from the decay of intermediate daughter products in the complex decay series from U or Th to Pb via the decay of ^{214}Bi and ^{208}Tl respectively, are measurable. Therefore resultant concentrations determined by GRS's are the 'equivalent' concentrations (IAEA 2003, Grasty & Minty 1995).

Several complications exist in the determination of radio-elemental concentrations from gamma ray spectrometry: 1) secular disequilibrium in the decay series, 2) density and thickness of weathered material covering the rock sample, 3) varying regional background, 4) variations in cosmogenic background (usually above 3.0MeV), 5) instrument 'dead-time' and 6) interference of spectra (corrected by using stripping ratios calculated from calibration pads) (Serra 1984a, Serra 1984b, Løvborg & Mose 1987, Grasty & Minty 1995, Groves & Campbell 1995, Minty *et al.* 1997, IAEA 2003, Minty *et al*. 2009). These complications are covered in appendix 2.

Calibration of the GRS's is necessary due to questions raised over the validity of data collected in India in January this year, of which is now highlighted. Figure 3.2 is a graph depicting uranium concentrations against the counts per minute (cpm) ratio of uranium to thorium, and evidentially there is zero uranium for any ratio of counts under approximately 0.3 counts per minute (cpm) U/Th. This data is perturbing, as it is suggesting that even though there are counts of gamma radiation being detected in the uranium region of interest (ROI) by the GRS, these are not being converted into a concentration by the software of the instrument. Figures 3.3 and 3.4 also represent alarming findings, whereby even small counts of uranium are not being converted into concentrations, and that there were very rare thorium assays of zero when compared to the many zero uranium readings. Furthermore, Figure 3.5 is demonstrating the

discrepancies in the software's ability to calculate concentrations. In both spectral signatures it is displaying 4cpm of uranium, however only one assay resulted in an actual concentration of 0.2ppm uranium. These results alone are enough to warrant the calibration.

The significance of this project is to test the parameters defined in the instruction manual, and define a robust method for analysing rocks with the portable GRS. I will be conducting experiments to determine the ideal and minimum source size, the attenuation distance of the gamma rays from the source to the GRS, and ascertain exactly how the GRS software calculates concentrations from the cpm. Geoscience Australia in Canberra has calibration pads for portable GRS's to validate the instruments sensitivity, following which I will produce instructions that will aid in determining the steps in converting cpm to ppm. I will contribute to the current knowledge in this field by producing comprehensive directions on how to process and interpret data from the portable GRS, which has not yet been embarked upon by the University of Adelaide. The significance of this for future users and University of Adelaide's geothermal research is highly important, and can be applied to possibly examining the heat production of core samples held in various repositories in South Australia.

3.2.2.2 Calibration process

A positive outcome with calibration of the GRS can stipulate that in the future it can be used without questioning the data integrity, which also means previous sampling can be known to be correct or incorrect/corrected. My data pertaining to this potential problem has been compared with previous chemistry and GRS data collection, and correlations being drawn from Kumar *et al.* (2007) in the Eastern

Ghats, and Foden *et al.* (2002) from South Australian localities (Figures 3.6 – 3.10). A thorough discourse on the methods and mathematics of the calibration process is set out in Appendix 2 and 5.

3.3 Thermal Conductivity of rocks

3.3.1 Background

Thermal conductivity is a petrophysical property and depends on many variables within the rock. The thermal conductivity ultimately characterises the proportionality of the temperature gradient on heat flow, and is a fundamental control on temperature at depth in the crust. The thermal diffusivity is derived from thermal conductivity divided by the petrophysical properties of the rock; density and specific heat capacity:

$$\kappa = \frac{k}{\rho C_p} \qquad \text{(Equation 3.5)}$$

The interior heat of the earth is transmitted to its surface by three mechanisms: radiation, advection and conduction. The extent of the lithosphere can be defined in two ways, with one of them being the thermal lithosphere; the boundary between advection in the mantle and conduction in the lithosphere (Clauser & Huenges 1995, Clauser 2006, Jaupart & Mareschal 2007, Hofmeister *et al*. 2007, Stüwe 2007, Whittington *et al*. 2009) (Figure 1.1). Even in the absence of advection, heat production and lateral hydrothermal circulation, the temperature gradient cannot remain constant due to variable thermal conductivity, and boundary conditions. Where two contiguous domains of differing thermal conductivity coincide, heat refraction is said to occur (Mildren & Sandiford 1995, Stüwe 2007), and can be understood by identifying the following equation:

$$-q = k_1 \frac{\Delta T_1}{\Delta z} = k_2 \frac{\Delta T_2}{\Delta z} \quad \text{(Equation 3.6)}$$

This equation denotes that if the conductivities *k*1 and *k*2 are different, the temperature gradient of the rock with the higher conductivity must be lower, and vice versa. Rarely would thermal conductivity in a given lithology remain homogeneous, therefore this phenomenon would occur regularly.

The thermal conductivity of a rock depends on its mineralogy, grain size, depositional environment, layer anisotropy, porosity, pore fluids, pressure, temperature and fabric directions (Clauser & Huenges 1995, Correia & Jones 1996, Clauser 2006, Matthews & Beardsmore 2007, Hofmeister *et al*. 2007, Matthews 2009). Porosity plays a large effect on thermal conductivity, as the two major forms of heat transport are via phonons and radiative heat transport by photons (McKenzie *et al.* 2005 and Hofmeister *et al*. 2007). The transport of heat by scattering of phonons within each individual mineral grain is termed lattice conductivity, and describes the increase of phonon density with increasing temperature, resulting in a decrease of the free path between collisions. Heat is additionally diffused radiatively by grain-to-grain progressive absorption and re-emission of photons down a temperature gradient.

The thermal conductivity for many rocks is isotropic, however for metamorphic and sedimentary rocks that display anisotropic structure, the thermal conductivity becomes anisotropic concordantly. Anisotropy exists at all scales from individual crystals to the crustal scale (Clauser 2006).

3.3.2 Estimating thermal conductivity

Numerous authors identify methods to estimate thermal conductivity from various mixing models that are aimed at estimating the thermal conductivity of a rock without physically measuring it. This practice is commonly used in heat flow

modelling where the lithology has roughly been ascertained from seismic velocities. The modal mineralogy and/or saturating fluids should be identified or estimated, because minerals due to their well-defined composition, exhibit much smaller variances in thermal conductivity than rocks (Clauser & Huenges 1995, Vasseur *et al*. 1995, Clauser 2006).

Many mixing models are proposed in the literature (see Clauser 2006 for summary), however the most common indirect methods used are the arithmetic, harmonic and geometric mean. Similar to hydrology flow measurements, the arithmetic mean (k_{ari}) is used when the mineral lineation is parallel to the heat flux, the harmonic mean (k_{har}) is used for a perpendicular flow, and the geometric mean (k_{geo}) is an intermediate value in between both. These three means are defined by:

$$k_{ari} = \sum n_i . \lambda_i$$

$$k_{har} = \frac{1}{\sum \frac{n_i}{\lambda_i}} \qquad \text{(Equations 3.7, 3.8 \& 3.9)}$$

$$k_{geo} = \prod \lambda_i^{n_i}$$

Where λ_i is the mineral thermal conductivity, and n_i the volume fraction of the *i-th* phase, relative to the total volume. Johnson & Wenk (1974) and Matthews (2009) point out that the thermal conductivity parallel to layering can be up to three times higher than the thermal conductivity perpendicular to it. Quartz and feldspar contents have a strong influence on the overall thermal conductivity, as quartz has a high thermal conductivity (7-10$Wm^{-1}K^{-1}$), whereas feldspars have a low thermal conductivity (2.3$Wm^{-1}K^{-1}$) (Horai 1971, Clauser & Huenges 1995, Ray *et al*. 2006).

A thermal conductivity measurement at room temperature and pressure will not necessarily dictate the coinciding conductivity at depth, where temperatures and

pressures are higher (Wong & Brace 1979). Clauser & Huenges (1995) propose an empirical relationship for temperature dependant thermal conductivity:

$$k(T) = \frac{k(0)}{1.007 + T.(0.0036 - \frac{0.0072}{k(0)}} \qquad \text{(Equation 3.10)}$$

Where $k(T)$ is the thermal conductivity at a given temperature, and $k(0)$ is the thermal conductivity at the surface. At temperatures below 500^{o}C, heat transfer in crustal rocks is mainly due to phonon conduction, which is inversely proportional to temperature. At higher temperatures, radiative heat transfer starts playing a role, and conductivity is proportional to T^3 (Hofmeister *et al*. 2007). Pressure also plays a key role in thermal conductivity, as fractures and microcracks which develop during stress release begin to close with increasing pressure; thus reducing thermal contact resistance as well as porosity (Clauser & Huenges 1995, Abdulagatov *et al*. 2006, Abdulagatova *et al*. 2009) (Figure 3.7).

3.3.3 Measuring thermal conductivity

Thermal conductivity measurements were conducted using a Portable Electronic Divided Bar (PEDB) apparatus supplied by Torrens Energy Ltd at the University of Adelaide. Before measurements took place, rock samples had to be prepared and the device calibrated, which is the topic of discourse in appendix 4. Twenty samples were measured at the University of Adelaide, and at NGRI in India, where measurements were made parallel and perpendicular to foliation.

3.4 Numerical Heat Flow Modelling

When conducting crustal scale heat flow calculations, certain constraints need to be identified to gain acceptable results. Dense and reliable surface heat flow values

need to be gathered from boreholes in the region to be studied. Additionally, a high-quality data set of heat production and thermal conductivity for each lithology constituting the crustal layers is required, along with accurate mapping of regional geology. Depending on the objective of the study, Moho heat flow can be estimated, or would likely be the result of the heat flow study.

Before numerical modelling is commenced, questions need to be identified in order to gain an answer through stochastic modelling. Questions such as:

- What is the objective of the study (ie looking for a geothermal reservoir)?
- How thick is the crust, how many layers are there, and what is the thickness of each layer going to be?
- What is the temperature at the mantle, and the distance to the asthenosphere?
- What is the Moho temperature?
- Will anisotropy of thermal properties be included?

The modelling approach in this study was undertaken using MATLAB R2008, which utilised one-dimensional steady-state finite difference models with a constant temperature upper boundary condition, and either a constant heat-flux or constant temperature lower boundary condition.

4. Results

4.1 Heat Production

The Eastern Ghats heat production data is summarised in Table 4.1 and Figures 4.1 – 4.15, with complete details provided in appendix 3; and is compared to data acquired in similar studies by Kumar *et al*. (2007) and Palmer (2009).

The quartzo-feldspathic gneiss had the highest average heat production of 5.49 ± 0.69 μWm^{-3}, which was due to very high levels of thorium contributing to heat generation. In fact, the Th/U ratios for all rocks assayed averaged approximately 14.3, which is substantially high when compared to the average value of 4 (Kumar *et al*. 2007). Khondalites also had relatively high RHP values, with an average of 3.76 ± 0.53 μWm^{-3}, and an average Th/U ratio of 15. These values are extremely high, suggesting there is obvious depletion of uranium when compared to thorium, and this observation also questions the general belief that granulites characteristically have low heat production. As expected, the mafic UHT granulites had low overall RHP of 0.69 ±0.23 μWm^{-3}.

The relative probability graph (Figure 4.14) displays a bimodal distribution of heat production with an average RHP value of 3.46 μWm^{-3}, which most likely correlates to the dominant two lithologies of charnockites and khondalites in the region.

There was no evident pattern of RHP distribution found along the transects (Figure 4.15). Heat production can be extremely heterogeneous within the one outcrop, and this small-scale precedent is clearly mimicked over the region, even though the lithological units have definitive boundaries.

4.2 Thermal Conductivity

Thermal conductivity testing on the Eastern Ghats samples was undertaken at the Mawson Laboratories at the University of Adelaide, plus there were ten samples sent to NGRI in Hyderabad, India for thermal conductivity testing. Being the first study to determine the thermal conductivity of rocks from the Eastern Ghats, there were no previous studies to compare results to, only similar lithologies in different regions, which were not compared to.

Data is summarised in Table 4.2, 4.3, Figure 4.20 and appendix 4. All samples excluding the massive charnockite, showed varying degrees of foliation and therefore anisotropy of their thermal properties. The major lithological units - Khondalite and Charnockite, had conductivities of 2.49 ± 0.06 $Wm^{-1}K^{-1}$ (perpendicular to foliation) and 2.92 ± 0.21 $Wm^{-1}K^{-1}$ (parallel to foliation) and 2.40 ± 0.2 $Wm^{-1}K^{-1}$ respectively. The lowest conductivity was seen in the K-feldspar megacrystic granite (1.96 ± 0.09 $Wm^{-1}K^{-1}$ perpendicular to foliation, and 2.43 ± 0.33 $Wm^{-1}K^{-1}$ parallel to foliation), which subscribes to the notion that the high modal proportion of feldspars in this rock resulted in this low conductivity.

Anisotropy of thermal conductivity was clearly observed in all foliated rocks, with parallel to perpendicular ratios up to 1.54 (quartzo-feldspathic gneiss). The lowest anisotropy was observed in Khondalites (1.18), possibly due to the ambiguous foliation; only on rare occasions was alignment of the K-feldspar megacrysts noticed.

It is quite evident that the measured conductivities are somewhat lower than the estimated conductivities derived from the mixing models of Clauser & Huenges (1995) and Horai (1971). This is most probably due to two reasons. (1) The thermal expansion effects (temperature and pressure) of conductivity result in a decreased

observed conductivity at the surface. (2) The contact between the rock sample and the brass plates may not have been perfect (see appendix 4 for details).

4.3 Heat flow modelling

Four seismic profiles were used in stochastic heat flow modelling; and their localities used in this study are located in Figure 2.1. Two seismic sections were used from Kumar *et al*. (2007), incorporating the Godavari and Mahanadi grabens. Another two seismic sections were used from Singh & Mishra (2002), and Mishra *et al.* (1999). The interpreted profiles (by the authors) are displayed in Figures 4.30 and 4.31, and the extrapolated heat flow and crustal RHP contribution models for each profile are shown in Figure 4.32. These theoretical heat flow contribution models were produced to examine the crustal column heat distribution. They assume an average Moho input of 15 mWm^{-2}, and result in a range of surface heat flow values between 69.1 mWm^{-2} and 97.5mWm^{-2}, which are consistent with heat flow measurements from Kumar *et al* (2007).

The layer thicknesses and composition were predefined by Kumar *et al*. (2007), and in the remaining two seismic sections, they were estimated using line-of-sight and densities. Temperature and pressure dependant conductivity was extrapolated from the formula derived from Hofmeister *et al*. (2007). A constant upper boundary condition of 25^{o}C, and a lower boundary condition of 15 ± 5 mWm^{-2} was set for each model. Table 4.4 displays all necessary input parameters used in each model.

The models were run using 10,000 iterations each, utilising random parameters defined by the range from the standard deviations. Plausible results were

then selected according to a maximum temperature of 1330^{o}C (to stipulate a solid mantle), and a maximum surface heat flow of 150mWm^{-2}.

4.3.2. NEGB – Layering from Kumar *et al*. (2007)

Within the plausible parameters, 94% of the iterations were deemed to fit these conditions. Figure 4.33 displays these models, resulting in an average surface heat flow of 67.2 ± 8.2 mWm^{-2}, a Moho temperature of 649 ± 122.8^{o}C, a Moho heat flow of 14.7 ± 4.4 mWm^{-2}, and a temperature of 907.1 ± 207.1^{o}C at 100km depth. These results strongly agree with the values given by Kumar *et al*. (2007), of a surface heat flow of 69 mWm^{-2}, and a Moho input of 15mWm^{-2}.

4.3.3. SEGB – Layering from Kumar *et al*. (2007)

Within the plausible parameters, 51.7% of the iterations were deemed to fit these conditions. Figure 4.34 displays these models, resulting in an average surface heat flow of 82.5 ± 6.5 mWm^{-2}, a Moho temperature of 857.2 ± 95.6^{o}C, a Moho heat flow of 15.7 ± 3 mWm^{-2}, and a temperature of 1143 ± 137.6^{o}C at 100km depth.

4.3.4. Mahanadi Graben – Layering from Mishra *et al*. (1999)

Within the plausible parameters, 89.17% of the iterations were deemed to fit these conditions. Figure 4.35 displays these models, resulting in an average surface heat flow of 83 ± 7.9 mWm^{-2}, a Moho temperature of 717.9 ± 101.8^{o}C, a Moho heat flow of 17.4 ± 3.5 mWm^{-2}, and a temperature of 1035.2 ± 166^{o}C at 100km depth.

4.3.5. SEGB – Layering from Singh and Mishra (2002)

Within the plausible parameters, 80.72% of the iterations were deemed to fit these conditions. Figure 4.36 displays these models, resulting in an average surface heat flow of 97.3 ± 6.7 mWm^{-2}, a Moho temperature of 781.7 ± 89.6^{o}C, a Moho heat flow of 16.8 ± 3.3 mWm^{-2}, and a temperature of 1092.1 ± 148.5^{o}C at 100km depth.

4.3.6. Palaeo-geotherms at 550 Ma ago.

550Ma was used, as this is when the thrusting of the Eastern Ghats over the Archaean cratons are said to have occurred (Chetty 2001, Kumar *et al*. 2007, Das *et al*. 2008, Mukhopadhyay & Basak 2009, Chetty *et al*. 2010); and the evolution of the UHT orogen can be examined. From Dharma & Chmielkowski (2010) and S. Marshall pers. comm. (2010), the amount of denudation that has occurred since 550 Ma is approximately 30km, due to average pressures of 10kbar seen in surface granulites. This top layer of 30km is added to the pre-existing models (only for the SEGB), and is assigned conservative parameters; such as RHP of 2 ± 1 μWm^{-2}, and a conductivity of $4Wm^{-1}K^{-1}$. New RHP values are also computed (Figure 4.37), as these values would have been slightly elevated in this period due to the radioactive decay rate.

The plausible parameters used to define a UHT orogen in these models were a Moho (between 30 and 40km) temperature between 900 and 1100^{o}C, and the input parameters are displayed in Table 4.5.

When examining the SEGB model (layering defined by Kumar *et al*. (2007)), only 3.57% of the iterations were concordant with the UHT parameters. Surface heat flow was found to have an average of 132.1 ± 22 mWm^{-2}, the average temperature at 40km depth is 1290 ± 117.1^{o}C, the heat flow at 40km is 54.2 ± 8.2 mWm^{-2}, and the average temperature at 100km depth was 1852.7 ± 217.8^{o}C (Figure 4.38). Most other models produced, resulted in much higher temperatures and heat fluxes; with an average temperature of approximately 2000^{o}C at the Moho, and an average surface heat flow of 175 mWm^{-2}. These models are disregarded, as melting of the crust would have occurred at shallow depths (15 – 20km), and the granulites currently seen today would be consumed by the mantle.

Additionally, after examining the SEGB model (layering defined by Singh & Mishra (2002)), only 1.22% of the iterations were concordant with the UHT parameters. Surface heat flow was found to have an average of 138.1 ± 21.6 mWm^{-2}, the average temperature at 40km depth is 1367.9 ± 98.5^{o}C, the heat flow at 40km is 65.9 ± 8.2 mWm^{-2}, and the average temperature at 100km depth was 1890 ± 194^{o}C (Figure 4.39). Similar to the previous model, the majority of iterations resulted in much higher temperatures and heat fluxes; with an average temperature of approximately 2200^{o}C at the Moho, and an average surface heat flow of 180 mWm^{-2}; which again, is implausible.

4.4 Gamma ray spectrometer calibration results

The results of the gamma ray spectrometry calibration are shown in Figures 4.40 – 4.44 and appendix 2. After calibration has been applied to the raw spectra, it is now apparent that the gamma ray spectrometer is detecting RHPE accurately. Even though the GRS is detecting a larger region of the rock than XRF analysis does, the possibility of heterogeneity did not play a major role in the correlations of the two data sets.

The results from appendix 2 have culminated in the conception that there is a strong association with sample size and the recorded radioelemental concentrations. For field-testing of rock samples, it has become apparent that the only method of conducting an accurate study is to sample the in-situ formation, and to ensure that it is on a ‘clean’ surface with minimal weathering. It is also evident that the GRS should be placed as close as possible to the rock face when undertaking an assay, to minimise attenuation of the gamma radiation emitted from the source.

5. Discussion

It was suggested that since the pre-calibrated uranium values were relatively low, there was either a problem with the GRS's software, or that secular disequilibrium was exerting an influence on the detected concentrations. Subsequent to this, a thorough examination of the calibration process of the GRS software, and copious calibration and sensitivity exercises were done. It can now be confirmed that the values obtained are accurate and precise. Serra (1984a) states that the effective rock sample should have a thickness of 25cm, a radius of 1m and a mass exceeding 100kg, and the sensitivity analysis generally confirms this; that RHPE in hand samples can not be detected accurately. The possibility of using the GRS for 'lab-use' was not examined in this study, whereby a sample is crushed, placed in a gamma ray-insulating environment, and the count time set to long periods (> 10,000 seconds). The purpose of this study was to identify the portable GRS's applicability in field assays, and as such, it is a very credible device to use. It is of my opinion that if the rocks are to be crushed and analysed in the lab, then the accurate method of XRF analysis is better suited. With respect to analysing core samples, analytical results may include great uncertainties when using the 'field-method'.

The RHP levels revealed in the major lithological units in the Eastern Ghats are classed as 'high'. However, the uranium concentrations were not anomalously high; in fact they were found to be relatively depleted in some of the granulites. The high RHP can be attributed to the prevalence of thorium-rich minerals, as the average contribution towards the total RHP from thorium is 3.9 times more than uranium. This fact is supported by the average Th/U ratio of 14.3, denoting that the occurrence of thorium is much more abundant in the Eastern Ghats than uranium.

Whilst the sample numbers were relatively low for thermal conductivity measurements, a good spread of data for all major rock units was acquired, and consistent anisotropy readings were found. The very low uncertainties and propagated errors suggest that the methodologies for analysing thermal conductivity were sufficient. However, extrapolating these values to the required pressures and temperatures involved a calculation, thus increasing uncertainties. The ideal scenario would be to undertake thermal conductivity measurements at the specified pressure and temperature at their relevant depth in the crust.

When utilising only p-wave velocities to constrain the crustal structure for use in heat flow modelling, the propagation of all potential uncertainties leads to the possibility of errors in these types of studies. The densities of crustal sections are averaged to aid in the appointment of RHP values to the crust. This poses two problems. (1) Without rigorous studies of the average densities of the representative lithologies, this practice becomes futile. (2) The arbitrary classification of rock units into separate categories should be replaced with a classification by density.

Assumptions made by other studies and integrated into this study may not be entirely accurate; therefore gathering further thorough data sets in heat production, thermal conductivity, geophysical data and surface heat flow will ensure tighter constraints in stochastic heat flow modelling. The assumptions that I integrated, yet questioned in this study were:

- Moho heat flow values of 15mWm^{-2}. Previous studies of the Eastern Ghats and the adjoining Archaean cratons have found a range of Moho values that could be possible.
- The assumption that similar composition granulites extend from the surface down to the mantle.

- The RHP and thermal conductivity values of the eroded crust in the 550Ma modelling were only conservative estimates.

My results show that at the present day the Eastern Ghats have possible Moho temperatures ranging between 649 ± 122.8^{o}C and 857.2 ± 85.6^{o}C, and Moho heat flows of 14.7 ± 4.4mWm^{-2} to 17.4 ± 3.5mWm^{-2}. This implication signifies that currently the Eastern Ghats could possibly still be an UHT region.

Additionally, results at 550Ma suggest that very high geothermal gradients were present, and only a very small (<5%) number of models resulted in what would constitute a solid crust at 40km depth. This low percentage of plausible models is concerning, and other parameters should be analysed for future modelling scenarios. The majority of models ran resulted in Moho depths ranging from 10km to 40km (Figures 5.1 and 5.2). Therefore, even though at 550Ma crustal thickening was said to have occurred, in retrospect, because of the very high crustal temperatures the crust would be in a thermally transient state, and melting would be proficient up to shallow depths before thermal equilibration occurred. This brings about the question as to why the Eastern Ghats were so hot then. These UHT conditions may have been caused by thermal equilibration from crustal thickening, from high RHP, extension coupled with magmatic intrusions, or a combination of all three.

6. Conclusions

The following major results emerge from this study:

(1) The high RHP of the Eastern Ghats can be attributed to the pervasiveness of thorium-rich minerals, as the average contribution towards the total RHP from thorium is 3.9 times more than uranium, and the average Th/U ratio is 14.3. There was found to be no pattern of surface RHP distribution.

(2) A significant anisotropy of thermal conductivity was found in the rocks from the Eastern Ghats, however superior testing methods need to be applied to take into account pressure and temperature.

(3) The present day thermal structure of the Eastern Ghats could possibly adhere to UHT conditions. High Moho temperatures (between 649 ± 122.8^{o}C and 857.2 ± 85.6^{o}C), high Moho heat flows (between 14.7 ± 4.4mWm^{-2} and 17.4 ± 3.5mWm^{-2}) and high surface heat flows (between 67.2 ± 8.2mWm^{-2} and 97.3 ± 6.7mWm^{-2}) depict a 'hot' crust in steady state.

(4) The Pan-African reconstruction (550Ma) of Gondwana caused the thrusting of the Eastern Ghats over the Archaean cratons, resulting in very high geothermal gradients, shallow Moho depths and very high surface heat flow (between 138.1 ± 21.6 mWm^{-2} and 132.1 ± 22 mWm^{-2}).

(5) Conclusions drawn from the gamma ray spectrometry results state that the portable GRS should only be used on in-situ formations when undertaking 'field assays', and that the data acquired from the Eastern Ghats was found to be precise and accurate post-calibration.

7. Acknowledgements

I would like to express my gratitude to my primary supervisor Dr. Graham Baines for his guidance, enthusiasm in my project and willingness to help out at all times. I have greatly benefited from his fervour in the field of geothermal energy (and MATLAB), which has also ignited my passion in this field.

My appreciation also goes to my secondary supervisor Associate Professor Alan Collins for the opportunity to participate in this project, and for the possibility of the continuation in studying this field. Thanks also to Professor Martin Hand and Dr. Guillaume Backe for their company and advice in India, and here in Adelaide.

I would like to thank my Indian travelling companions and good friends Campbell Harvey, Billy Reid and Sarah Marshall, for an unforgettable trip. To all my other Honors mates (especially Will Teale) I would like to say thank you for providing me with a humorous and supportive environment, not only in Adelaide, but also on our field trips.

Thank you to Dr. Sukanta Roy and his team from NGRI, India, for conducting thermal conductivity tests on my rocks, providing me with many valuable papers/books to read, and also the fruitful correspondance about my project. I look forward to maybe working with you one day.

Thanks to Dr. Saibal Gupta and Ananda Modak for their company and friendship in India.

A shout out to Ravi and Muduli; our Indian driver's and personal bodyguards.

To my Mum and Dad and two brothers (Nick, Janine, Dan and Mike) thanks for being you! I wouldn't be here without your love, support and encouragement.

8. References

Abbady A.G.E., El-Arabi A.M. and Abbady A., 2006. Heat production rate from radioactive elements in igneous and metamorphic rocks in Eastern Desert, Egypt. Applied radiation and isotopes, Vol. 64, pp 131-137.

Abdulagatov I.M., Emirov S.N., Abdulagatova Z.Z. and Askerov S.Y., 2006. Effect of pressure and temperature of the thermal conductivity of rocks. Journal of chemical engineering, Vol. 51, pp 22-33.

Abdulagatova Z., Abdulagatov I.M. and Emirov V.N., 2009. Effect of temperature and pressure on the thermal conductivity of sandstone. International journal of rock mechanics and mining sciences, Vol. 46, pp 1055-1071.

Bhattacharya S., 1996. Eastern Ghats granulite terrain of India: an overview. Journal of Southeast Asian Earth Sciences. Vol 14, pp 165-174.

Bhattacharya S., 1997. Evolution of Eastern Ghats granulite belt of India in a compressional tectonic regime and juxtaposition against Iron Ore Craton of Singhbhum by oblique collision-transpression. Proceedings of the Indian Academy of Sciences Earth and Planetary Sciences. Vol 106, pp 65-75.

Chetty T.R.K., 2001. The Eastern Ghats Mobile Belt: A collage of juxtaposed terranes. Gondwana Research, Vol. 4, pp 319-328.

Chetty T.R.K., 2010. Structural architecture of the northern composite terrane, the Eastern Ghats Mobile Belt, India; Implications fro Gondwana tectonics. Gondwana Research, doi: 10.1016.

Clauser C. 2006. Geothermal Energy, In: K. Heinloth (ed), Landolt-Bornstein, Group VIII: Advanced materials and technologies, Vol. 3: Energy technologies, Subvol. C:Renewable energies, Springer Verlag, pp 493-604.

Clauser C. and Huenges E., 1995. Thermal conductivity of rocks and minerals, in: Rock physics and phase relations, chapter 10, AGU.

Correia A. and Jones F.W., 1996. On the importance of measuring thermal conductivities for heat flow density estimates: an example from the Jeanne d'Arc Basin, offshore eastern Canada. Tectonophysics, Vol. 257, pp 71-80.

Das S., Nasipuri P., Bhattacharya A. and Swaninathan S., 2008. The thrust-contact between the Eastern Ghats Belt and the adjoining Bastar Craton (Eastern India): Evidence from mafic granulites and tentonic implications. Precambrian research, Vol. 162, pp 70-85.

Dasgupta S., Sengupta P., Fukuoka M. and Bhattacharya P.K., 2010. Mafic Granulites from the Eastern Ghats, India: Further evidence for extremely high temperature crustal metamorphism. The Journal of Geology, Vol. 99, pp 124-133.

Dharma Rao C.V. and Chmielowski R.M., 2010. New constraints on the metamorphic evolution of the Eastern Ghats Belt, India, based on relict composite inclusions in garnet from ultrahigh-temperature sapphirine granulites. Geological Journal (online), Wiley Interscience.

Foden J.D., Elburg M.A., Turner S.P., Sandiford M., O'Callaghan J. & Mitchell S., 2002. Granite Production in the Delamerian Orogen, South Australia. Journal of the Geological Society, London, Vol 159, pp 557-575.

Grasty R. and Minty B., 1995. A guide to the technical specifications for airborne gamma-ray surveys. Australian Geological Survey Organisation. Record 1995/60.

Groves P. and Campbell I., 1995. Airborne radiometric calibration – as Australian perspective. Exploration Geophysics, Vol. 26, pp 284-291.

Gupta M.L., 1982. Heat flow in the Indian Peninsula – Its geological and geophysical implications. Tectonophysics, Vol. 83, pp 71-90.

Gupta H. and Roy S., 2007. Geothermal Energy, An alternative resource for the 21st century. Elsevier.

Hofmeister A.M., Branlund J.M., and Pertermann M., 2007. Properties of rocks and minerals – Thermal conductivity of the Earth, in Treatise on Geophysics, Chapter 2 Mineral Physics. Elsevier.

Hofmeister A.M. and Criss R.E., 2005. Earth's heat flux revised and linked to chemistry. Tectonophysics, Vol. 395, pp 159-177.

Horai K.I., 1971. Thermal conductivity of rock-forming minerals. Journal of geophysical research, Vol. 79, pp 1278-1308.

Jaupart C. and Mareschal J. C., 2007. Heat flow and thermal structure of the lithosphere, in Treatise on Geophysics, Chapter 6 Crust and lithosphere dynamics. Elsevier.

Johnson L.R. and Wenk H.R., 1974. Anisotropy of physical properties in metamorphic rocks. Tectonophysics, Vol. 23, pp 79-98.

International Atomic Energy Agency (IAEA), 2003. Guidelines for radioelement mapping using gamma ray spectrometry data. IAEA, Austria.

Ketcham R., 1996a. An improved method for determination of heat production with gamma-ray scintillation spectrometry. Chemical Geology, Vol 130, pp175-194.

Ketcham R., 1996b. Distribution of heat-producing elements in the upper and middle crust of southern and west central Arizone: Evidence from the core complexes. Journal of Geophysical Research, Vol. 101, pp 611-632.

Kumar P.S., Menon R. and Reddy G.K., 2007. The role of radiogenic heat production in the thermal evolution of a Proterozoic granulite-facies orogenic belt: Eastern Ghats, Indian Shield. Earth and Planetary science letters. Vol. 254, pp 39-54.

Kumar P.S., Menon R. and Reddy G.K., 2009. Heat production heterogeneity of the Indian crust beneath the Himalaya: Insights from the northern Indian Shield. Earth and planetary science letters, Vol. 283, pp 190-196.

Kumar P.S. and Reddy G.K., 2004. Radioelements and heat production of an exposed Archaean crustal cross-section, Dharwar craton, south India. Earth and Planetary science letters. Vol. 224, pp 309-324.

Løvborg L. and Mose E., 1987. Counting statistics in radioelement assaying with a portable spectrometer. Geophysics, Vol. 52, pp 555-563.

McKenzie D., Jackson J. and Priestley K., 2005. Thermal structure of oceanic and continental lithosphere. Earth and Planetary Science letters, 233, pp337-349.

Manglik A., 2006. Mantle heat flow and thermal structure of the northern block of Southern Granulite Terrain, India. Journal of geodynamics, Vol. 41, pp 510-519.

Marshall S., 2010. An integrated metamorphic, geochronological and spatial approach to the classic Eastern Ghats large hot orogen, India. Thesis, unpublished.

Matthews C., 2009. Geothermal energy prospectivity of the Torrens Hinge Zone: evidence from new heat flow data. Exploration geophysics, Vol. 40, pp 288-300.

Matthews C., and Beardsmore G., 2007. New heat flow data from south-eastern South Australia. Exploration geophysics, Vol. 38, pp 260-269.

Mildren S.D. and Sandiford M., 1995. Heat refraction and low pressure metamorphism in the northern Flinders Ranges, South Australia. Australian journal of Earth Sciences. Vol. 42, pp 241-247.

Minty B., Franklin R., Milligan P., Richardson M. and Wilford J., 2009. The Radiometric map of Australia. Exploration Geophysics, Vol. 40, pp325-333.

Minty B.R.S., Luyendyk A.P.J. and Brodie R.C., 1997. Calibration and data processing for airborne gamma-ray spectrometry. Journal of Australian geology and geophysics, Vol 17, pp 51-62.

Mishra D.C., Chandra Sekhar D.V., Venkata Raju D.Ch. and Kumar V.V., 1999. Crustal structure based on gravity–magnetic modelling constrained from seismic studies under Lambert Rift, Antarctica and Godavari and Mahanadi rifts, India and their interrelationship. Earth and Planetary Science Letters, Vol. 172, pp 287-300.

Mukhopadhyay D. and Basak K., 2009. The Eastern Ghats Belt… A polycyclic granulite terrain. Journal of Geological Society of India, Vol. 73, pp 489-518.

Palmer J., 2009. The Eastern Ghats Mobile Belt, India: Anisotropy of Magnetic Susceptibility (AMS), a comparison with structural field, geochronological and heat production data. Unpublished thesis.

Radiation Solutions INC, 2008. RS-125 Super-Spec RS-230 Super-Spec Users manual.

Rai S.N. and Thiagarajan S., 2006. A tentative 2D thermal model of central India across the Narmada-Son Lineament (NSL). Journal of Asian Earth sciences, Vol. 28, pp 363-371.

Rao R.U.M., Verma R.K., Venkateshwar Rao G., Hamza V.M., Panda P.K. and Gupta M.L., 1970. Heat flow studies in the Godavari Valley (India). Tectonophysics, Vol. 10, pp 165-181.

Rao G.V. and Rao R.U.M., 1980. A geothermal study of the Jharia Gongwana Basin (India): Heat flow results from several holes and heat production of basement rocks. Earth and Planetary science letters, Vol. 48, pp 397-405.

Rao G.V. and Rao R.U.M., 1983. Heat flow in Indian Gondwana basins and heat production of their basement rocks. Tectonophysics, Vol. 91, pp 105-117.

Ray L., Bhattacharya A., Roy S., 2007. Thermal conductivity of Higher Himalayan Crystallines from Garwhal Himalaya, India. Tectonophysics, Vol. 434, pp 71-79.

Ray L., Förster H.J., Schilling F.R., Förster A., 2006. Thermal diffusivity of felsic to mafic granulites at elevated temperatures. Earth and Planetary Science letters, Vol. 251, pp 241-253.

Ray L., Kumar S.P., Reddy G.K., Roy S., Rao G.V., Srinivasan R. and Rao R.U.M., 2003. High mantle heat flow in a Precambrian granulite province: Evidence from Southern India. Journal of geophysical research, Vol. 108.

Ray L., Roy S. and Srinivasan R., 2008. High radiogenic heat production in the Kerala Khondalite Block, Southern Granulite Province, India. International journal of earth sciences. Vol. 97, pp 257-267.

Roy S. and Rao R. U. M., 2000. Heat flow in the Indian shield. Journal of geophysical research, Vol. 105, pp 587-604.

Roy S. and Rao R.U.M., 2003. Towards a crustal thermal model for the Archaean Dharwar craton, southern India. Physic and chemistry of the earth, Vol. 28, pp 361-373.

Roy S., Ray L., Bhattacharya A. and Srinivasan R., 2008. Heat flow and crustal thermal structure in the Late Archaean Closepet Granite batholith, south India. International journal of earth sciences. Vol. 97, pp 245-256.

Serra O., 1984a. Chapter 6 – Measurement of the natural gamma radioactivity, in: Developments in petroleum science 15A, Amsterdam, Elsevier

Serra O., 1984b. Chapter 7 – Natural gamma-ray spectrometry, in: Developments in petroleum science 15A, Amsterdam, Elsevier

Stüwe K., 2007. Geodynamics of the Lithosphere, Quantitative description of geological problems. Springer-Verlag, Berlin, Chapter 3 – Energetics: Heat and temperature.

Singh A.P. and Mishra D.C., 2002. Tectonosedimentary evolution of Cuddapah basin and Eastern Ghats mobile belt (India) as Proterozoic collision: gravity, seismic and geodynamic constraints. Jounal of Geodynamics, Vol. 33, pp 249-267.

The University of Adelaide, 2010. South Australian Centre for Geothermal Energy Research. http://www.adelaide.edu.au/geothermal.

Vilá M., Fernández M., Jimenez-Munt I., 2010. Radiogenic heat production variability of some common lithological groups and its significance to lithospheric thermal modelling. Tectonophysics, Vol. 490, pp 152-164.

Vasseur G., Brigaud F. and Demongodin L., 1995. Thermal conductivity estimation in sedimentary basins. Tectonophysics, Vol. 244, pp167-174.

Whittington A. G., Hofmeister A. M. and Nabelek P. I., 2009. Temperature-dependant thermal diffusivity of the Earth's crust and implications for magmatism. Nature Letters, Vol 458, pp 319-321.

Wong T.F. and Brace W.F., 1979. Thermal expansion of rocks: some measurements at high pressure. Tectonophysics, Vol. 57, pp 95-117.

9. Figure & Table Captions

Figure 1.1 – The distribution of heat producing elements in the Earth's crust and mantle with fixed basal and surface boundary conditions. The distribution (a) (blue line), is a fixed concentration of heat production in the entire crust with a discontinuity at the mantle, resulting in a high geothermal gradient that tapers off at the Moho. The distribution (b) (shaded area) is an exponentially decreasing proportion of heat producing elements; considered to be indicative of most crustal regions. Distributions (c) and (d) are demonstrating a (granitic) intrusion, and heat production concentrated in the upper crust respectively. Modified from Stüwe (2007).

Figure 1.2 – Schematic structure of the thermal boundary layer between the asthenosphere and the lithosphere. In the effectively rigid upper part (h1) of the boundary heat is transported by conduction, and in the unstable lower part of the boundary (h3) heat is brought up by advection. An intermediate depth, h2, is obtained by downward extrapolation of the conductive geotherm to the isentropic temperature profile of the convecting mantle. Reproduced from Jaupart & Mareschal (2007).

Figure 2.1 – Geological map of the Eastern Ghats Belt, including the current study area. Rock types are: a – gneisses, b – charnockites, c – khondalites, d – anorthosites, e – Gondwana sedimentary rocks, and f – alluvium. I, II and III are the locations of DSS studies undertaken by Kumar et al. 2007, Singh and Mishra, 2002 and Mishra et al. 1999 respectively, which are integrated into this study with heat flow modelling. The entire western margin is a thrust belt. The Vamsadara shear zone (VSZ) divides the Northern Eastern Ghats Belt (NEGB) and the Southern Eastern Ghats Belt (SEGB). The belt is dissected by the Godavari (GG) and Mahanadi (MG) grabens.

Only three surface heat flow measurements exist (in mWm^{-2}) east of the GG, and heat production assay localities (undertaken by Kumar et al. 2007) are listed. Modified from Kumar et al. (2007).

Figure 2.2 – Gridded heat flow map of India – Dhar = Dharwar craton, B & K = Badami and Kaladgi Basins, G = Godavari Basin, Cud = Cuddapah Basin, Ch = Chattsgarh Basin. It is evident that there are high geothermal gradients in the Eastern Ghats.

Figure 2.3 – Transect of paths to be taken, from Vizag – Vizianagaram – Araku, and Vizag – Vaddadi – Paderu – Araku.

Table 3.1 - Energy regions and associated isotopes used when determining what radioelement is being counted by a GRS. Reproduced from IAEA (2003).

Figure 3.1 – Graph depicting initial uranium values in comparison to a study done by Kumar et al. (2007) according to their rock classification scheme. It is evident from this, that uranium concentrations are much lower in three out of four lithological units.

Figure 3.2 – Graph of initial GRS assays from the Eastern Ghats. Y-axis is the ratio of the cpm uranium to thorium, and anything under a ratio of approximately 0.3, results in zero ppm uranium. This graph should show a 1:1 correlation with no zero uranium readings.

Figure 3.3 – Graph showing uranium cpm against uranium ppm, with many zero uranium concentrations even though there are counts being detected. This should be a 1:1 correlation.

Figure 3.4 – Graph depicting concentrations calculated for uranium against thorium, and it is evident that there were very few zero thorium readings compared to the many zeros of uranium.

Figure 3.5 – Assays 189 & 190 from the Eastern Ghats plotted together, to demonstrate the minor differences in spectral signature.

Figure 3.6 – Comparison of GRS data with XRF chemistry from the Eastern Ghats, (Marshall 2010) and Kangaroo Island (Foden et al. 2002) for uranium concentrations. This graph demonstrates that the GRS data have a good correlation with the XRF analysis. All data is close to the Y = X line, with the calibrated data being the closer fit.

Figure 3.7 – Comparison of GRS data with XRF chemistry from the Eastern Ghats, (Marshall 2010) and Kangaroo Island (Foden et al. 2002) for thorium concentrations. This graph demonstrates that the GRS data have a good correlation with the XRF analysis. All data is exceptionally close to the Y = X line, with the calibrated data being the closer fit.

Figure 3.8 – Comparison of GRS data with XRF chemistry from the Eastern Ghats, (Marshall 2010) and Kangaroo Island (Foden et al. 2002) for potassium

concentrations. This graph demonstrates that the GRS data have a good correlation with the XRF analysis. All data is close to the Y = X line, with the calibrated data being the closer fit.

Figure 3.9 – Comparison of GRS data with XRF chemistry from the Granite Island granites (Foden et al. 2002) for all three radioelement concentrations. This graph demonstrates that the GRS data all have superbly close values to those found in the literature study.

Figure 3.10 – This is Figure 3.33 after calibrations have been done, demonstrating that there is now a 1:1 correlation of data pertaining to the comparison of counts and concentration results.

Figure 3.11 – The range of conductivities (in $Wm^{-1}K^{-1}$) of a sandstone sample with differing pressure and temperature ranges (from Abdulagatova et al. 2009). An inflection point at 23MPa and 100MPa demonstrates that the rate of thermal conductivity change decreases at this pressure.

Table 4.1 - Summary of heat production values for the lithologies of the Eastern Ghats. This table displays the pre and post calibration values of heat production, as well as the data from Palmer (2009). The values in brackets are the number of samples used in Palmer (2009)'s study.

Table 4.2 – Estimated thermal conductivity values. Blue values are mineral conductivities from two separate authors (Clauser and Huenges 1995, and Horai 1971). Mineralogy percentages of each lithology are shown, with calculated arithmetic, harmonic and geometric mean for parallel and perpendicular to foliation. The green shading denotes what mixing model is preferably used for each orientation, and the yellow shaded area are the NGRI conductivities for a comparison.

Table 4.3 – Results from thermal conductivity testing on Eastern Ghats samples (undertaken at the University of Adelaide and NGRI, Hyderabad), with anisotropy shown (parallel/perpendicular).

Table 4.4 – Input parameters used in each separate model at 0Ma.

Table 4.5 – Input parameters used in both models at 550Ma.

Figure 4.1 – Heat production comparison from the Eastern Ghats to Kumar et al. (2007) after calibration is completed, and a more thorough rock classification done.

Figure 4.2 – Uranium data from the Eastern Ghats. These values have a much closer correlation to Kumar et al. (2007).

Figure 4.3 – Thorium data from the Eastern Ghats, compared to Kumar et al. (2007).

Figure 4.4 – Heat production results of all lithologies from the Eastern Ghats. Quartzo-feldspathic gneiss resulted in highest heat production of 5.49 ±0.69 μWm^{-3},

Khondalites with second highest heat production of 3.76 ±0.53 μWm^{-3}, and the UHT granulites with a low heat production of 0.69 ±0.23 μWm^{-3}.

Figure 4.5 – Probability density graph for Khondalites, showing a mean of 3.76 μWm^{-3}, and some outliers up around the 9-12 μWm^{-3}.

Figure 4.6 - Probability density graph for Charnockites, showing a mean of 1.52 μWm^{-3}.

Figure 4.7 - Probability density graph for Quartzo-feldspathic gneiss, showing a mean of 5.49 μWm^{-3}, with outliers at very high values of 10-15 μWm^{-3}.

Figure 4.8 - Probability density graph for K-feldspar megacrystic granite, showing a mean of 2.79 μWm^{-3}, with three outliers at very high values. These values were from a migmatised shear zone along the Hukumpeta River Crossing, just outside of Paderu.

Figure 4.9 - Probability density graph for Quartzite, showing a mean of 2.42 μWm^{-3}.

Figure 4.10 - Probability density graph for the UHT granulite, showing a mean of 0.69 μWm^{-3}.

Figure 4.11 - Probability density graph for Gt/Sill/Crd gneiss, showing a mean of 2.72 μWm^{-3}, with a large spread of data.

Figure 4.12 - Probability density graph for Gt/Sill gneiss, showing a mean of 2.70 μWm^{-3}.

Figure 4.13 - Probability density graph for felsic gneiss, showing a mean of 2.80 μWm^{-3}.

Figure 4.14 – Probability density graph (with histogram) of the total of all heat production values for the Eastern Ghats. The bimodal distribution is most likely due to the dominant khondalites and charnockites.

Figure 4.15 – Surface heat production distribution of study area in the Eastern Ghats. The colour of the marker represents lithology. Blue = Khondalite, Red = Charnockite, Magenta = K-feldspar megacrystic granite, White = Quartzite, Brown = Quartzo-feldspathic gneiss, Green = Gt/Sill gneiss and Orange = UHT granulite. The size of the marker depicts the heat production value. I.e., the smallest size is below 1 μWm^{-3}, and the largest marker is above 6 μWm^{-3}.

Figure 4.20 – Conductivity plot for all samples from the Eastern Ghats. All values are in $Wm^{-1}K^{-1}$. The shaded white area is the where the estimated harmonic value lies. The shaded yellow bars are the estimated geometric value and the shaded green bars are where the arithmetic mean values lie. Blue squares are the average measured conductivity perpendicular to foliation, and the red diamond is the average measured conductivity parallel to foliation (with error bars). The black circle depicts the isotropic value for charnockite. All measured values are relatively low compared to the estimated thermal conductivity.

Figure 4.30 – Seismic profile from Singh and Mishra (2002). The most eastern part of the profile was used for 1D thermal modelling (over Kavali).

Figure 4.31 – Seismic profile from Mishra et al. (1999). The centre of the profile was used for 1D thermal modelling.

Figure 4.32 – Present-day crustal contribution to surface heat flow (all values are in mWm^{-2}), using an average constant mantle input of $15mWm^{-2}$. The value at the bottom of the box is the lower boundary condition (mantle input). The boxes represent approximate layer geometries and corresponding heat production. The value above the box is the total crustal contribution, and the value at the top in the smaller box is the theoretical combined heat flow from the crust and mantle. Profile (a) is the NEGB from Kumar et al. (2007). Profile (b) is the SEGB from Kumar et al. (2007). Profile (c) is from Singh and Mishra (2002). Profile (d) is from Mishra et al. (1999).

Figure 4.33 – Present day plausible stochastic heat flow modelling results for the NEGB using Kumar et al. (2007)'s layering.

Figure 4.34 – Present day plausible stochastic heat flow modelling results for the SEGB using Kumar et al. (2007)'s layering.

Figure 4.35 – Present day plausible stochastic heat flow modelling results for the Mahanadi Graben using Mishra et al. (1999)'s layering.

Figure 4.36 – Present day plausible stochastic heat flow modelling results for the SEGB using Singh and Mishra (2002)'s layering.

Figure 4.37 – Probability density graph (with histogram) of the total of all heat production values for the Eastern Ghats at 550Ma.

Figure 4.38 – Past (550Ma) plausible stochastic heat flow modelling results, defined by UHT conditions for the SEGB using Kumar et al. (2007)'s layering.

Figure 4.39 – Past (550Ma) plausible stochastic heat flow modelling results, defined by UHT conditions for the SEGB using Singh and Mishra (2002)'s layering.

Figure 5.1 – All past (550Ma) stochastic heat flow modelling results for the SEGB, using Singh and Mishra (2002)'s layering. Note that at 20km depth average temperatures exceed the melting point of the mantle.

Figure 5.2 – All past (550Ma) stochastic heat flow modelling results for the SEGB, using Kumar et al (2007)'s layering. Note the high surface heat flux (>150mWm^{-2}) and very high geothermal gradients.

10. Tables

Table 3.1

Window	Nuclide	Energy Range (MeV)
Total Count	–	0.400 – 2.810
Potassium	^{40}K (1.460 MeV)	1.370 – 1.570
Uranium	^{214}Bi (1.765 MeV)	1.660 – 1.860
Thorium	^{208}Tl (2.614 MeV)	2.410 – 2.810

Table 4.1

		Calibrated		Pre-calibrated		Palmer, 2009
Rock type	**Number**	**Heat Production (μWm^{-3})**	**±1σ**	**Heat Production (μWm^{-3})**	**±1σ**	**Heat Production (μWm^{-3})**
Khondalite	48	**3.76**	0.53	3.41	0.51	3.51 (25)
Charnockite	27	**1.52**	0.29	1.32	0.26	1.95 (48)
K-spar Megacrystic granite	28	**2.79**	0.53	2.44	0.51	3.44 (8)
Gt/Sill granitic gneiss	3	**2.70**	0.43	2.39	0.39	
Gt/Sill/Crd gneiss	7	**2.72**	0.41	2.38	0.40	
Quartzo-feldspathic gneiss	40	**5.49**	0.69	5.11	0.67	1.46 (5)
Felsic gneiss	14	**2.80**	0.44	2.45	0.42	
Quartzite	5	**2.42**	0.42	2.12	0.40	
UHT Granulite	5	**0.69**	0.23	0.63	0.21	

Table 4.2

Clauser, 1995 - Thermal conductivity of rocks and minerals

Conductivity ($Wm^{-1}K^{-1}$)	10.17	6.15	3.14	0.52	3.89	0.62	2.34	?	2.34	?	3.6	155	5.15	2.81	12.14	17.7	9.1	4.66	4.47		Estimated Conductivity - Parallel to Foliation			Estimated Conductivity - Perpendicular to Foliation		
	Qtz (parallel)	Qtz (perp.)	Bt (parallel)	Bt (perp.)	Musc (parallel)	Musc. (perp.)	K-feldspar	Cordierite	Plagioclase	Sphene	Garnet	Graphite	Chlorite	Amphibole	Spinel	Corundum	Sillimanite	CPX	OPX	TOTAL %	Arithmetic mean	Harmonic mean	Geometric mean	Arithmetic mean	Harmonic mean	Geometric mean
Khondalite	0.3	0.3	0.1	0.1	0.05	0.05	0.25	0	0	0	0.1	0.01	0	0.04	0	0	0.1	0	0.05	1.00	**7.30**	4.08	**4.98**	5.67	**2.03**	**3.27**
Charnockite	0.2	0.2	0.05	0.05	0	0	0.3	0	0.25	0	0.05	0	0	0.05	0	0	0	0.05	0.05	1.00	**4.26**	3.08	**3.51**	3.32	**2.40**	**2.90**
Quartzo-feldspathic gneiss	0.45	0.45	0.2	0.2	0.1	0.1	0.2	0	0	0	0.05	0	0	0	0	0	0	0	0	1.00	**6.24**	4.29	**5.17**	3.58	**1.39**	**2.39**
K-Spar Megacrystic granite	0.39	0.39	0.1	0.1	0	0	0.3	0	0.1	0	0.1	0.01	0	0	0	0	0	0	0	1.00	**7.13**	3.72	**4.65**	5.30	**2.20**	**3.20**
UHT Granulite	0.05	0.05	0.05	0.05	0	0	0.05	0.05	0.25	0.05	0.1	0	0	0.1	0.02	0	0	0.18	0.1	1.00	**3.54**	3.64	**3.12**	3.21	**2.79**	**2.78**
Quartzite	0.8	0.8	0.05	0.05	0.05	0.05	0.1	0	0	0	0	0	0	0	0	0	0	0	0	1.00	**8.72**	6.66	**7.89**	5.21	**2.86**	**4.40**
Gt/Sill/Crd gneiss	0.3	0.3	0.1	0.1	0	0	0.1	0.05	0.04	0	0.15	0.01	0	0	0	0	0.2	0	0.05	1.00	**7.83**	5.10	**5.41**	6.36	**2.66**	**3.89**
Mg/Al Rich metapelite	0.2	0.2	0.05	0.05	0	0	0.4	0	0.1	0	0.05	0	0	0	0.1	0.1	0	0	0	1.00	**6.53**	3.61	**4.70**	5.59	**2.70**	**3.88**

Horai K, 1971 - Thermal conductivity of rock-forming minerals

In mcal cm^{-1} sec^{-1} $°C^{-1}$	18.37	4.83	5.96	5.95	5.53	7.91	?	6.5	11.74	5.58	7.35	22.65	?	21.73	11.79	10.5					
Conductivity ($Wm^{-1}K^{-1}$)	7.69	2.02	2.50	2.49	2.32	3.31	?	2.72	4.92	2.34	3.08	9.48	?	9.10	4.94	4.40		Estimated Conductivity			
	Quartz	Biotite	Muscovite	K-feldspar	Plagioclase	Garnet	Graphite	Cordierite	Chlorite	Sphene	Amphibole	Spinel	Corundum	Sillimanite	CPX	OPX	TOTAL %	Arithmetic mean	Harmonic mean	Geometric mean	NGRI K's
Khondalite	0.3	0.1	0.05	0.25	0	0.1	0.01	0	0	0	0.04	0	0	0.1	0	0.05	1.00	4.84	3.64	4.12	
Charnockite	0.2	0.2	0	0.3	0.1	0.05	0	0	0	0	0.05	0	0	0	0.05	0.05	1.00	3.71	2.93	3.24	3.43 - 2.82
Quartzo-feldspathic gneiss	0.45	0.2	0.1	0.2	0	0.05	0	0	0	0	0	0	0	0	0	0	1.00	4.78	3.41	4.03	
K-Spar Megacrystic granite	0.39	0.1	0	0.3	0.1	0.1	0.01	0	0	0	0	0	0	0	0	0	1.00	4.51	3.40	3.83	3.41
UHT granulite	0.05	0.05	0	0.05	0.25	0.1	0	0.05	0	0.05	0.1	0.02	0	0	0.18	0.1	1.00	3.60	3.10	3.31	1.90
Quartzite	0.8	0.05	0.05	0.1	0	0	0	0	0	0	0	0	0	0	0	0	1.00	6.63	5.29	6.08	2.12
Gt/Sill/Crd gneiss	0.3	0.1	0	0.1	0.04	0.15	0.01	0.05	0	0	0	0	0	0.2	0	0.05	1.00	5.52	4.12	4.72	2.65 - 2.54
Mg/Al Rich metapelite	0.2	0.05	0	0.4	0.1	0.05	0	0	0	0	0	0.1	0.1	0	0	0	1.00	3.98	3.57	3.24	2.9 - 2.39

Table 4.3

Unit	Measured Perp. to foliation (W/m/K)	Error	Measured Parr. to foliation (W/m/K)	Error	Measured Isotropic (W/m/K)	Error	Measured Anisotropy
Khondalite	2.49	0.06	2.92	0.21			**1.18**
Charnockite					2.40	0.20	
Quartzofeldspathic gneiss	2.66	0.14	4.09	0.30			**1.54**
K-spar megacrystic Granite	1.96	0.09	2.43	0.33			**1.24**
UHT Granulite	2.09	0.15	2.71	0.06			**1.30**
Gt/Sill/Crd Gneiss	2.49	0.17	3.04	0.13			**1.22**
Mg/Al rich metapelite	2.06	0.18	2.95	0.26			**1.43**

Table 4.4

Kumar *et al.* (2007) SEGB									
Layers	**Depth to Base**		**K**		**HP**		**Density**	**Specific heat capacity**	
	km	**±**		**±**		**±**			
Upper Crust	5	1	3.5	0.26	3.7	0.44	2.67	800	
Middle Crust 1	15	2	2.37	0.31	1.67	0.35	2.67	800	
Middle Crust 2	25	3	2.22	0.19	2.58	0.38	2.9	800	
Lower Crust	40	4	2.4	0.15	0.69	0.23	2.9	800	
Mantle	100	0	4.7	0.25	0.05	0.01	3.3	800	
Kumar *et al.* (2007) NEGB									
Layers	**Depth to Base**		**K**		**HP**		**Density**	**Specific heat capacity**	
	km	**±**		**±**		**±**			
Upper Crust	6	1	2.79	0.19	2.99	0.48	2.67	800	
Middle Crust 1	20	2	2.35	0.21	1.84	0.41	2.67	800	
Lower Crust	35	3	2.4	0.15	0.69	0.23	2.9	800	
Mantle	100	0	4.7	0.25	0.05	0.01	3.3	800	
Mishra *et al*. (1999)									
Layers	**Depth to Base**		**K**		**HP**		**Density**	**Specific heat capacity**	
	km	**±**		**±**		**±**			
Upper Crust	1	0.5	3.07	0.25	3.43	0.49	2.35	800	
Middle Crust 1	12	1	2.71	0.25	3.76	0.53	2.7	800	
Middle Crust 2	21	2	2.4	0.25	1.52	0.29	2.67	800	
Lower Crust	34	3	2.4	0.25	0.69	0.25	3.3	800	
Mantle	100	0	4.7	0.25	0.05	0.01	3.3	800	
Singh and Mishra *et al*. (2002)									
Layers	**Depth to Base**		**K**		**HP**		**Density**	**Specific heat capacity**	
	km	**±**		**±**		**±**			
Upper Crust	10	1	3.07	0.26	3.43	0.44	2.71	800	
Middle Crust 1	19	2	2.71	0.31	3.76	0.35	2.76	800	
Middle Crust 2	23	2	2.4	0.19	1.52	0.38	2.88	800	
Lower Crust	35	3	2.7	0.15	0.69	0.23	2.9	800	
Mantle	100	0	4.7	0.25	0.05	0.01	3.3	800	

Table 4.5

Kumar *et al*. (2007) - SEGB @ 550Ma									
Layers	**Depth to Base**		**K**		**HP**		**Density**	**Specific heat capacity**	
	km	**±**		**±**		**±**			
Eroded layer	0-30		4	1	2	1	2.67	800	
Upper Crust	35	1	3.5	0.26	3.89	0.5	2.67	800	
Middle Crust 1	45	2	2.37	0.31	1.79	0.39	2.67	800	
Middle Crust 2	55	3	2.22	0.19	2.73	0.43	2.9	800	
Lower Crust	70	4	2.4	0.15	0.73	0.25	2.9	800	
Mantle	100	0	4.7	0.25	0.05	0.01	3.3	800	
Singh and Mishra (2002) - SEGB @ 550Ma									
Layers	**Depth to Base**		**K**		**HP**		**Density**	**Specific heat capacity**	
	km	**±**		**±**		**±**			
Eroded stuff	0-30	0	4.5	1	1.5	1	2.67	800	
Upper Crust	40	1	3.07	0.26	3.59	0.56	2.71	800	
Middle Crust 1	49	2	2.71	0.31	3.93	0.61	2.76	800	
Middle Crust 2	63	2	2.4	0.19	1.64	0.33	2.88	800	
Lower Crust	65	3	2.4	0.15	0.73	0.31	2.9	800	
Mantle	100	0	4.7	0.25	0.05	0.01	3.3	800	

11. Figures

Figure 1.1

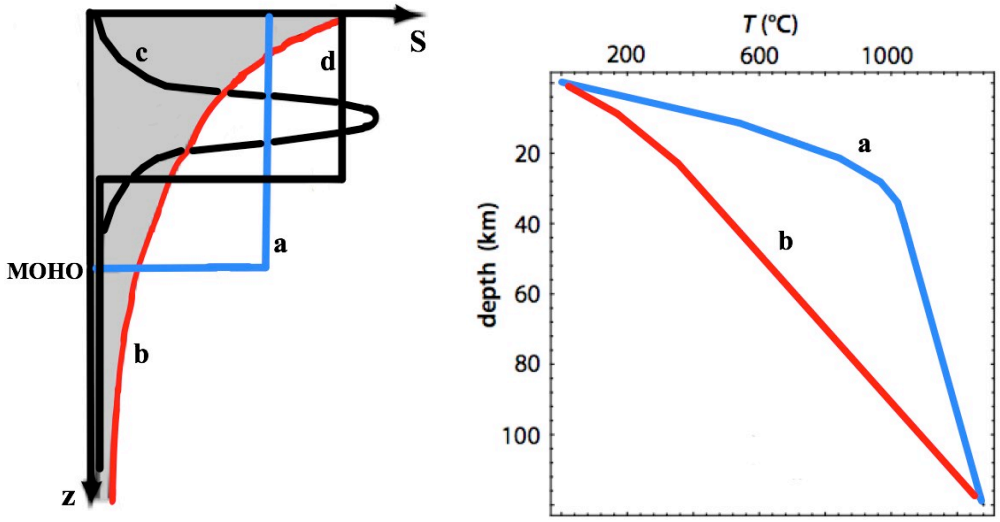

Figure 1.2

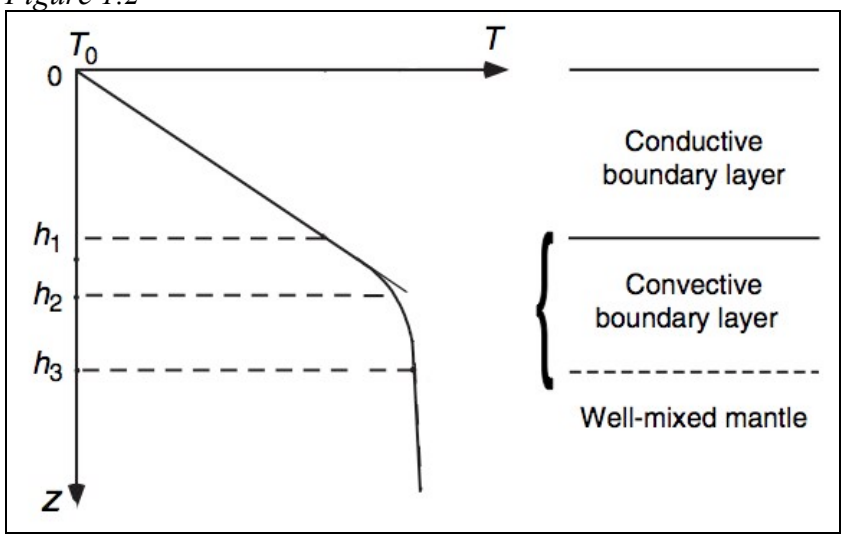

Figure 2.1

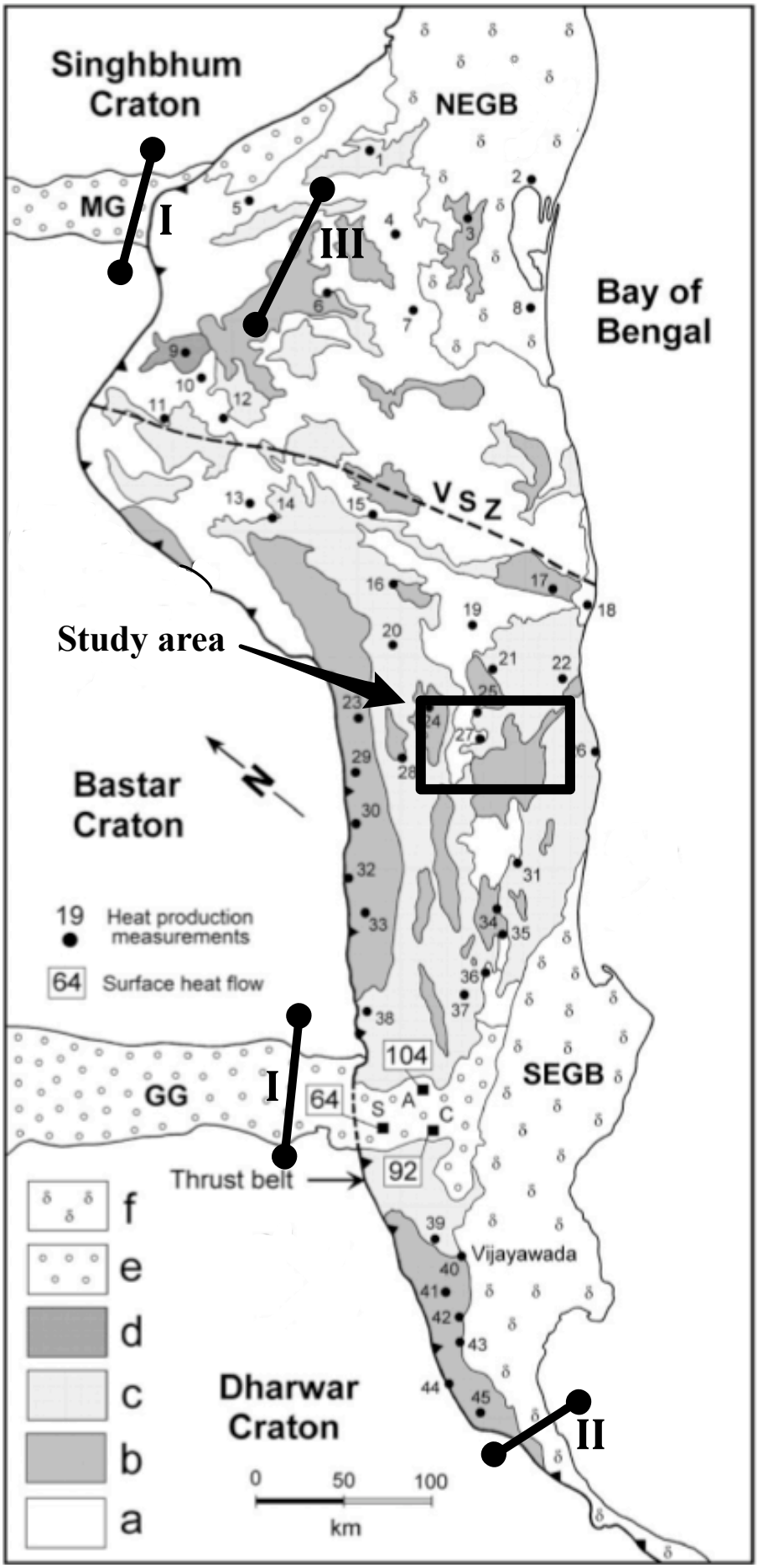
Singhbhum Craton
NEGB
MG
I
III
Bay of Bengal
VSZ
Study area
Bastar Craton
19 Heat production measurements
64 Surface heat flow
GG
I
64
104
SEGB
S
A
C
Thrust belt
92
Vijayawada
Dharwar Craton
II
0 50 100
km
f
e
d
c
b
a

Figure 2.2

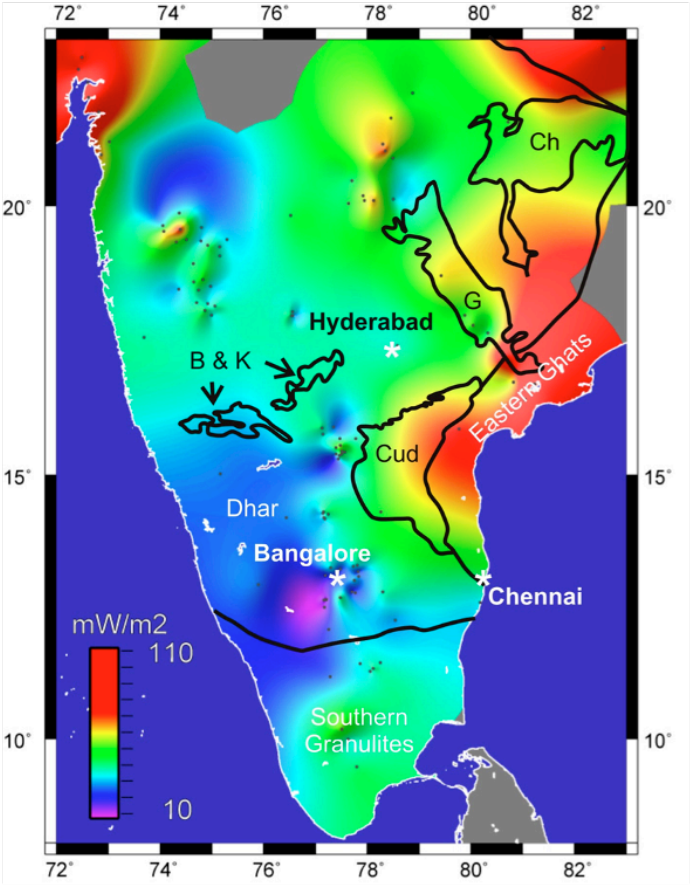

Figure 2.3

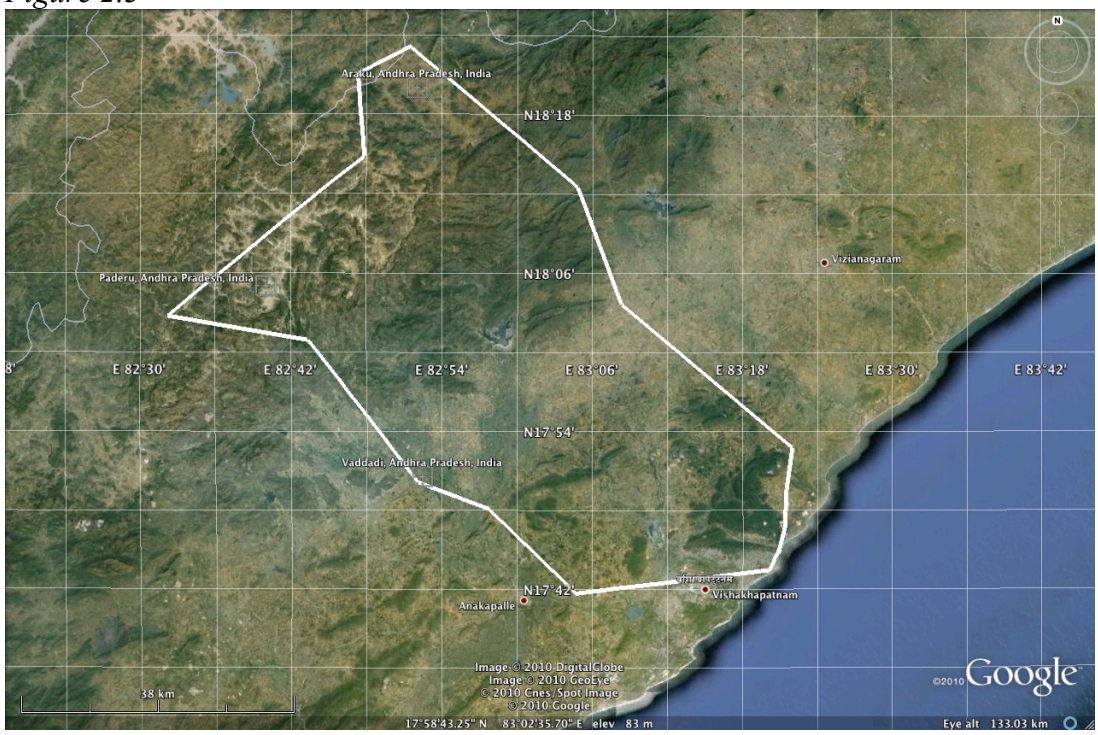

Figure 3.1

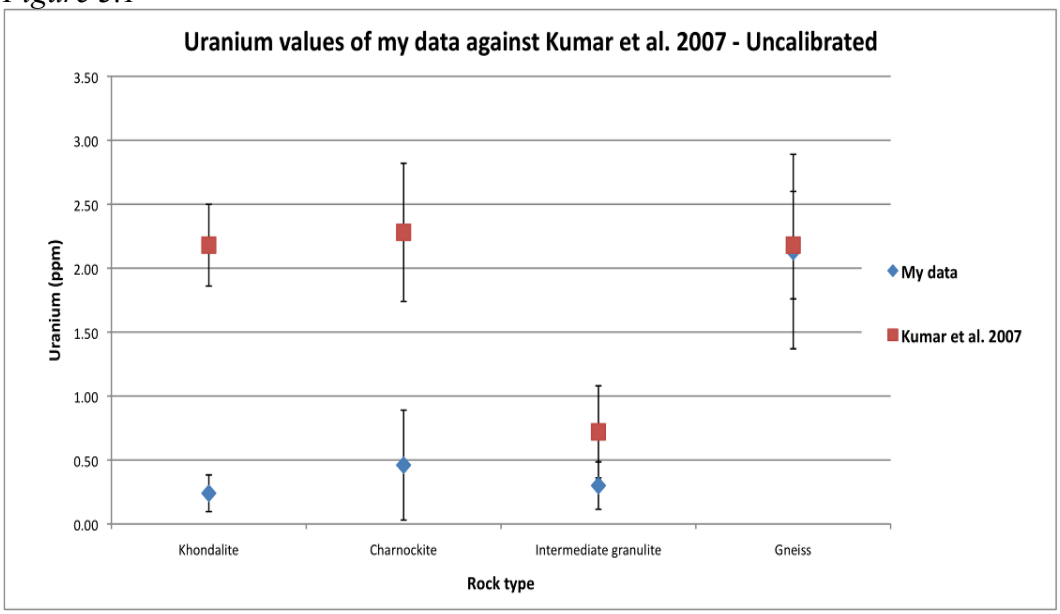

Figure 3.2

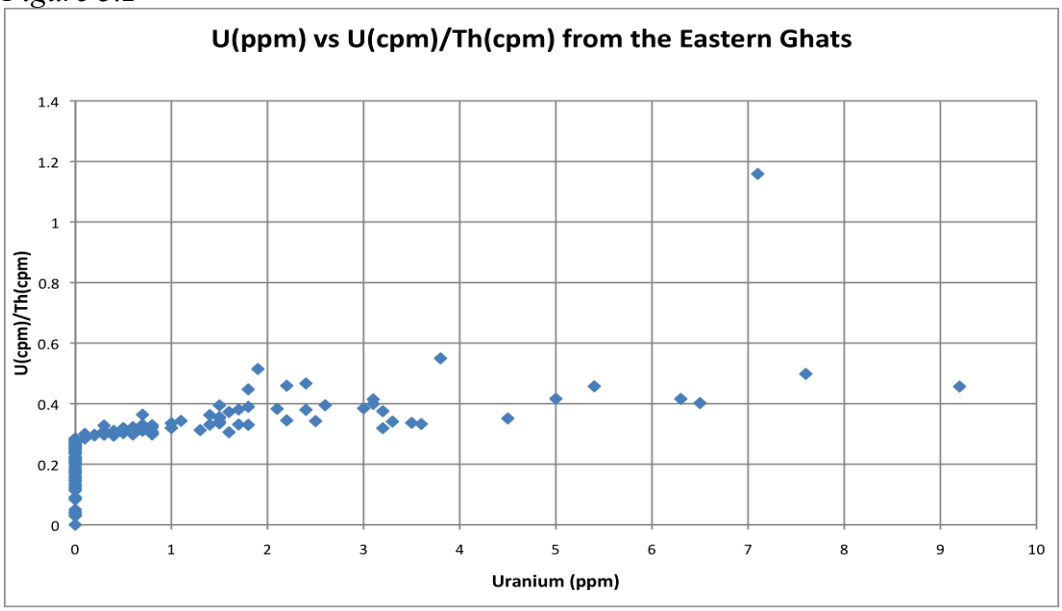

Figure 3.3

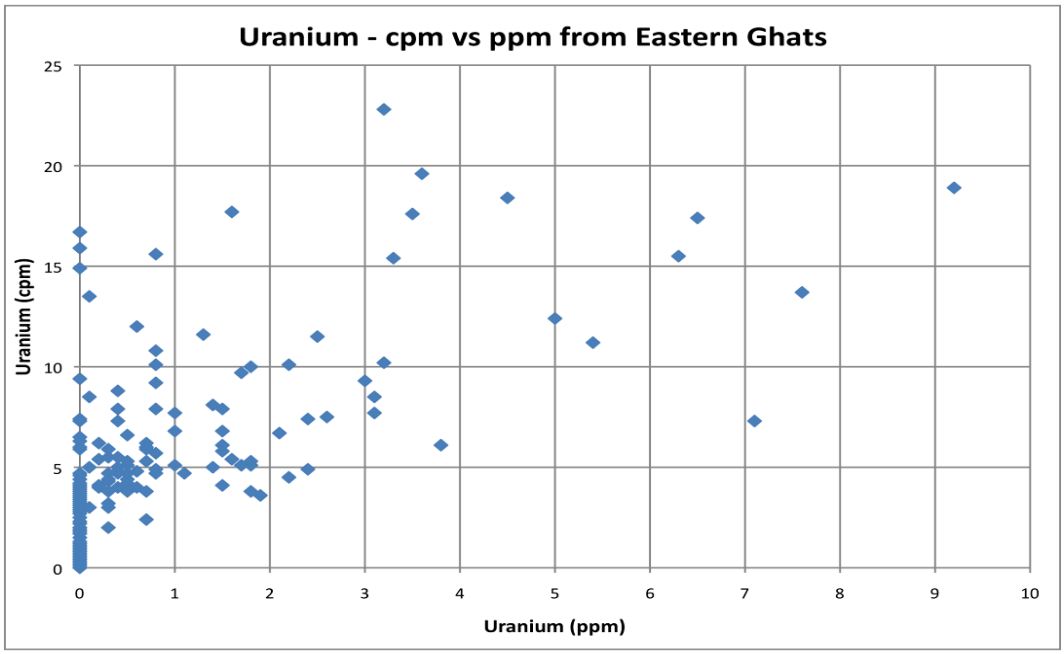
Uranium - cpm vs ppm from Eastern Ghats
Uranium (cpm)
Uranium (ppm)
0
5
10
15
20
25
0
1
2
3
4
5
6
7
8
9
10

Figure 3.4

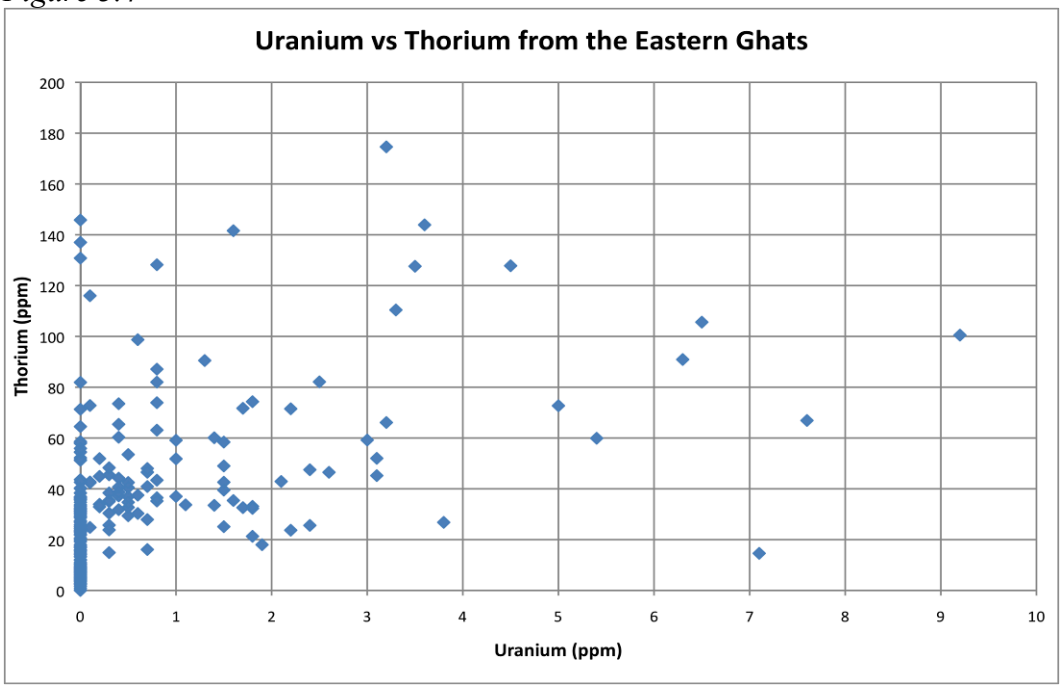
Uranium vs Thorium from the Eastern Ghats
Thorium (ppm)
Uranium (ppm)
0
20
40
60
80
100
120
140
160
180
200
0
1
2
3
4
5
6
7
8
9
10

Figure 3.5

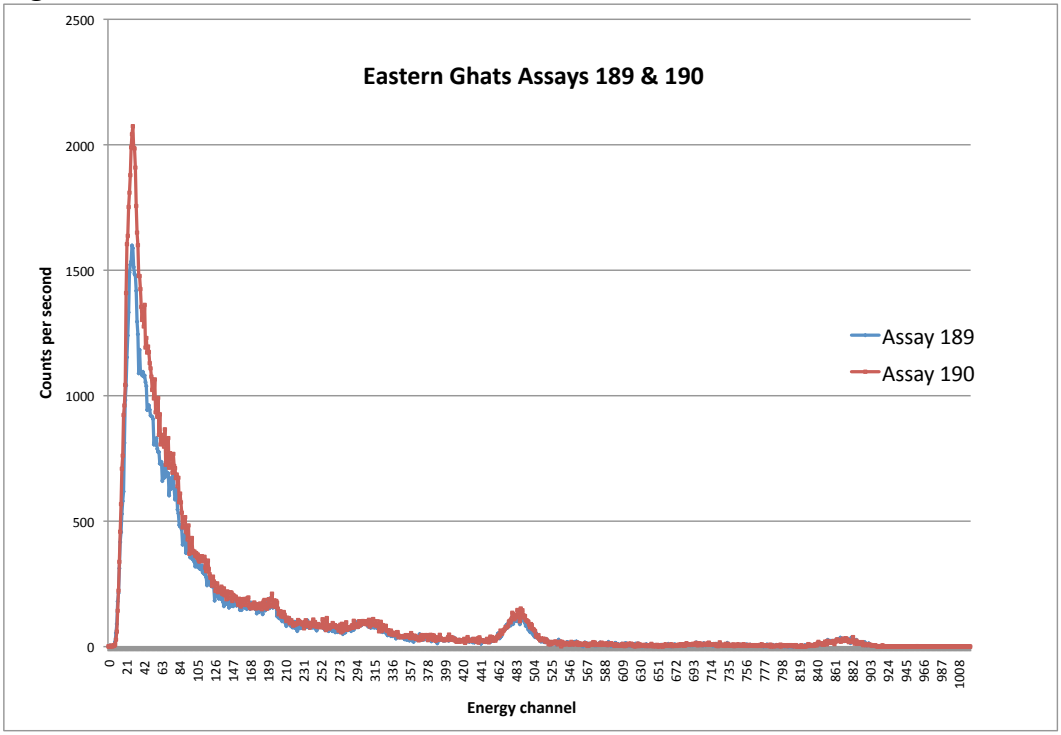

Figure 3.6

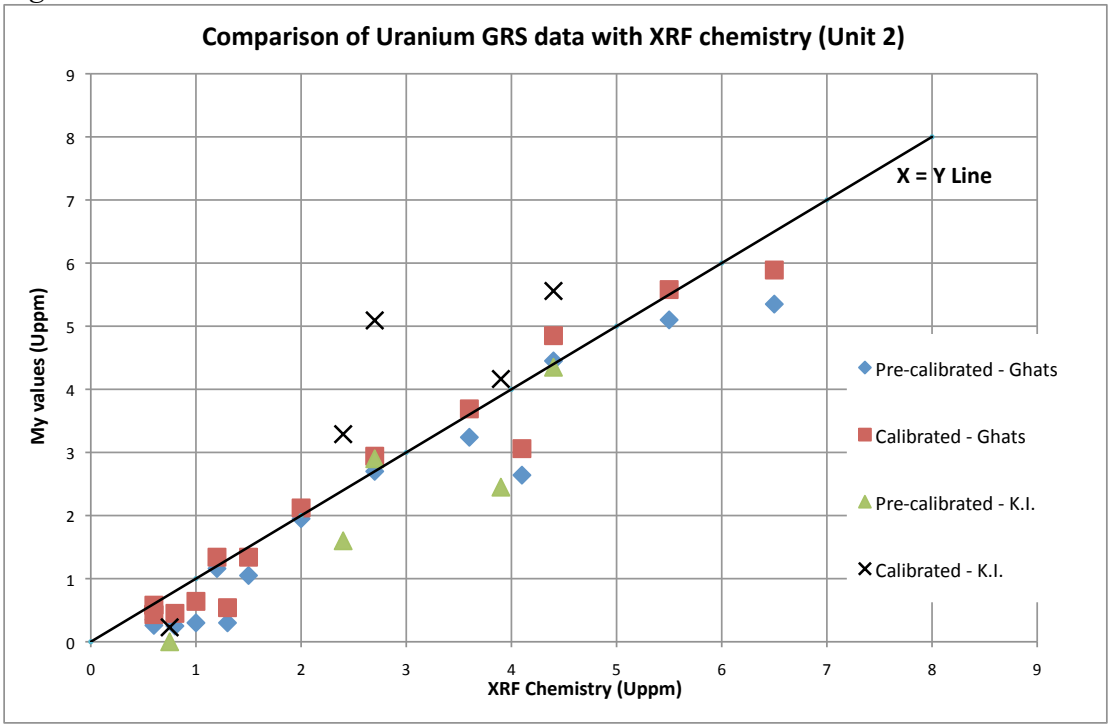

Figure 3.7

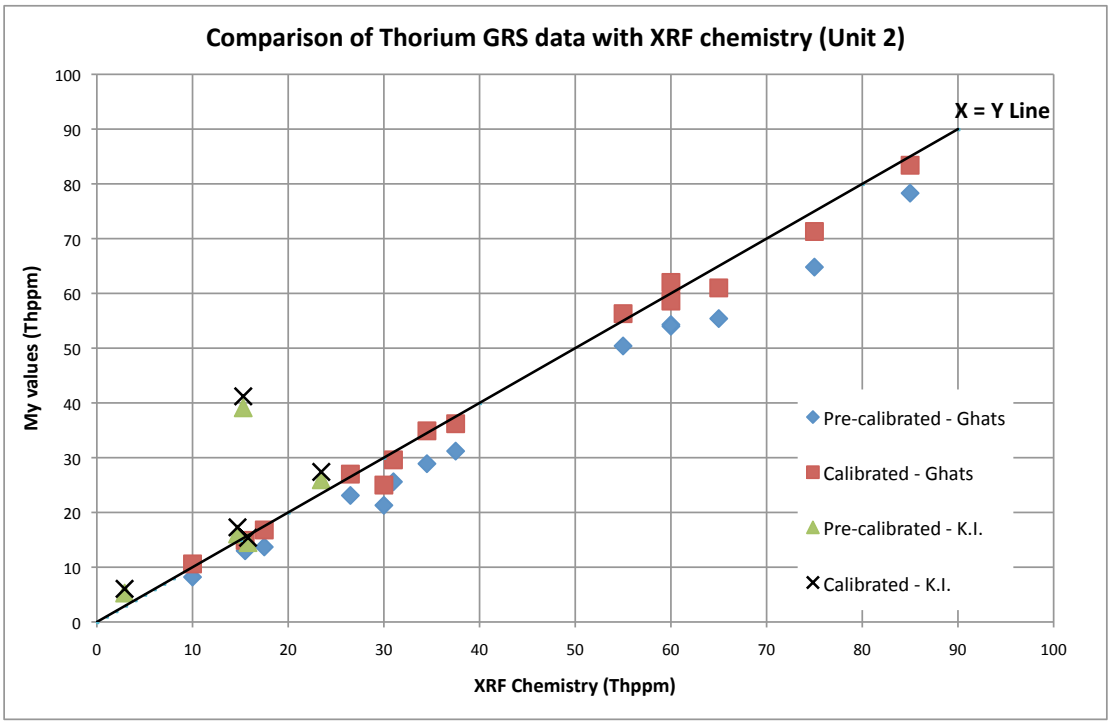

Figure 3.8

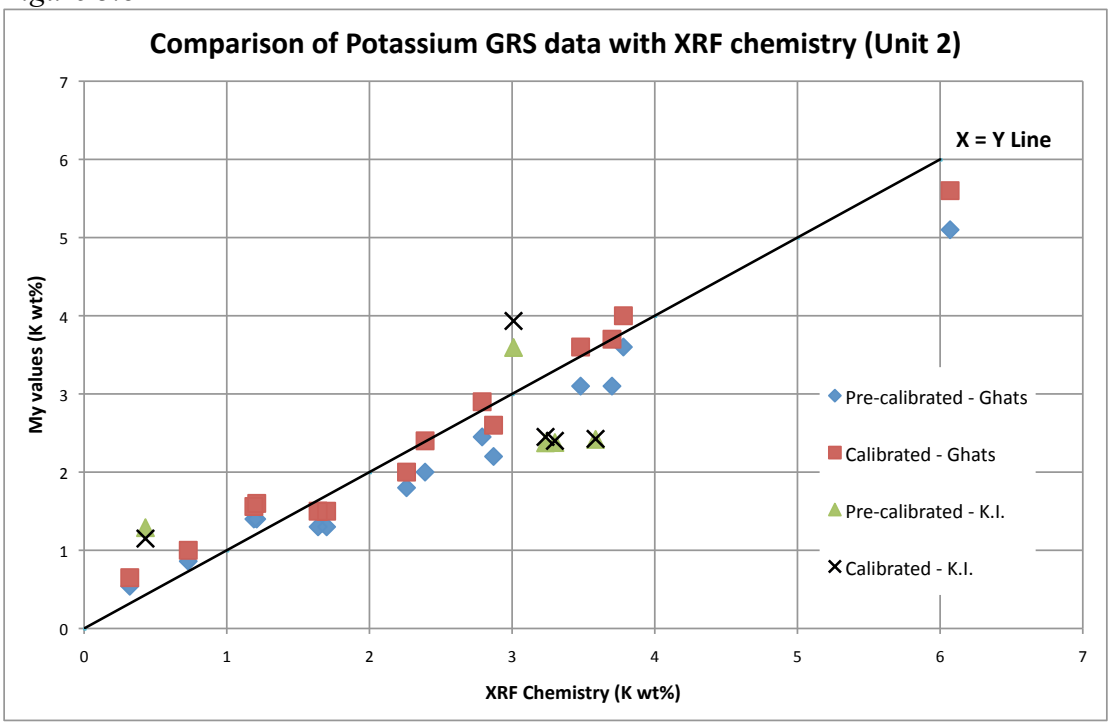

Figure 3.9

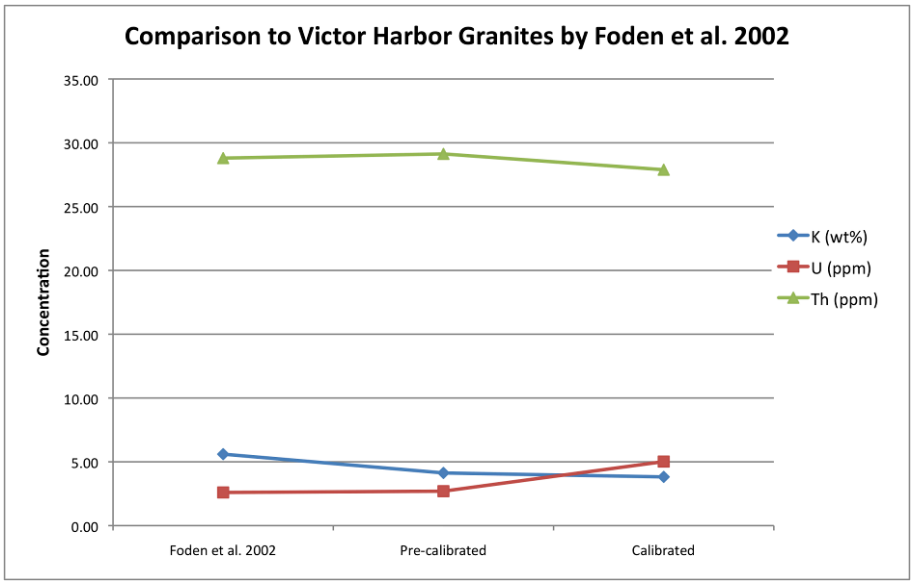

Figure 3.10

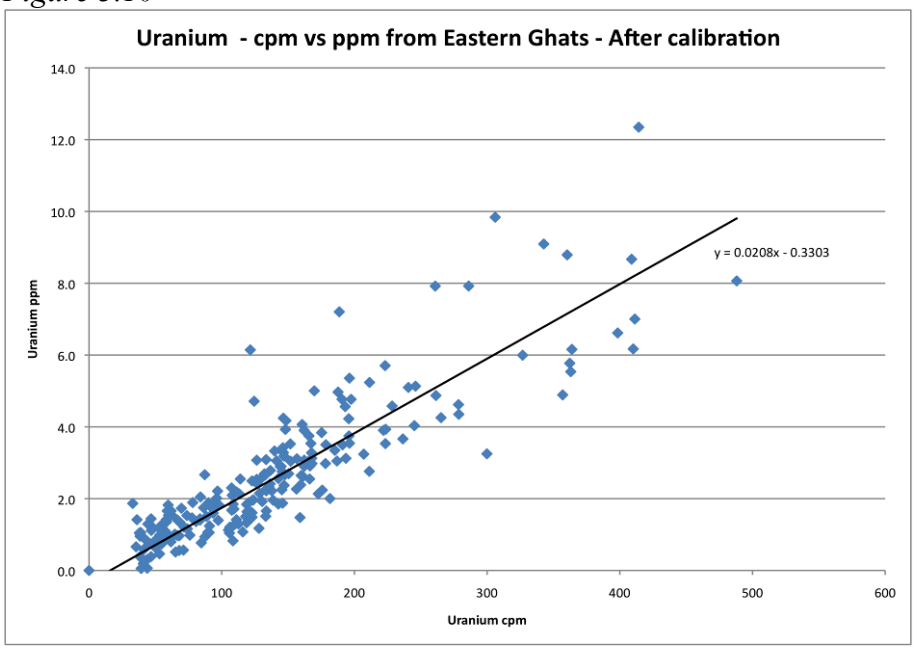

Figure 3.11

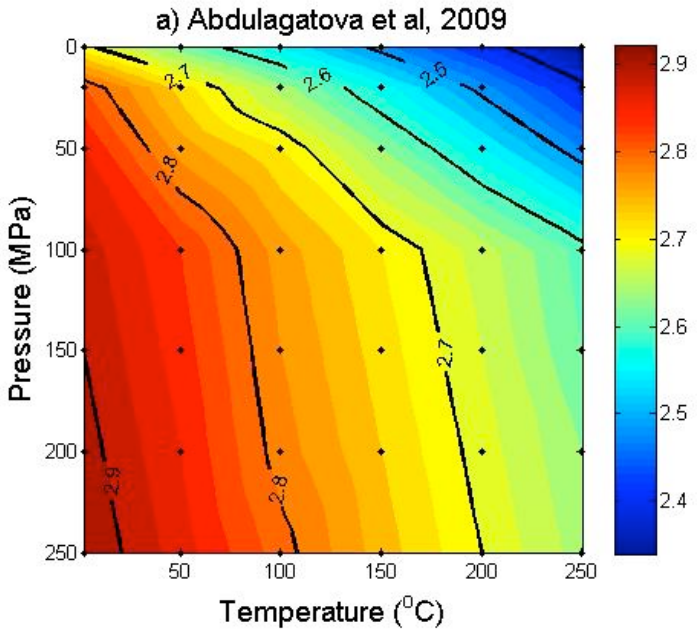

Figure 4.1

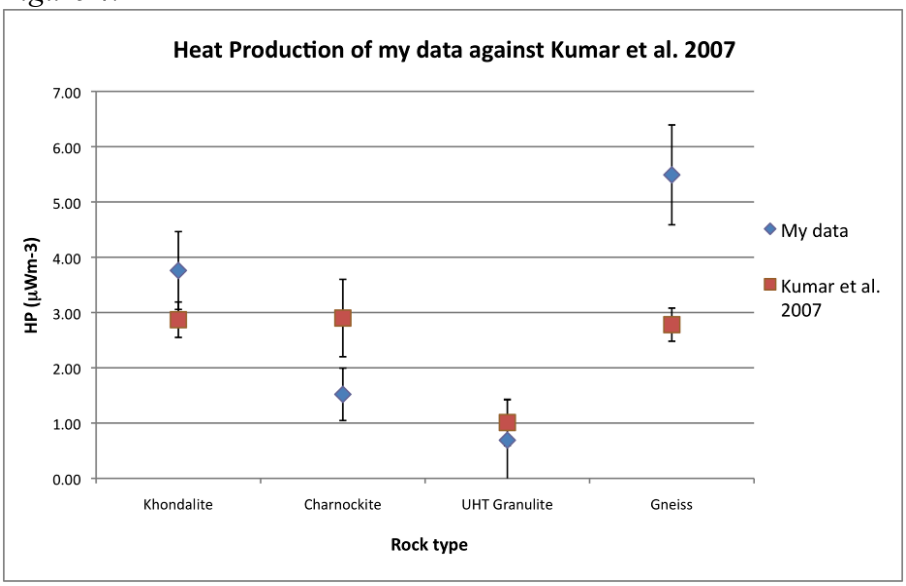

Figure 4.2

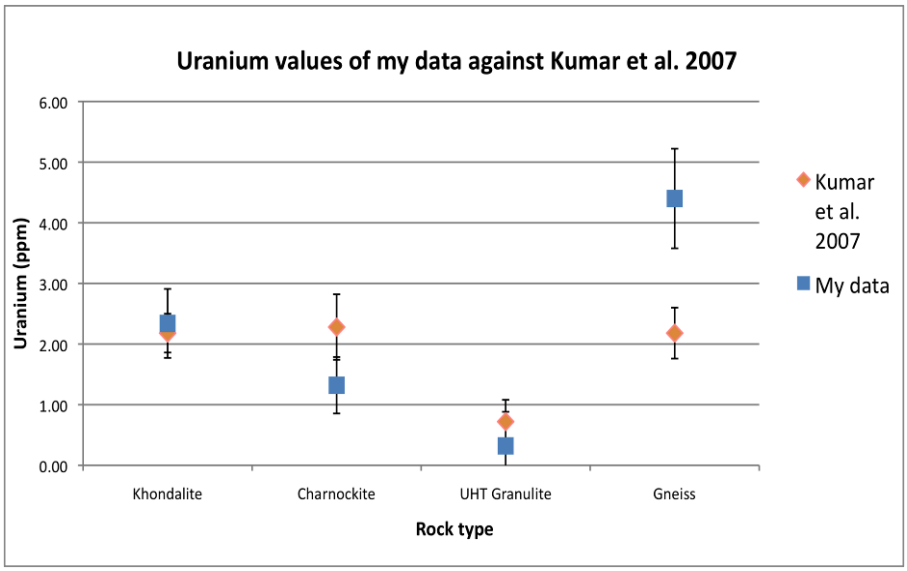

Figure 4.3

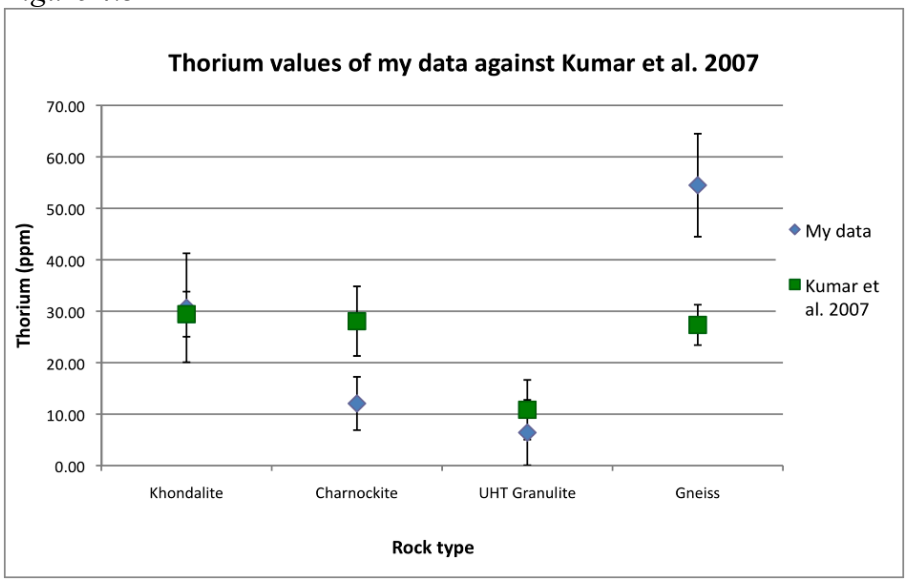

Figure 4.4

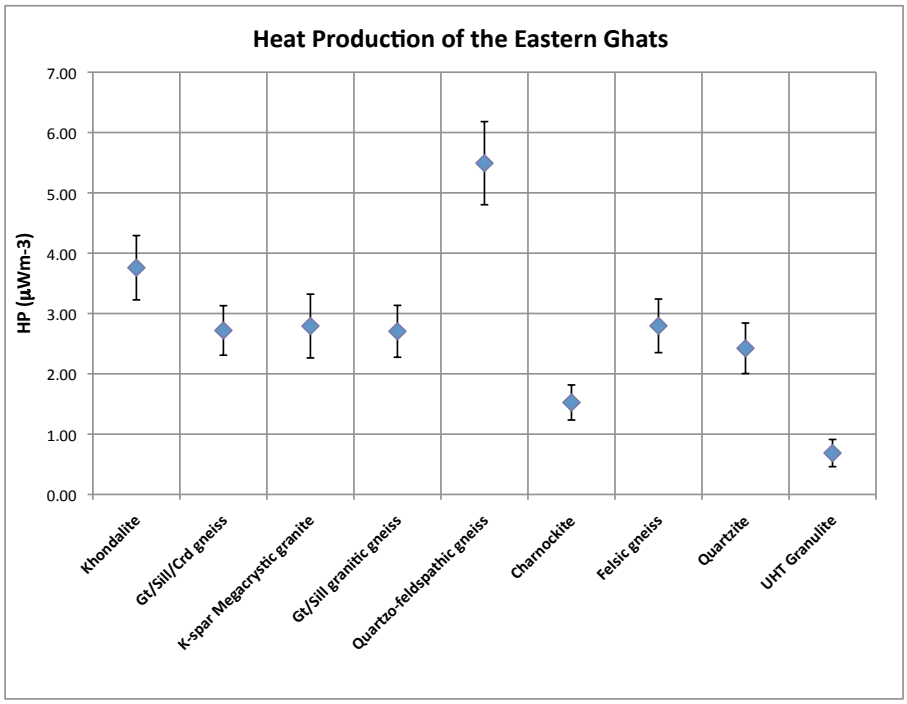

Figure 4.5

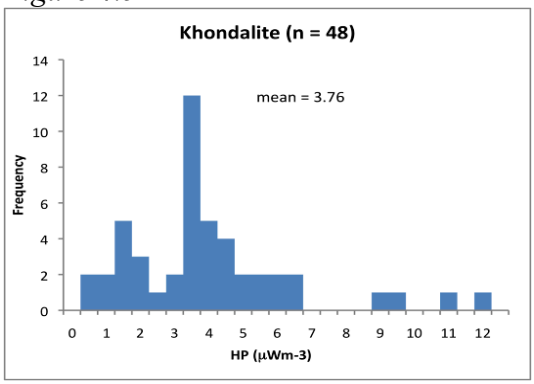

Figure 4.6

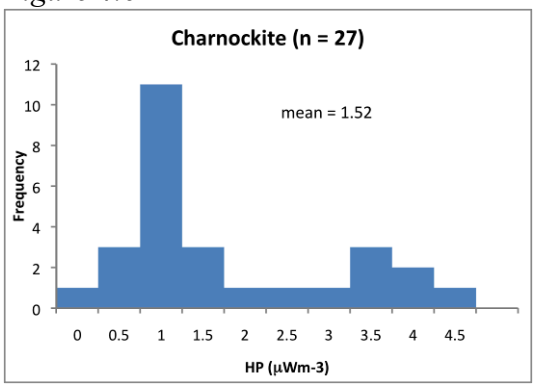

Figure 4.7

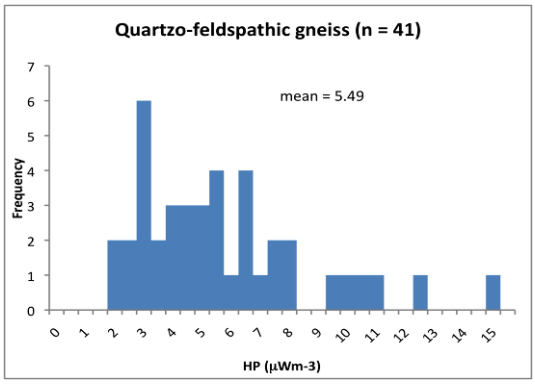

Figure 4.8

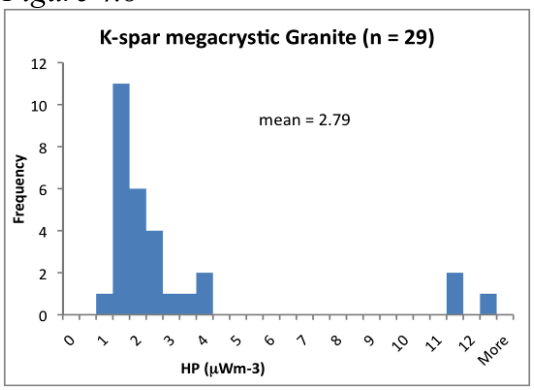

Figure 4.9

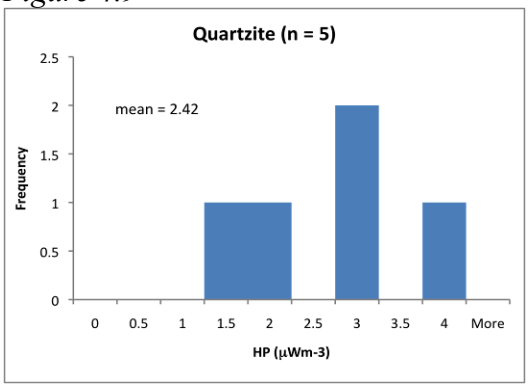

Figure 4.10

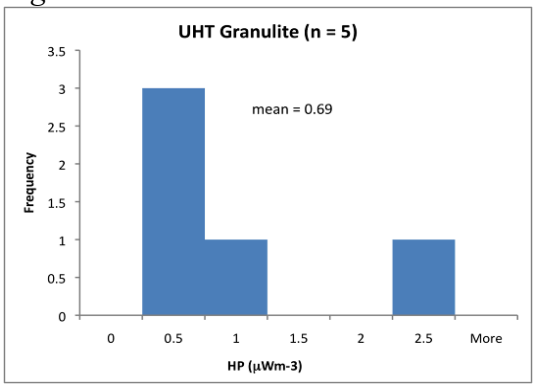

Figure 4.11

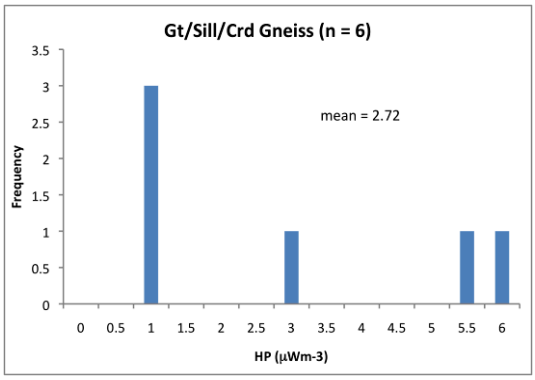

Figure 4.12

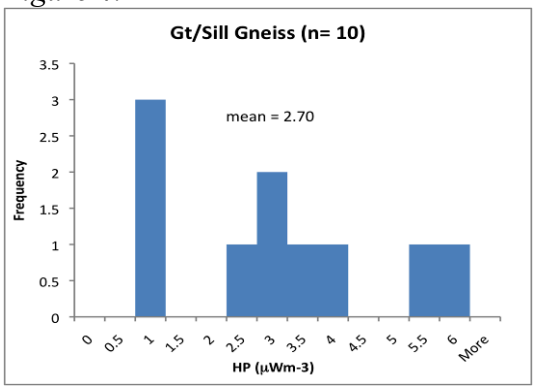

Figure 4.13

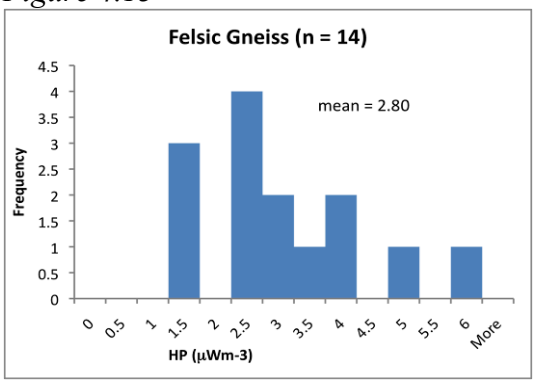

Figure 4.14

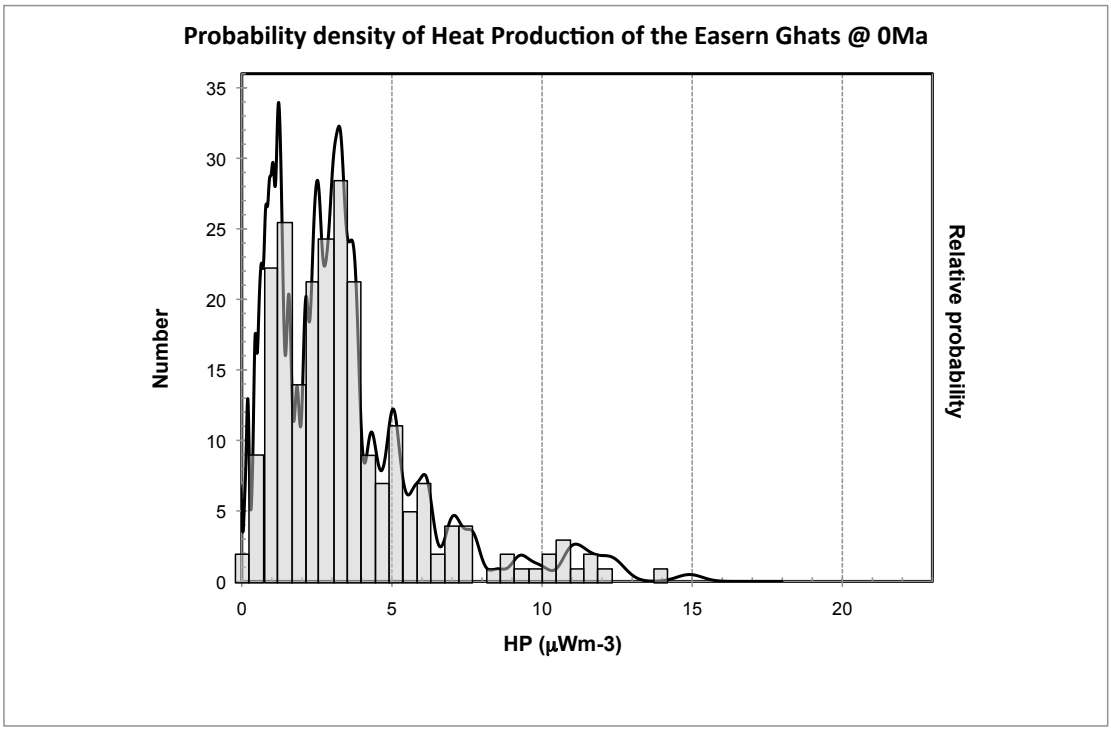
Probability density of Heat Production of the Easern Ghats @ 0Ma
Number
Relative probability
HP (µWm-3)
0
5
10
15
20
25
30
35
0
5
10
15
20

Figure 4.15

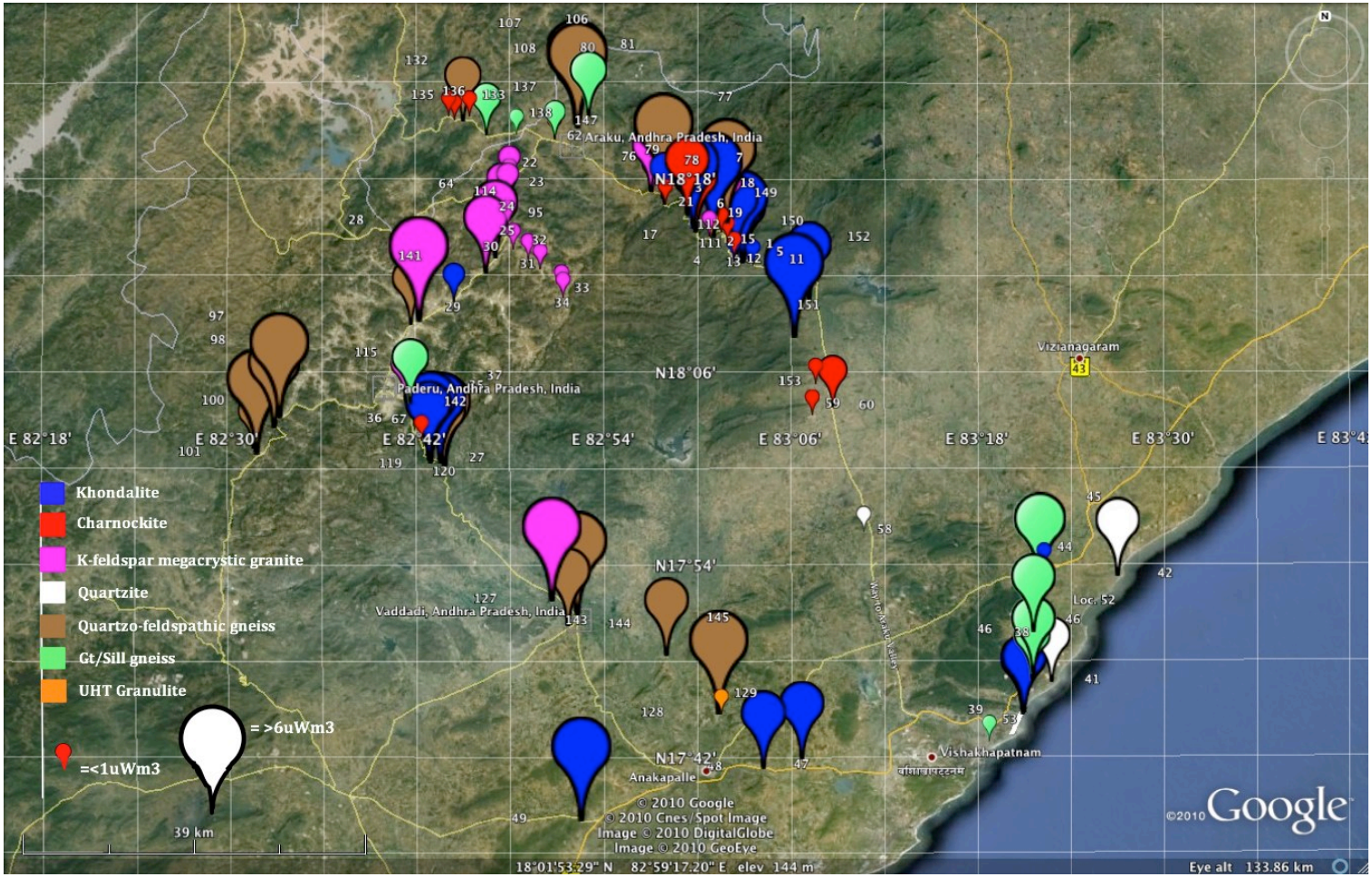
Araku, Andhra Pradesh, India
Paderu, Andhra Pradesh, India
Vaddadi, Andhra Pradesh, India
Anakapalle
Vishakhapatnam
Vizianagaram
N18°18'
N18°06'
N17°54'
N17°42'
E 82°18'
E 82°30'
E 82°42'
E 82°54'
E 83°06'
E 83°18'
E 83°30'
Khondalite
Charnockite
K-feldspar megacrystic granite
Quartzite
Quartzo-feldspathic gneiss
Gt/Sill gneiss
UHT Granulite
= >6uWm3
=<1uWm3
39 km
© 2010 Google
© 2010 Cnes/Spot Image
Image © 2010 DigitalGlobe
Image © 2010 GeoEye
©2010 Google
18°01'53.29" N 82°59'17.20" E elev 144 m
Eye alt 133.86 km

Figure 4.20

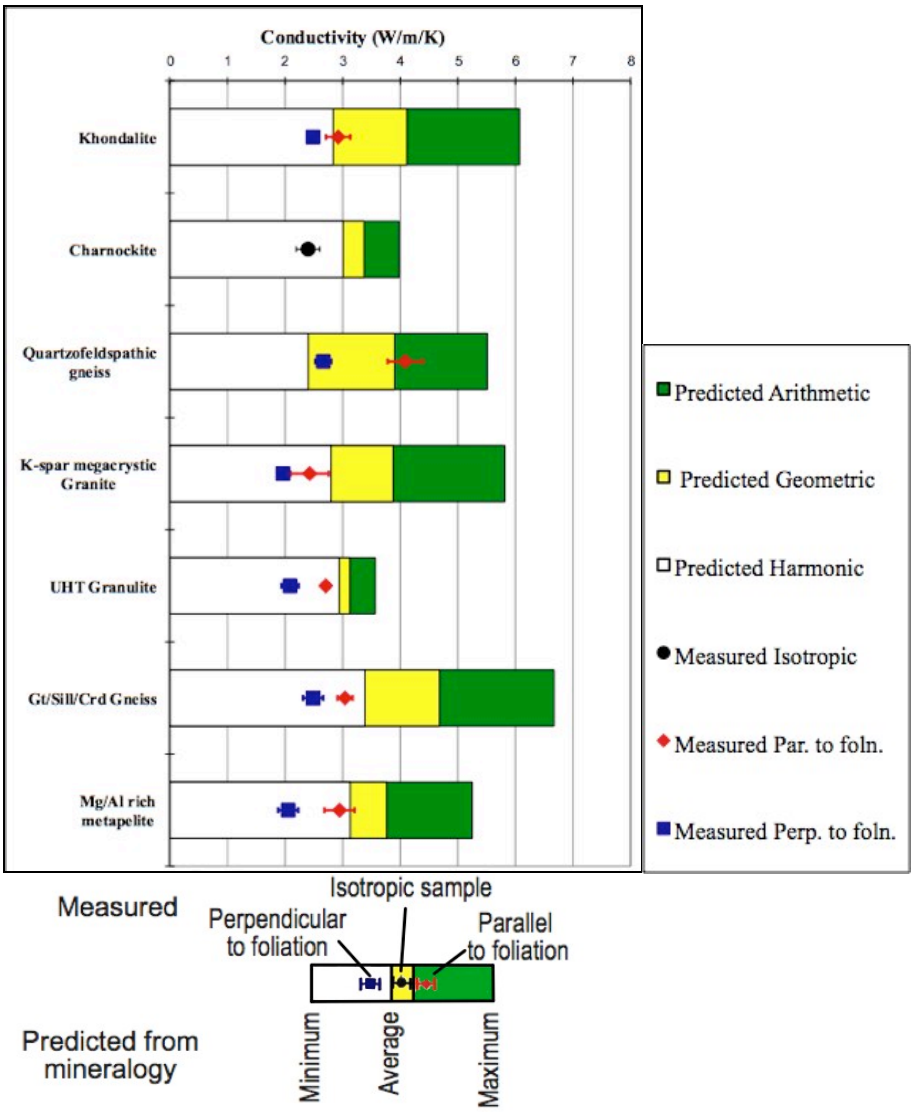

Figure 4.30

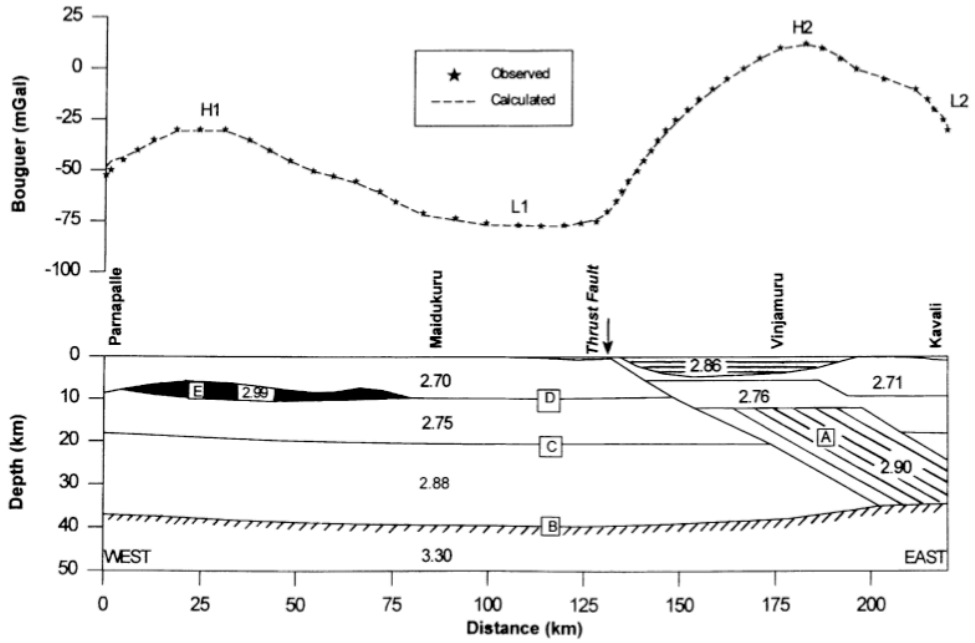
Bouguer (mGal)
Observed
Calculated
H1
H2
L1
L2
Parnapalle
Maidukuru
Thrust Fault
Vinjamuru
Kavali
Depth (km)
2.99
2.70
2.75
2.88
2.86
2.76
2.71
2.90
3.30
WEST
EAST
Distance (km)

Figure 4.31

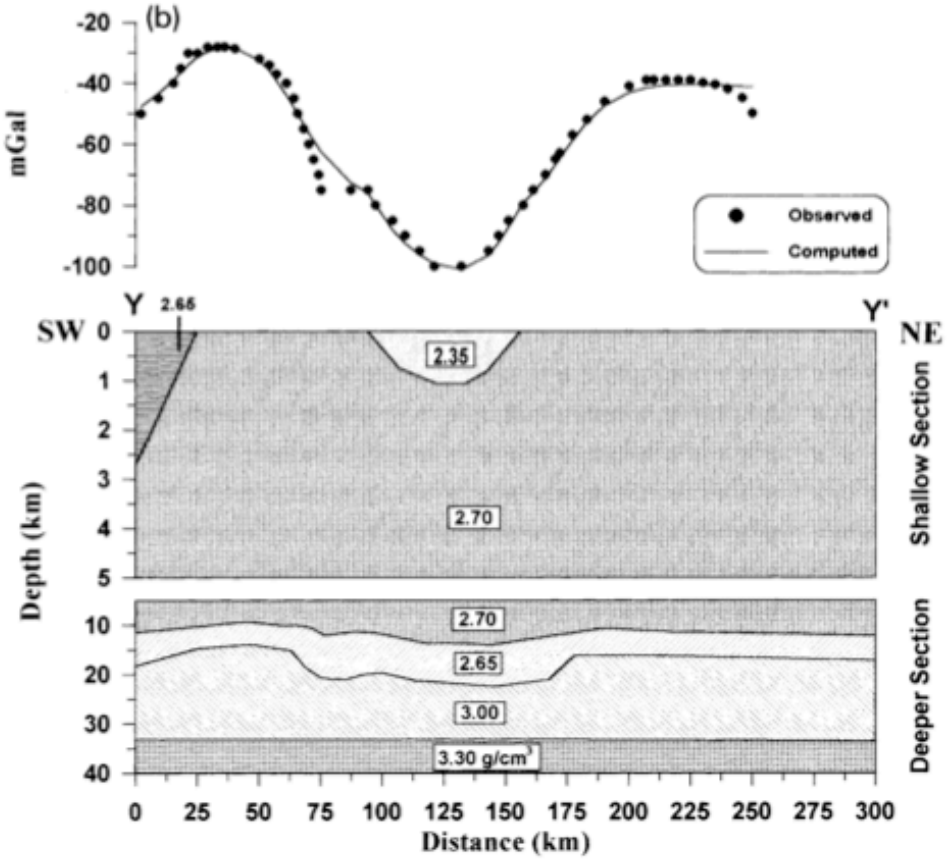
(b)
mGal
Observed
Computed
Y
Y'
2.65
SW
NE
2.35
2.70
Depth (km)
Shallow Section
2.70
2.65
3.00
3.30 g/cm³
Deeper Section
Distance (km)

Figure 4.32

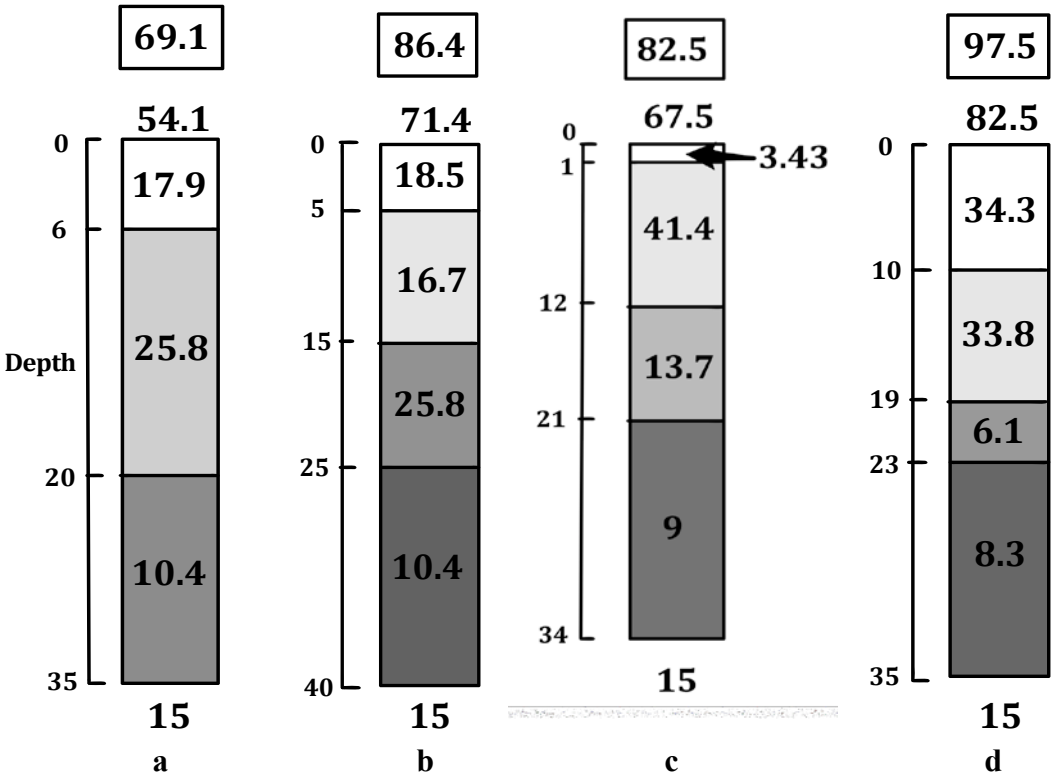

Figure 4.33

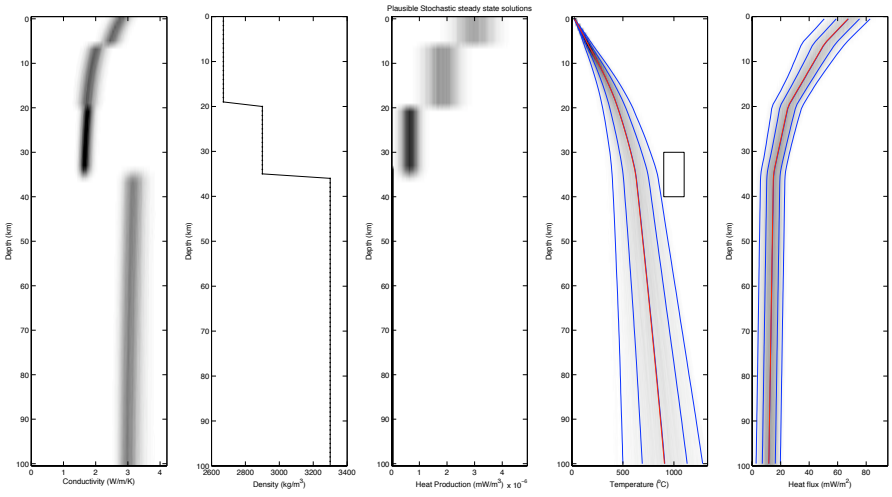

Figure 4.34

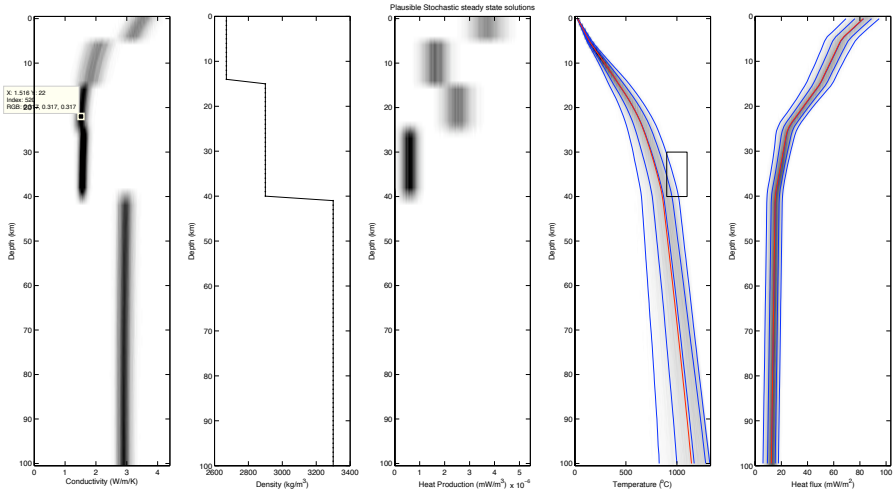

Figure 4.35

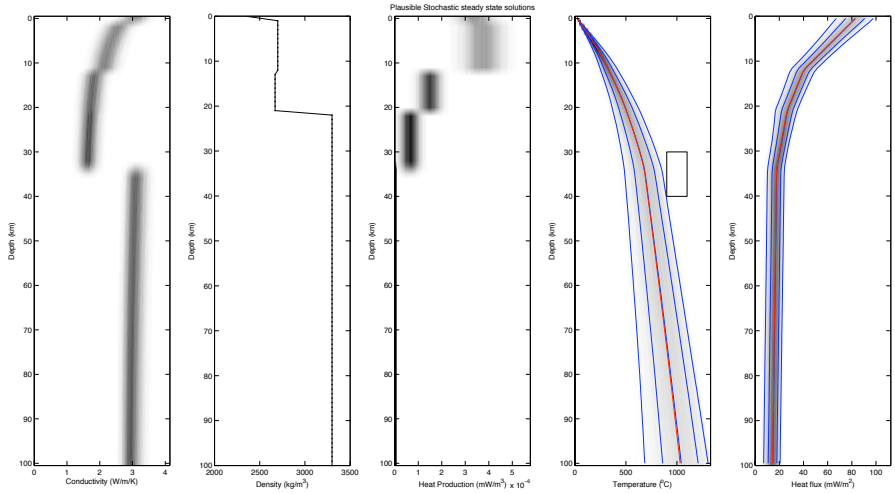

Figure 4.36

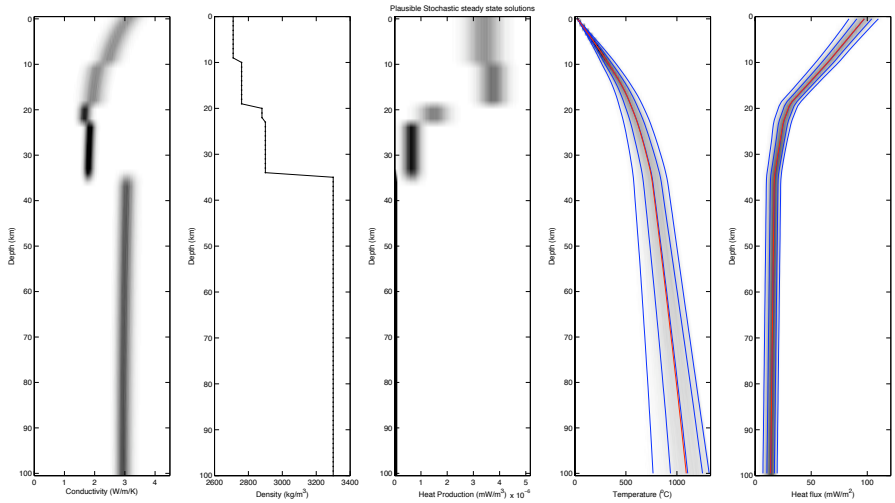

Figure 4.37

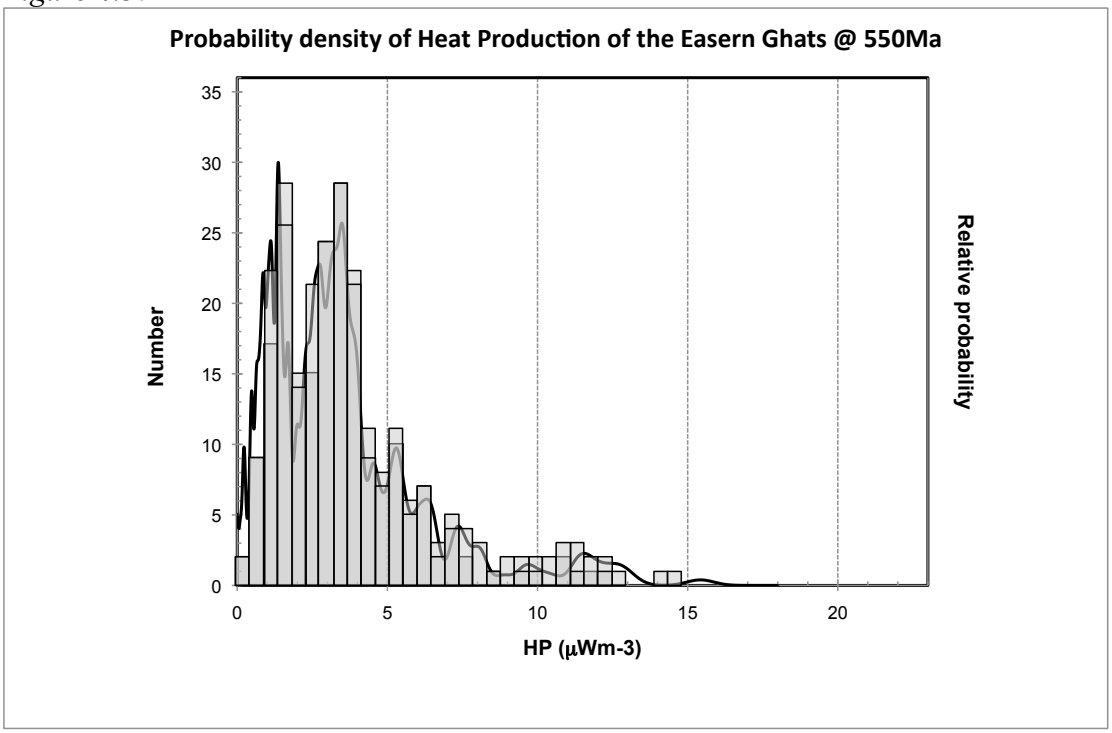

Figure 4.38

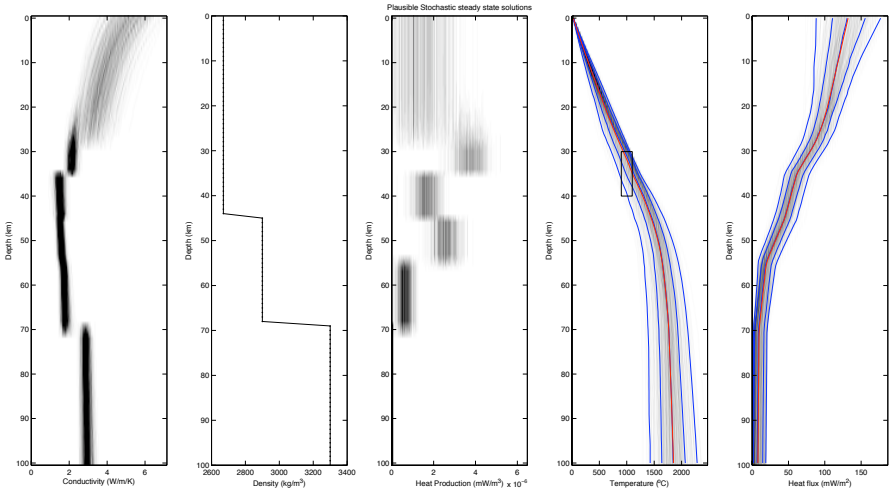

Figure 4.39

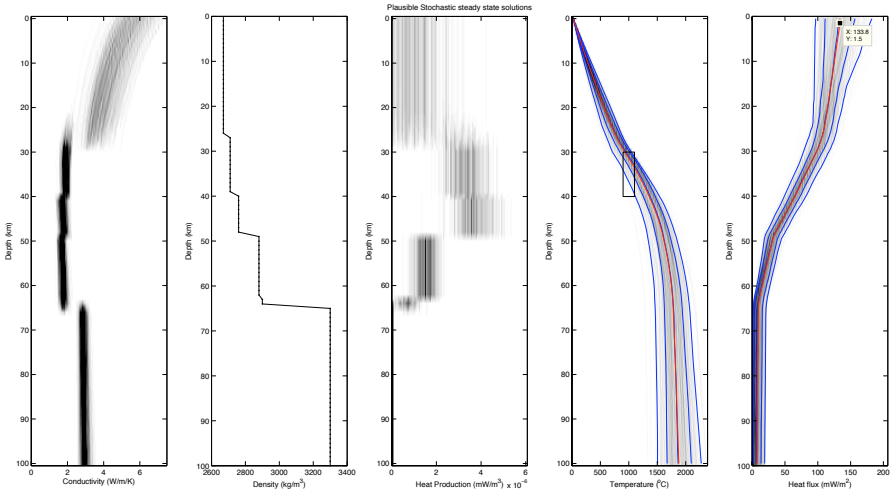

Figure 5.1

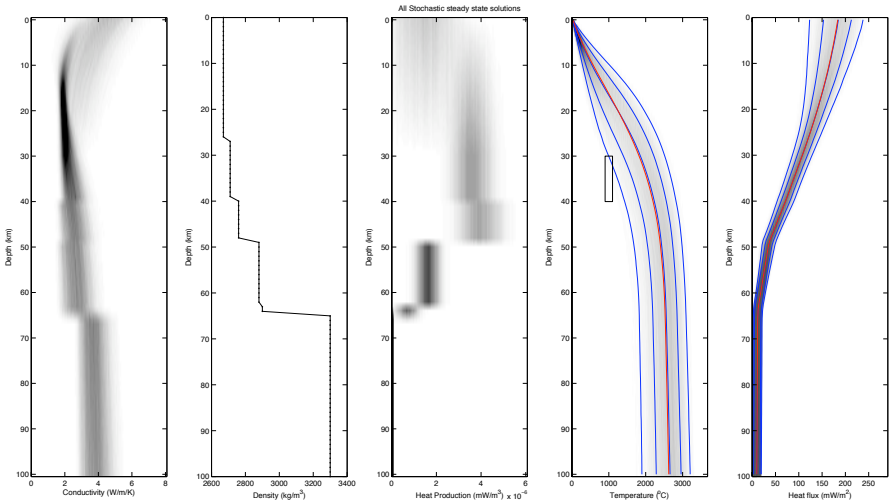

Figure 5.2

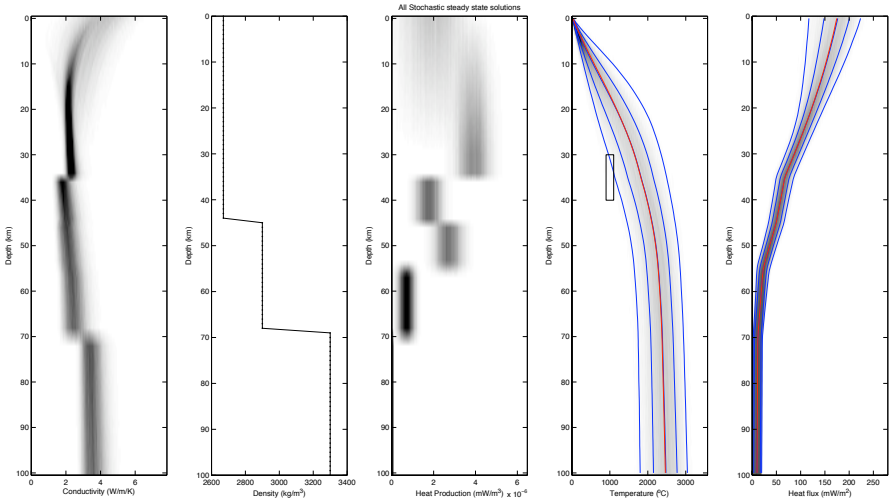

APPENDICES

Appendix 1: Samples from the Eastern Ghats, India.

A1.1 – Sample descriptions

These samples are representative samples of the crust I collected for thermal conductivity testing undertaken by myself at the University of Adelaide.

Sample #	Rock type & Description	Mineralogy	Texture	Location
EG001	**Charnockite** 'Greasy-green', OPX-bearing, vitreous, metaigneous rock.	Quartz, feldspars, pyroxenes and garnet bearing rock. Has subordinate rutile, biotite and amphibole.	Equigranular to slightly porphyritic. Fine to medium grained. Garnets have corona of biotite. Pervasive foliation, defined by K-feldpspar.	N18°03'20.9", E83°07'21.5"
EG002	**Charnockite** 'Greasy-green', OPX-bearing, vitreous, metaigneous rock.	Quartz, feldspars, pyroxenes and garnet bearing rock. Has subordinate rutile, biotite and amphibole.	Equigranular to slightly porphyritic. Fine to medium grained. Garnets have corona of biotite. Migmatitic quartz enclaves.	N18°12'29.3", E83°05'00.7"
EG003	**Mafic gneiss** Garnet/Pyroxene-bearing mafic gneiss.	Quartz, plagioclase, garnet, cordierite, CPX, OPX and subordinate amphibole.	Strongle foliated. Fine to medium grained.	N18°20'29.9", E82°50'51.9"
EG004	**Charnockite** 'Greasy-green', OPX-bearing, vitreous, metaigneous rock.	Quartz, feldspars, pyroxenes and garnet bearing rock. Has subordinate rutile, biotite and amphibole.	Equigranular to slightly porphyritic. Fine to medium grained. Garnets have corona of biotite. Pervasive foliation, defined by K-feldpspar.	N18°20'29.9", E82°50'51.9"
EG005	**Granitic gneiss** Garnet-bearing granite	Quartz, feldspars, garnet, biotite. Subordinate amphibole.	Strongly foliated, equigranular, fine grained.	N18°20'29.9", E82°50'51.9"

EG006	**Gt/Sill gneiss** Partially migmatised gneiss (protolith could have been Khondalite)	Quartz, sillimanite, garnet, feldspars, subordinate OPX and biotite.	Strong foliation defined by sillimanite and K-feldspar. Fine grained.	N18°01'03.1", E82°42'37.2"
EG007	**K-feldspar megacrystic granite** Metaigneous, intermediate garnet-bearing granulite	Quartz, K-feldspar, biotite, plagioclase feldspar, garnet, and subordinate graphite.	Varying degrees of migmatisation and foliation, and in some areas contained enclaves of metasedimentary rocks. Porphyritic (megacrystic) K-feldspar grains up to 10cm in some areas. Medium grained.	N18°15'45.5", E82°47'20"
EG008	**Quartzo-feldspathic gneiss** Felsic garnet-bearing gneiss	Quartz, K-feldspar, garnet, biotite, subordinate muscovite.	Strongly foliated, fine-grained rock. Platy minerals define foliation.	N18°03'15.9", E82°33'20.1"
EG009	**Quartzo-feldspathic gneiss** Felsic garnet-bearing gneiss	Quartz, K-feldspar, garnet, biotite, subordinate muscovite.	Strongly foliated, fine-grained rock. Platy minerals define foliation.	N18°21'28.1", E18°52'20.5"
EG010	**Khondalite** Garnet/Sillimanite bearing metasedimentary rock.	Quartz, K-feldspar, oligoclase, biotite, garnet, sillimanite and subordinate graphite, cordierite, sphene, and apatite.	Slightly gneissic fabric defined by garnet and sillimanite. Fine to medium grained.	N18°14'24", E83°00'44.6"

These samples are representative samples I collected for thermal conductivity testing undertaken by Sukanta Roy at NGRI, Hyderabad, India.

Sample #	Rock type & Description	Mineralogy	Texture	Location
ABEG011	**UHT Granulite** Mafic granulite	Plagioclase feldspar, CPX, OPX, garnet, amphibole, cordierite, sphene, spinel and subordinate K-feldspar.	Fine grained, with large enclaves of cordierite and sphene. Massive texture.	N17°44'44.7", E83°01'20"
ABEG012	**Leptynite** Metamorphosed quartz/K-feldspar sedimentary rock.	Quartz, K-feldspar	Coarse grained – porphyritic. Massive.	N17°46'44.7", E83°00'20"
ABEG013	**GT/Crd/OPX Gneiss**	Quartz, garnet, OPX, cordierite, K-feldspar, biotite, plagioclase and subordinate sillimanite and graphite.	Fine to medium grained. Strongly foliated. Equigranular.	N17°43'44.7", E83°02'20"
ABEG014	**K-feldspar megacrystic granite** Metaigneous, intermediate garnet-bearing granulite	Quartz, K-feldspar, biotite, plagioclase feldspar, garnet, and subordinate graphite.	Varying degrees of migmatisation and foliation, and in some areas contained enclaves of metasedimentary rocks. Porphyritic (megacrystic) K-feldspar grains up to 10cm in some areas. Medium grained.	N17°51'50.2", E82°50'38.1"
ABEG015	**Quartzo-feldspathic gneiss** Felsic garnet-bearing gneiss	Quartz, K-feldspar, garnet, biotite, subordinate muscovite.	Strongly foliated, fine-grained rock. Platy minerals define foliation.	N17°50'56.5", E82°52'16.4"
ABEG016	**K-feldspar megacrystic**	Quartz, K-feldspar, biotite, plagioclase	Varying degrees of migmatisation and foliation, and	N18°20'25.7", E82°50'53.1"

	granite Metaigneous, intermediate garnet-bearing granulite	feldspar, garnet, and subordinate graphite.	in some areas contained enclaves of metasedimentary rocks. Porphyritic (megacrystic) K-feldspar grains up to 10cm in some areas. Medium grained.	
ABEG017	**Gt/Sill/Crd gneiss** Partially migmatised gneiss (protolith could have been Khondalite)	Quartz, sillimanite, cordierite, garnet, feldspars, subordinate OPX and biotite.	Strong foliation defined by sillimanite and K-feldspar. Fine grained.	N18°21'43.9", E82°52'30.1"
ABEG018	**Gt/Sill/Crd gneiss** Partially migmatised gneiss (protolith could have been Khondalite)	Quartz, sillimanite, cordierite, garnet, feldspars, subordinate OPX and biotite.	Strong foliation defined by sillimanite and K-feldspar. Fine grained.	N18°21'44.9", E82°52'33.1"
ABEG019	**Khondalite** Garnet/Sillimanite bearing metasedimentary rock.	Quartz, K-feldspar, oligoclase, biotite, garnet, sillimanite and subordinate graphite, cordierite, sphene, and apatite.	Slightly gneissic fabric defined by garnet and sillimanite. Fine to medium grained.	N18°14'46", E83°03'55.6"
ABEG020	**Khondalite** Garnet/Sillimanite bearing metasedimentary rock.	Quartz, K-feldspar, oligoclase, biotite, garnet, sillimanite and subordinate graphite, cordierite, sphene, and apatite.	Slightly gneissic fabric defined by garnet and sillimanite. Fine to medium grained.	N18°15'45", E83°01'34"

Figure A1.1 is a map of sample locations.

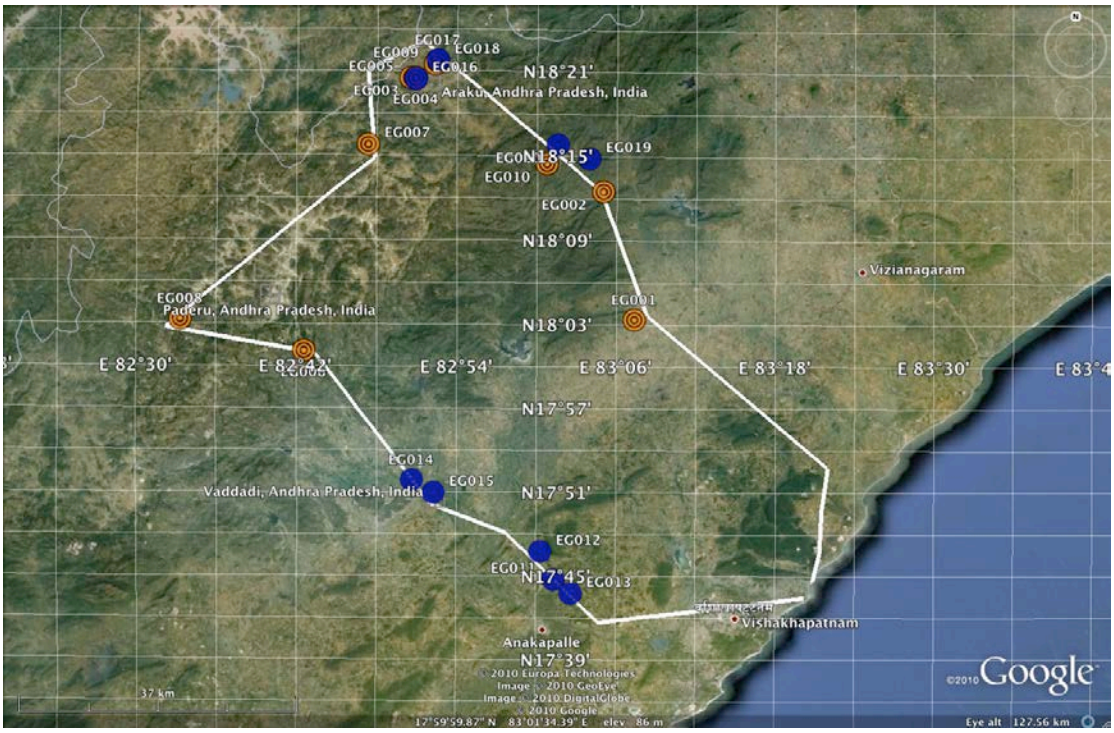

Figure A1.1 – Sample locations for thermal conductivity measurements. Orange dots represent the samples I examined, and the blue dots represent the samples sent to NGRI, Hyderabad for thermal conductivity testing.

A1.2 – Photographic record

A photographic record was taken of each whole rock sample (that I measured) before preparation, as well as selected shots of the cut rocks to demonstrate the geometries used for thermal conductivity tests. A Canon Ixus 100IS was used, with the rock against a neutral background.

EG001 – Charnockite

EG002 - Charnockite

EG003 – Mafic gneiss

EG004 - Charnockite

EG005 – Granitic gneiss

EG006 – Garnet/Sillimanite gneiss

EG007 – K-feldspar megacrystic granite

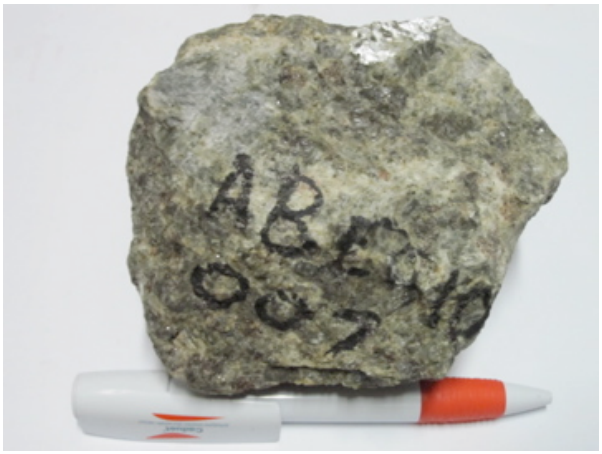

EG008 – Quartzo-feldspathic gneiss

EG009 – Quartzo-feldspathic gneiss

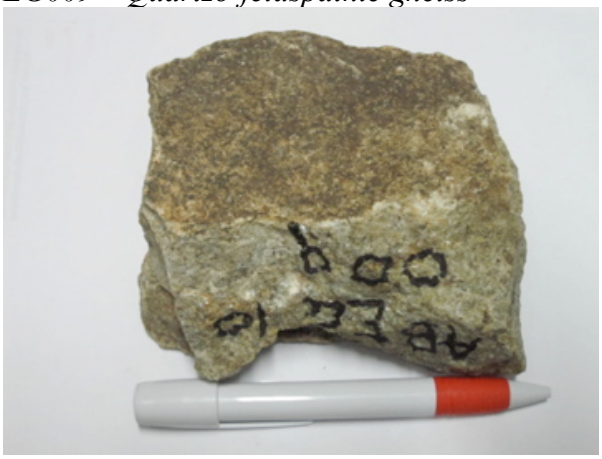

EG010 - Khondalite

Sample EG001 cut into cubes.

Sample EG002 cut into cubes and flattened cubes.

Sample EG003 cut into various geometries.

Sample EG006 cut into different sized geometries.

Appendix 2: Calibration of Portable Gamma Ray Spectrometers

A2.1 – Background and Theory

The University of Adelaide was recently awarded a grant by the South Australian Government to establish the South Australian Centre for Geothermal Energy Research (SACGER) to achieve its target of 33% renewable energy production by 2020 (http://www.adelaide.edu.au/geothermal/). There are also a number of staff and students in Geology and Geophysics, and the Australian School of Petroleum that are currently undertaking studies that involve geothermal energy research. To this end, the University of Adelaide recently bought three portable gamma-ray spectrometers (GRS's) that are currently being used in active projects in India and South Australia to aid in the acquisition of radiogenic heat production data for geothermal oriented projects.

Gamma rays are electromagnetic radiation similar to visible light (wavelength of 10^{-6}m) (Serra 1984b), having a high frequency/energy (10^{19}Hz) and short wavelength (10^{-12}m), which is detected by a sodium-iodide or bismuth-germanium oxide detector crystal. Gamma rays interact with the crystal to generate a flash of detectable photons that are transformed into voltage pulses by an amplifier and photomultiplier (Ketcham 1996a). This information is then transmitted to a multichannel analyser that determines the energy of the gamma ray, and results in a visible spectral signature used to quantify the decaying isotope.

The energy regions that are associated with the detection of specific radiogenic isotopes are listed in table 3.1. Typical spectra for each radioelement are shown below in Figure A2.1, and the combined photopeaks used to identify these elements are shown in Figure A2.1d.

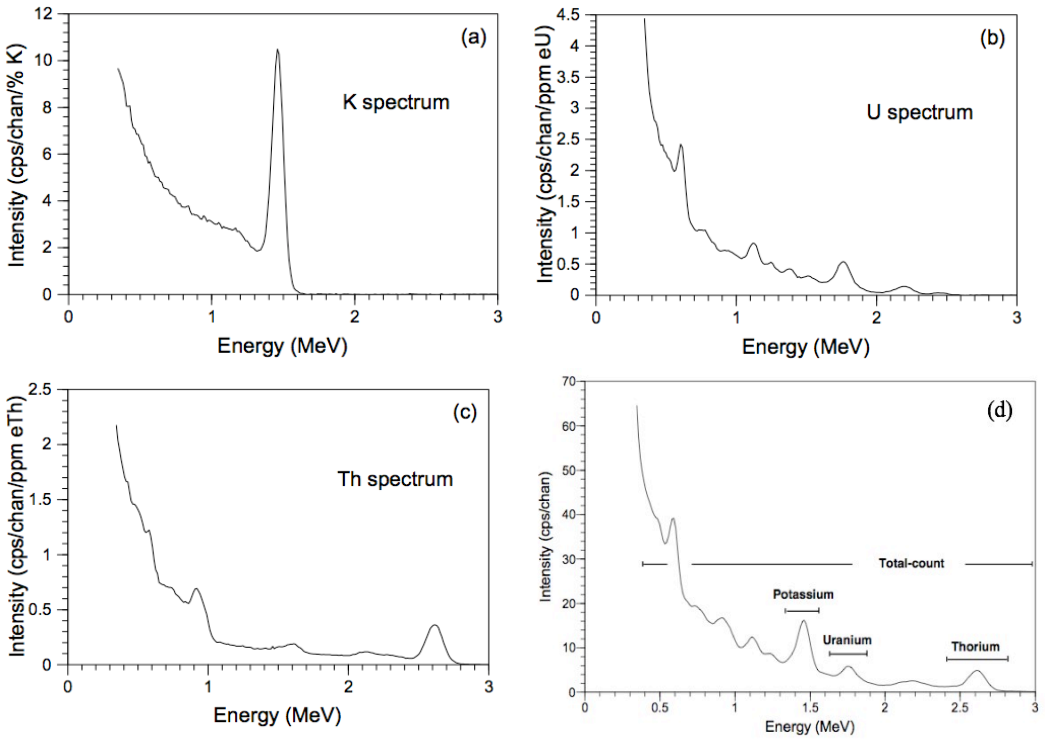

Figure A2.1. – The gamma ray spectra for radioelements of interest from IAEA (2003). The y-axis measures the 'intensity', which are cs^{-1} per channel. The x-axis is energy of gamma radiation; most GRS's have 256, 512 or 1024 channels between 0 and 3.0MeV. The intensity for the three photopeaks of K, U & Th determines the over all cs^{-1}, and from this the concentration can be calculated. a) Potassium, b) Uranium, c) Thorium d) Example of combined spectra of an assay, showing energy windows used by gamma ray spectrometers to calculate element concentrations.

Several authors describe a common problem with detecting uranium and thorium levels known as secular disequilibrium. This occurs when one or more decay products in a decay series are completely or partially removed or added by oxidisation, and can result in gross underestimations of uranium and sometimes thorium. Concentrations are based on the measurements of gamma rays emitted during the decay of ^{214}Bi and ^{208}Tl for uranium and thorium respectively. Potassium has no problems with disequilibrium, as GRS's directly measure gamma rays emitted by ^{40}K decaying to ^{40}Ar. Serra (1984)a states that the transport of uranium occurs in solution as complex carbohydrates and sulphates, in suspension in minerals (zircon and monazite) and in organisms that accumulate the element in their thyroid glands. Uranium is precipitated by reducing agents such as organic matter, platy minerals,

sulphur, phosphates and an acidic pH. It exists in two valencies: U^{4+} and U^{6+}. U^{4+} has a tendency to oxidize and become U^{6+}, forming U_2O_7, and UO_4, which are found in acidic (pH < 4.5) mediums (Ketcham 1996a).

The IAEA (2003) states that gamma rays interact with other atoms by the photoelectric effect, Compton scattering and pair production. Compton scattering is the collision of an incident photon with an electron, preceded by the photon losing part of its energy to the electron. It is the dominant process of emission of gamma radiation in rocks, and allows for the range of gamma rays to be approximately 700m in air, and 0.5m in most rocks. The source thickness has a significant effect on the shape of the spectra; with increasing thickness there is build-up of Compton scattering. Serra (1984a) states that the effective rock sample should have a thickness of 25cm, a radius of 1m and a mass exceeding 100kg.

Groves and Campbell (1995) identify the need for stripping ratios due to spectral overlap of the three radiogenic elements (table A2.1). Stripping is the removal of the effect that one element's spectral signature has upon another. Additionally, stripping is required because of the complexity of the decay series of the decay products of uranium and thorium; whereby Bi^{214} from the uranium decay series can be detected in the thorium window.

Stripping ratios	Ratio of sensitivities	Stripping ratio
α	0.075/0.128	0.586
β	0.062/0.128	0.484
γ	0.250/0.325	0.769
a	0.011/0.325	0.034
b = *g*		0.000

Table A2.1 – Average stripping ratios used in gamma ray spectrometry. α is Th counts in the U window per Th count in the Th window. β is Th counts in the K window per Th counts in the Th window. γ is U counts in the K window per U counts

in the U window. a = U counts in the Th window per U counts in the U window. b and g are the background counts.

The Radiation Solutions INC (2008) manual for the RS-230 GRS clarifies that dead-time occurs when a radiation event is not recorded due to the machine processing a previous pulse and is 'closed' due to transferring of buffered data. Typical dead-time is approximately 5-15 μs per pulse, and can be calculated by:

$$DT = \frac{R_T - R_O}{R_T}.100\% \quad \text{(Equation A2.1)}$$

Where R_T is the true input count rate and R_O is the observed count rate. The implications of dead-time for a portable GRS involve the crystal size in the detector, however it can be determined to be negligible in the RS-230 Super-Spec GRS.

Løvborg and Mose (1987) define the net count rate (r) obtained from a GRS as:

$$r = n - b - w \quad \text{(Equation A2.2)}$$

Where *n* is the measured count rate in counts per second, *b* is the background count rate, and *w* is the interfering count rate of *j-th* element in the *i-th* element ROI. Background count rates include cosmic rays, radon gases and traces of radioactivity in the detectors photomultilpier assembly, and numerous authors articulate that background counts can be determined by undertaking an assay over a large body of water for approximately ten minutes. The IAEA (2003) defines the formula for finding the concentrations from the counts as:

$$n_i = S_{ik}C_k + S_{iU}C_U + S_{iTh}C_{Th} + n_{iBG} \quad \text{(Equation A2.3)}$$

n_i = count rate in the *i-th* energy window (cs^{-1})

S_{ij} = sensitivity of the GRS for the detection of the *j-th* element in the *i-th* energy window

C_j = concentration of the *j-th* element (% K, U ppm and Th ppm)

n_{iBG} = backround count rates in the *i-th* energy window (cs^{-1})

The sensitivity of the GRS is found by using a stripping ratio, which is the count of the *i-th* element in the *j-th* element window, per *i-th* element count in the *i-th* element window. Some average sensitivities and stripping ratios are given in table A2.2.

Sensitivities	K window	U window	Th window
counts/s per 1% K	3.36	0	0
counts/s per 1 ppm eU	0.250	0.325	0.011
counts/s per 1 ppm eTh	0.062	0.075	0.128

Table A2.2 – Average sensitivities for the i-th element in the j-th window. I.e., for 1ppm uranium there will be 0.25 cs^{-1} of K, 0.325 cs^{-1} of U and 0.011 cs^{-1} of Th. Reproduced from IAEA (2003).

A2.2 – Calibration

Conversion from the number of counts to concentrations of RHPE is far from straight forward, and several corrections and calibration routines are necessary. The Radiation Solutions Inc. RS-230 BGO Super-spec GRS requires a firmware upgrade that should theoretically render this calibration obsolete, but until we are confident with the software function in the GRS, then calibration is to be completed manually. This section presents an overview and discussion of this with regard to the portable gamma ray spectrometers owned and operated by TRaX at the University of Adelaide.

Periodic measurements at Calibration pads are useful for verifying the instruments fidelity, and any changes in the crystal sensitivity over time. Although the crystals are relatively robust, their sensitivities could change with time. Yearly calibration is recommended by Grasty and Minty (1995).

Calibration assumes a linear fit between counts recorded by the instrument and the concentrations of the radioelements in the calibration pads. Hence, measurements

where the concentrations of radioelements are significantly different to those of the calibration pads will be subject to significant error associated with extrapolation of this linear fit. For instruments calibrated against the Geoscience Australia pads this means measurements where concentrations are significantly greater than 5% K, 40 ppm U and 100 ppm Th will have large errors that are proportional to the concentration multiplied by errors in the calibration.

The spectral signature can be downloaded from the machine via the software program RS Analyst, and each assay can be copied as a text file into a spreadsheet. This raw data can then be manipulated into counts per minute, and henceforth-equivalent concentrations.

The stripping procedure makes use of stripping ratios that are determined experimentally using concrete calibration pads containing known concentrations of potassium, uranium and thorium. A minimum of four is required to determine potassium, uranium and thorium spectra and to remove the background (Grasty and Minty 1995).

In practice the equation A2.3 has four unknowns (the window sensitivities from uranium, potassium, thorium and the background), and can be reduced to a set of three equations with three unknowns by subtracting the count rates and concentrations of the blank calibration pad from those of the potassium, uranium and thorium pad. The unknown backgrounds are then removed from the computation. In matrix notation, the 3 x 3 count rate matrix **N** is then related to the concentration matrix **C** and the unknown 3 x 3 sensitivity matrix **S** by the matrix equation:

$$\begin{vmatrix} n_{K,K} & n_{K,U} & n_{K,Th} \\ n_{U,K} & n_{U,U} & n_{U,Th} \\ n_{Th,K} & n_{Th,U} & n_{Th,Th} \end{vmatrix} = \begin{vmatrix} s_{K,K} & s_{K,U} & s_{K,Th} \\ s_{U,K} & s_{U,U} & s_{U,Th} \\ s_{Th,K} & s_{Th,U} & s_{Th,Th} \end{vmatrix} \times \begin{vmatrix} c_{K,K} & c_{K,U} & c_{K,Th} \\ c_{U,K} & c_{U,U} & c_{U,Th} \\ c_{Th,K} & c_{Th,U} & c_{Th,Th} \end{vmatrix}$$

In matrix notation **N = SC**, so to calculate the sensitivity, we transpose this formula to $\mathbf{S = NC^{-1}}$, and hence to calculate the concentrations we can then use $\mathbf{C = NS^{-1}}$. For matrix multiplication processes and error propagation through these matrices, see appendix 5.

A2.3 – GRS comparative data

In the main body of the text, Figures 4.1 - 4.3 display the calibrated data for RHP, uranium and thorium values from the Eastern Ghats. Figures A2.2 – A2.4 demonstrate the pre-calibrated values of RHP, uranium and thorium.

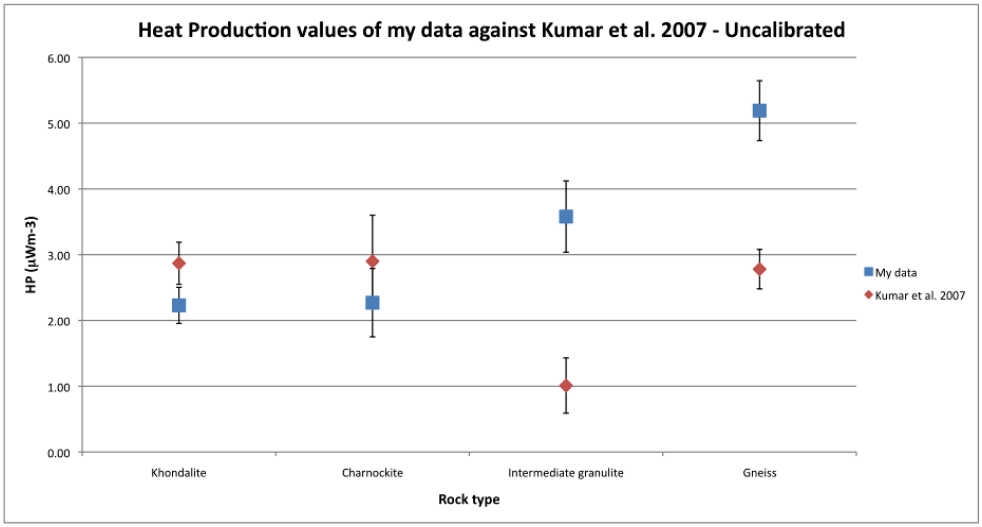

Figure A2.2 – Uncalibrated RHP from the Eastern Ghats.

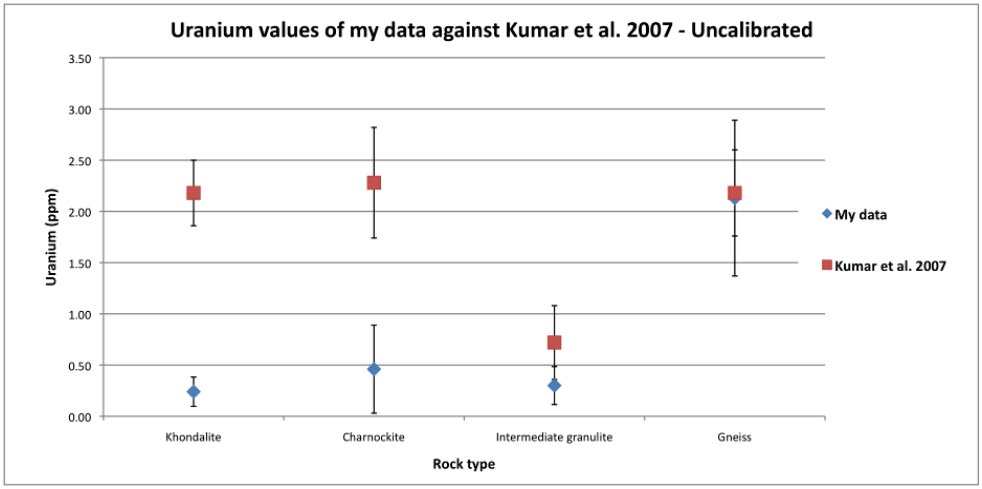

Figure A2.3 – Uncalibrated uranium from the Eastern Ghats.

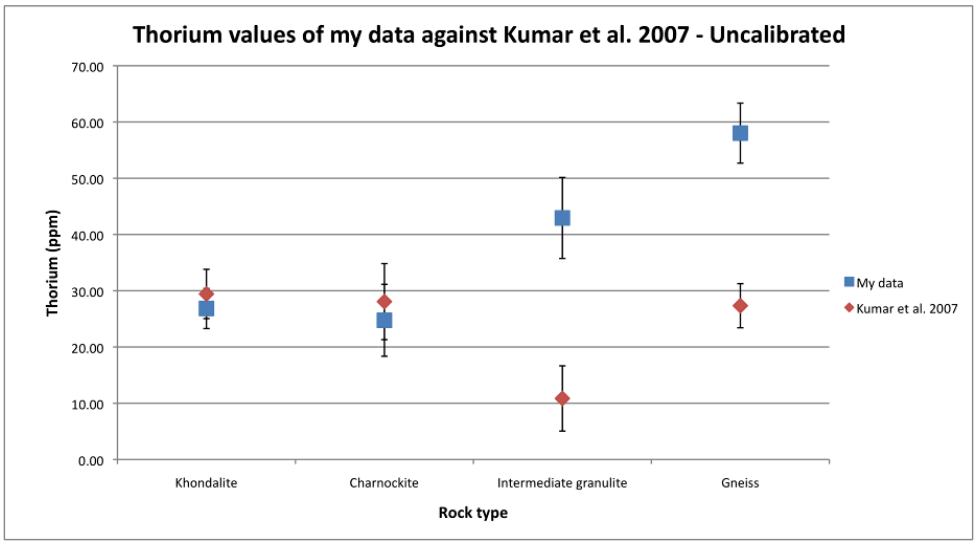

Figure A2.4 – Uncalibrated thorium from the Eastern Ghats.

A stark contrast can be made between the two sets of Figures, especially the uranium concentrations.

Further concern was raised over the inter-instrument legitimacy, due to variable readings of the exact spot in a rock formation. Figure A2.5 demonstrates this discrepancy from two machines used in Central Australia.

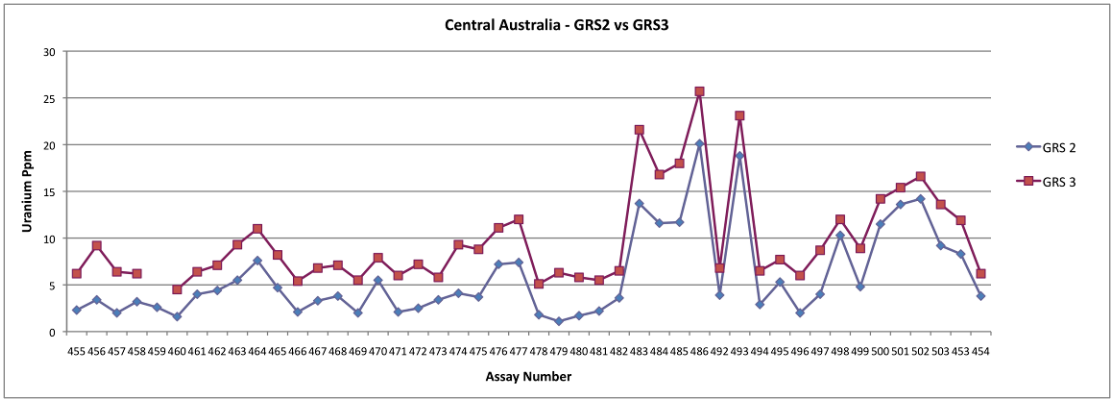

Figure A2.5 – Discrepancies between unit 2 and 3 for uranium concentrations.

Multiple ‘dummy’ assays were then recorded to cross-calibrate the instruments with each other. The results of this are displayed in Figures A2.6 – A2.11.

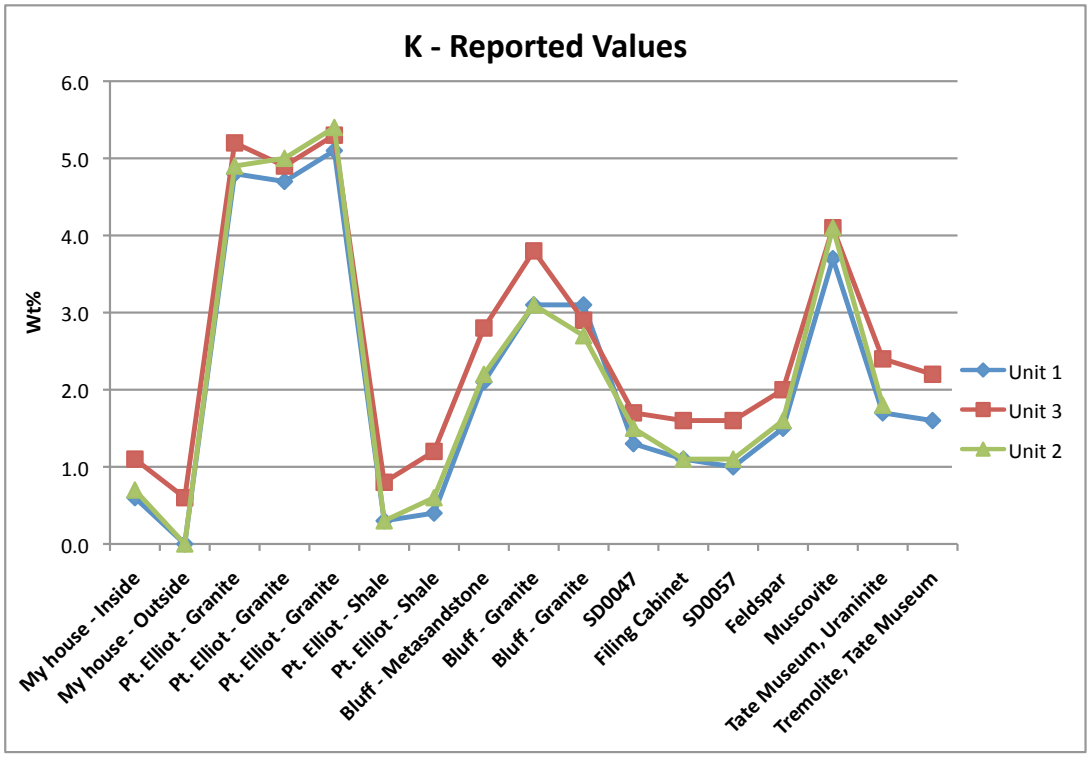

Figure A2.6 – Pre-calibrated K values. Note that there is a minor discrepancy between unit three and the other two machines.

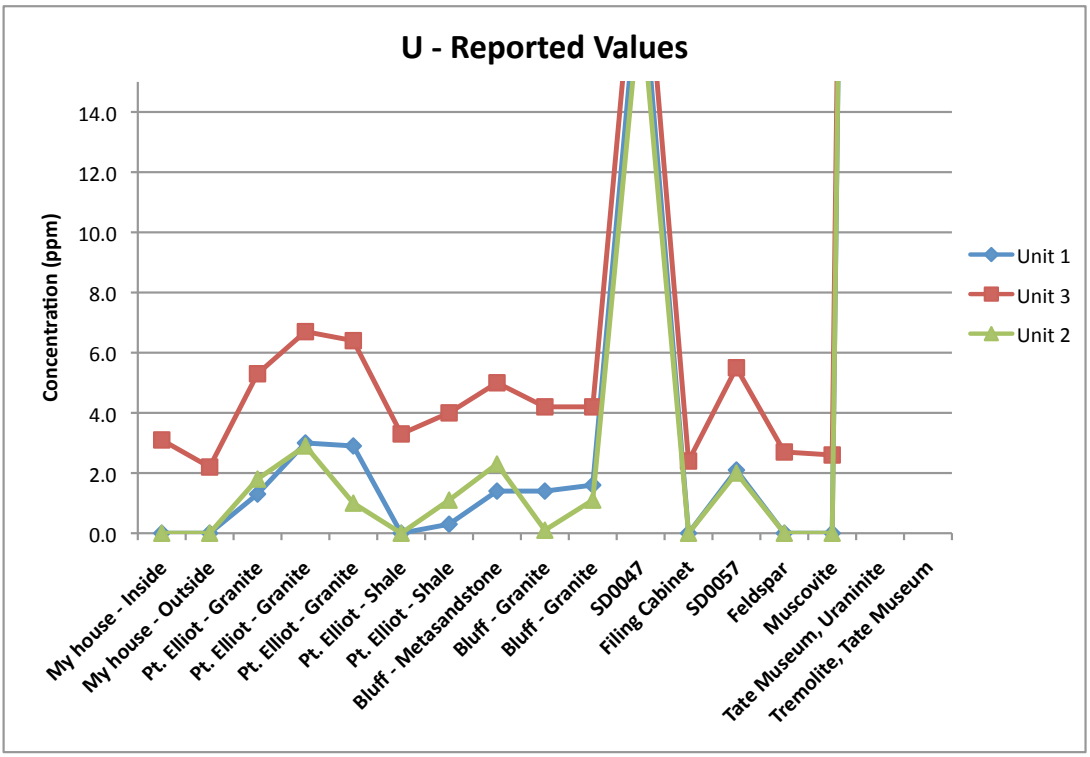

Figure A2.7 – Pre-calibrated U values. Note that there is a large discrepancy between unit three and the other two machines.

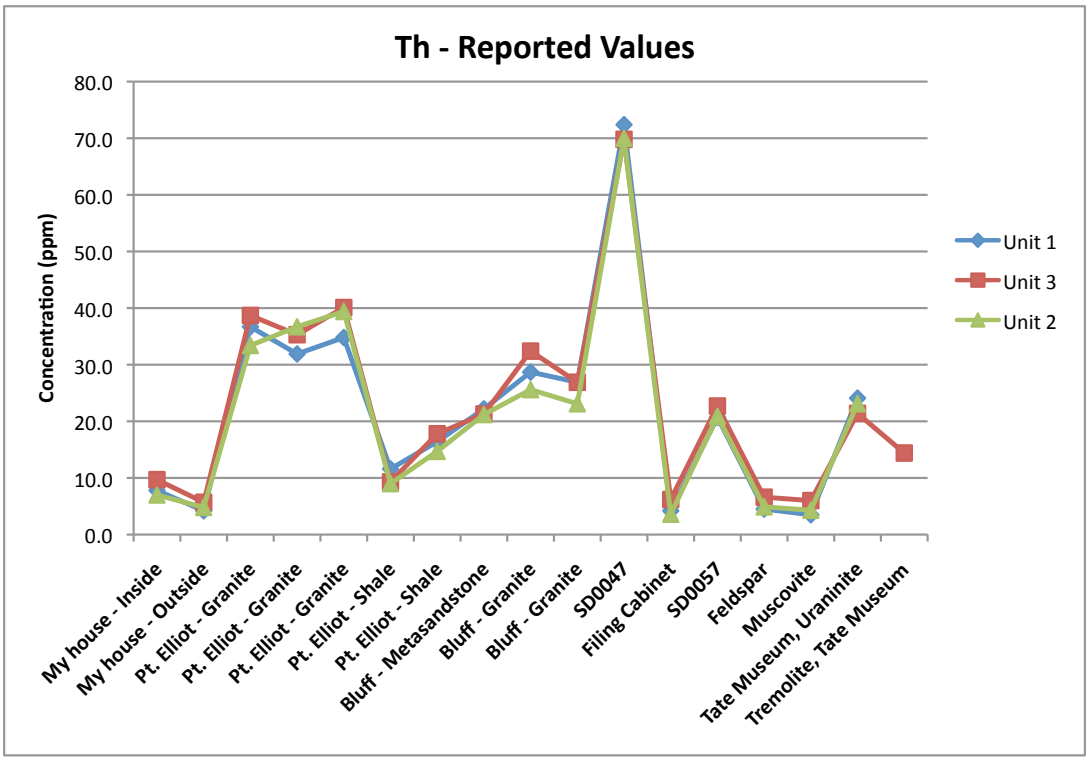

Figure A2.8 – Pre-calibrated Th values. There is no identifiable discrepancy between all three machines.

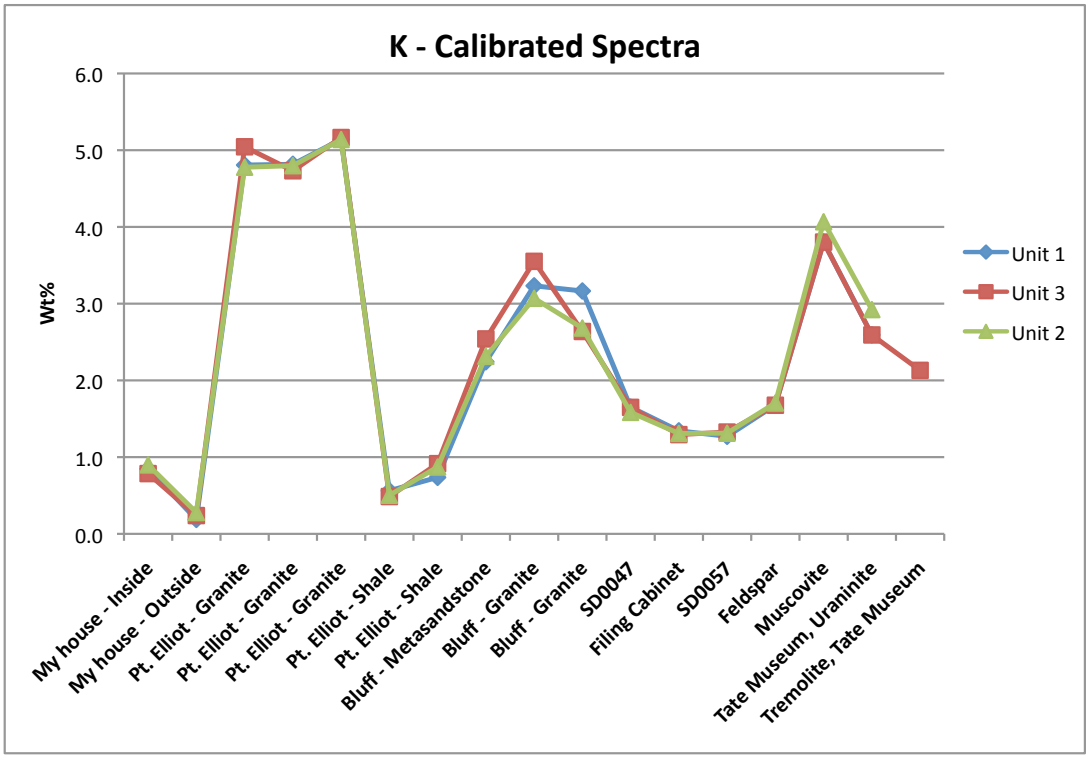

Figure A2.9 – Calibrated K values.

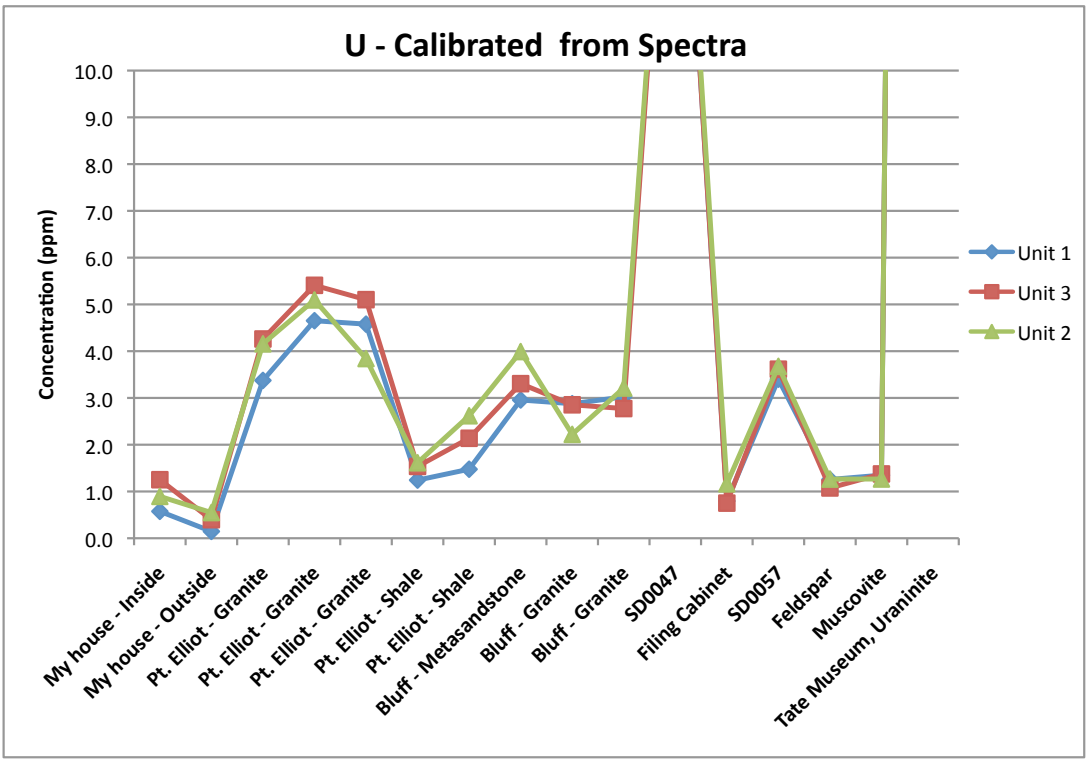

Figure A2.10 – Calibrated U values. Note the reduction in discrepancies.

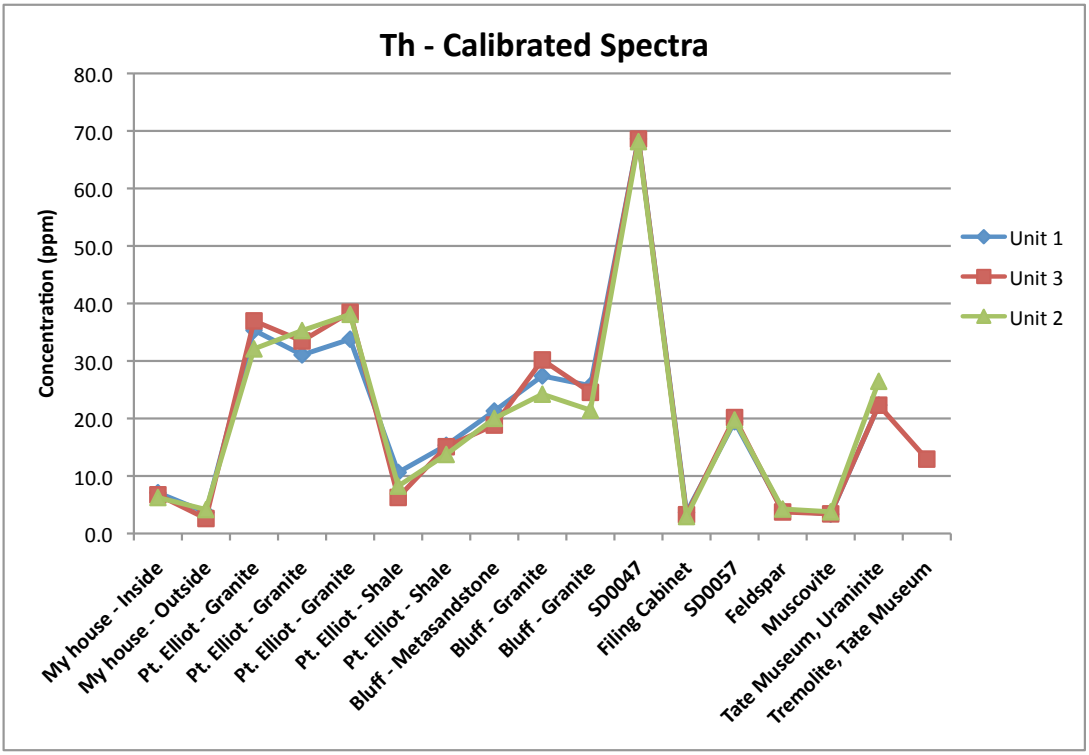

Figure A2.11 – Calibrated Th values.

A2.4 – Sensitivity analysis

Analysis of whether the volume of the sampled detected and the attenuation distance exerts an effect on the resulting concentrations has been undertaken. Figures A2.12 – A2.14 demonstrate the correlations between sample volume and concentration, Figures A2.15 – A2.17 demonstrate the effect of attenuation distance with different sample sizes from Port Elliot granites, and Figures A2.18 – A2.20 depict the effect of attenuation distance with different sample sizes from Granite Island granites.

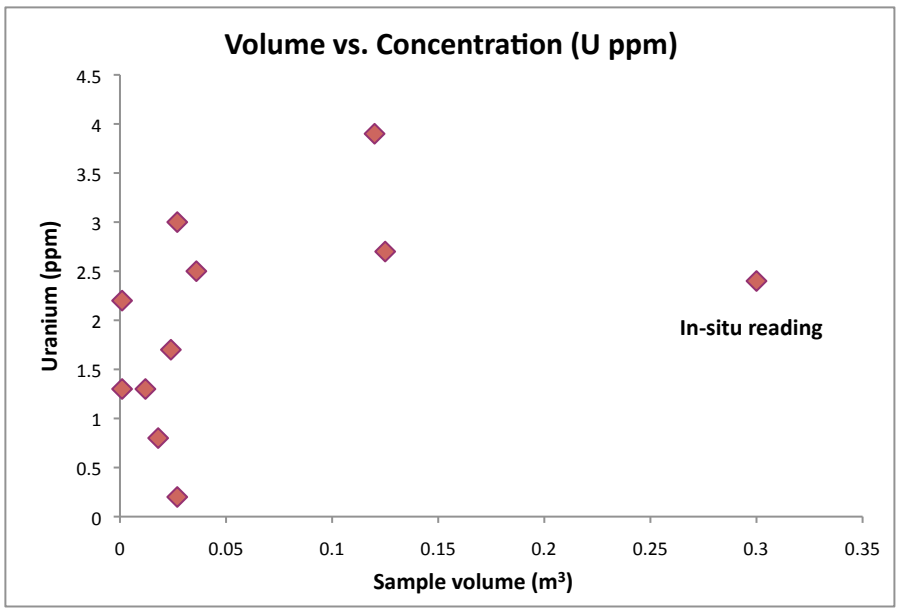

Figure 2.12 – Volume against concentration for uranium. It is possible to see that most readings of uranium are below that of the in-situ analysis, yet there are assays that resulted in higher uranium concentrations than in-situ.

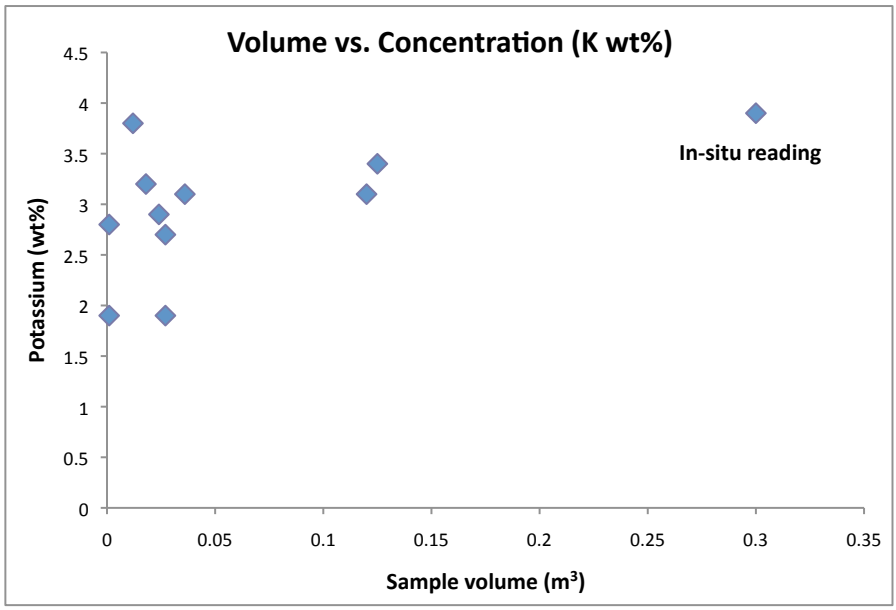

Figure 2.13 – Volume against concentration for potassium. It is evident that the in-situ reading is the highest assay recorded, leading to a conclusion that potassium in hand samples will not be detected correctly.

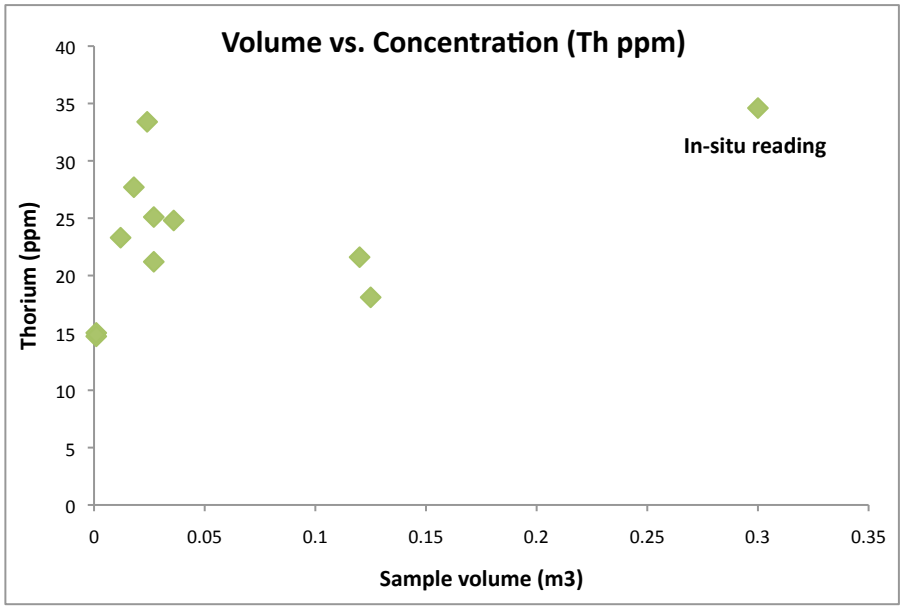

Figure 2.14 – Volume against concentration for thorium. It is evident that the in-situ reading is the highest assay recorded, leading to a conclusion that thorium in hand samples will not be detected correctly.

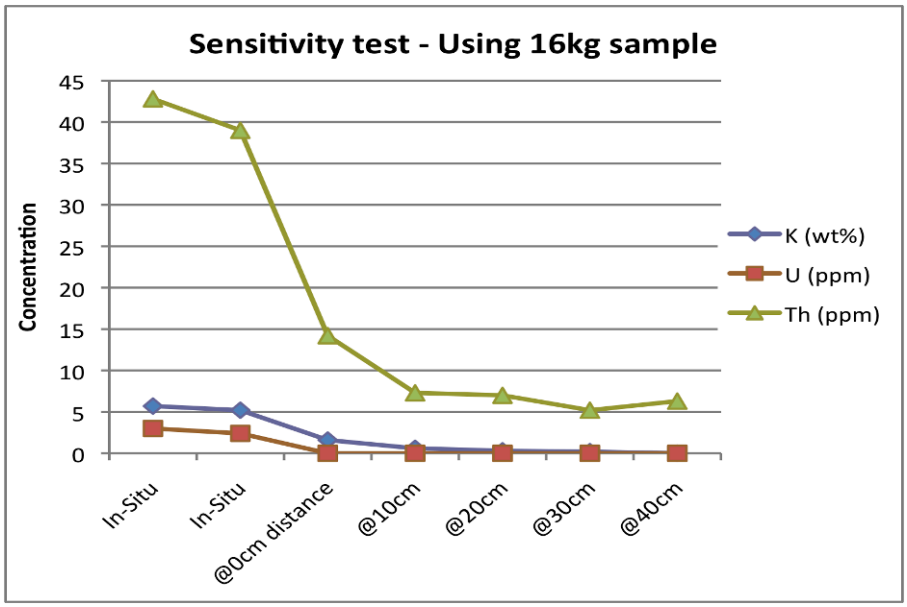

Figure A2.15 – Sensitivity anlysis of a 16kg granite (from Port Elliot), resulting in extremely lower readings when compared to the in-situ analysis. This Figure also demonstrates that the further the detector is from the sample, the lower the detected concentrations are.

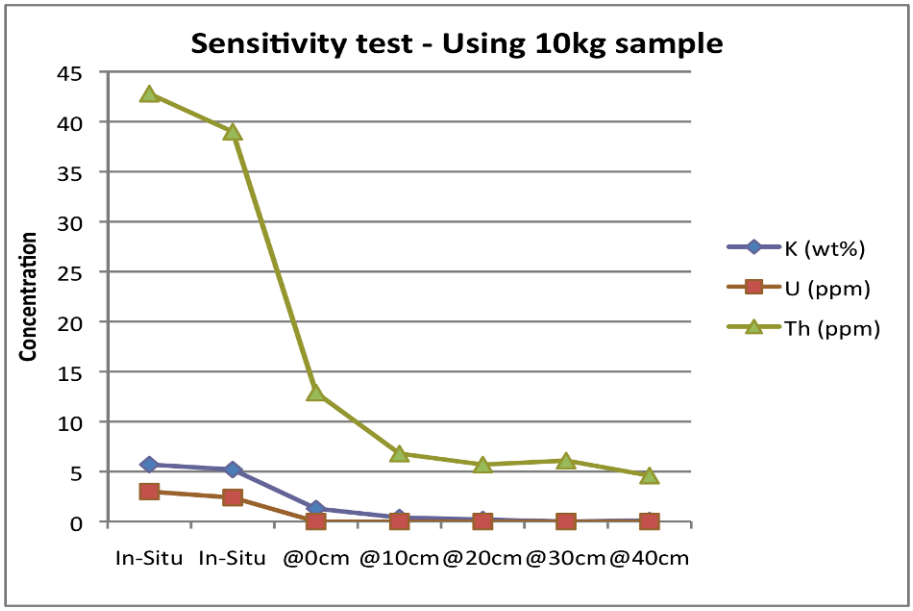

Figure A2.16 – Sensitivity anlysis of a 10kg granite (from Port Elliot), resulting in extremely lower readings when compared to the in-situ analysis. This Figure also demonstrates that the further the detector is from the sample, the lower the detected concentrations are.

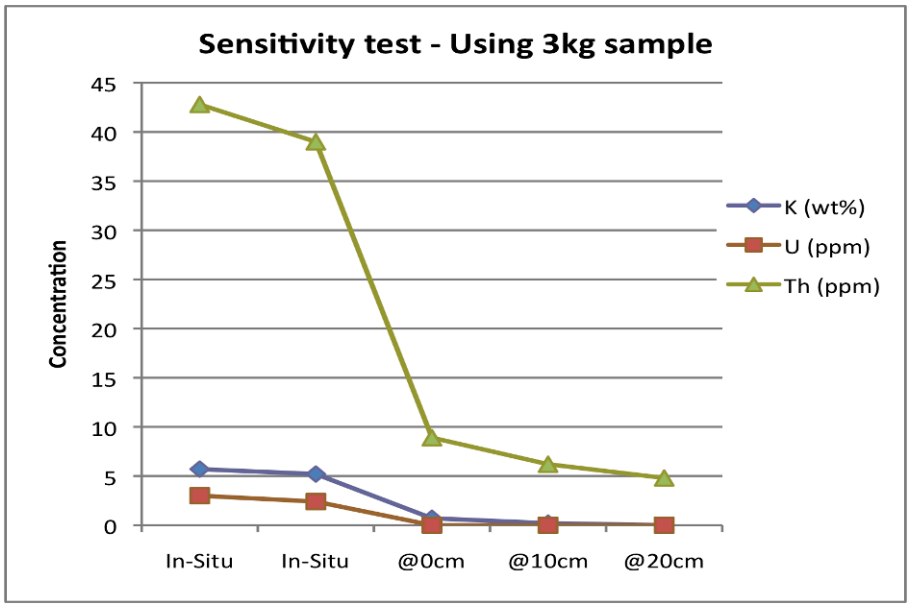

Figure A2.17 – Sensitivity anlysis of a 3kg granite (from Port Elliot), resulting in extremely lower readings when compared to the in-situ analysis. This Figure also demonstrates that the further the detector is from the sample, the lower the detected concentrations are.

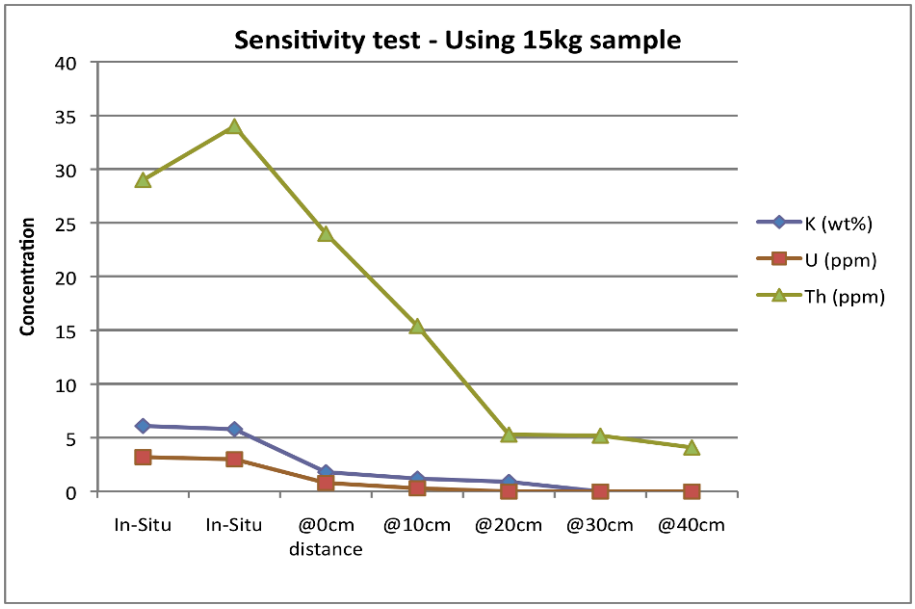

Figure A2.18 – Sensitivity anlysis of a 16kg granite (from Granite Island), resulting in significantly lower readings when compared to the in-situ analysis. This Figure also demonstrates that the further the detector is from the sample, the lower the detected concentrations are.

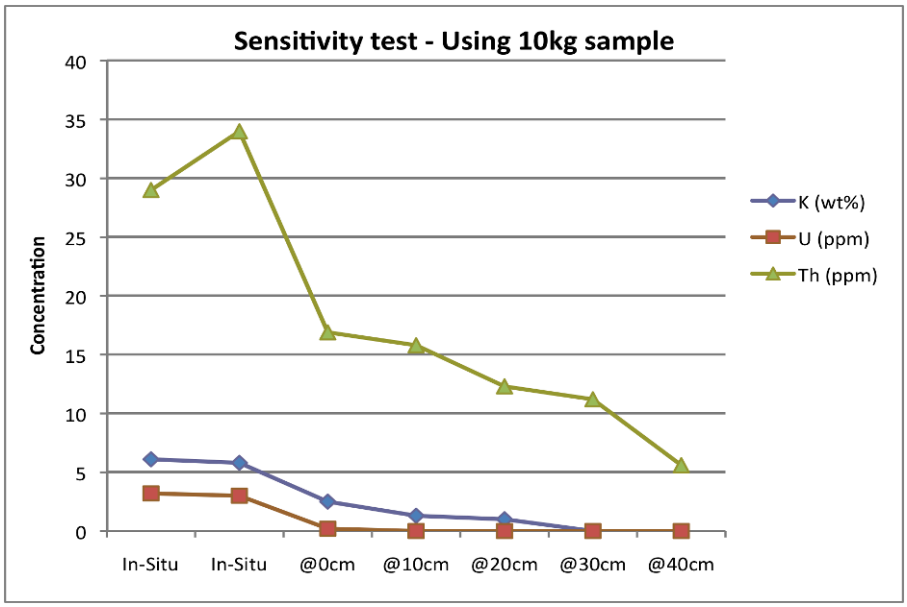

Figure A2.19 – Sensitivity anlysis of a 10kg granite (from Granite Island), resulting in significantly lower readings when compared to the in-situ analysis. This Figure also demonstrates that the further the detector is from the sample, the lower the detected concentrations are.

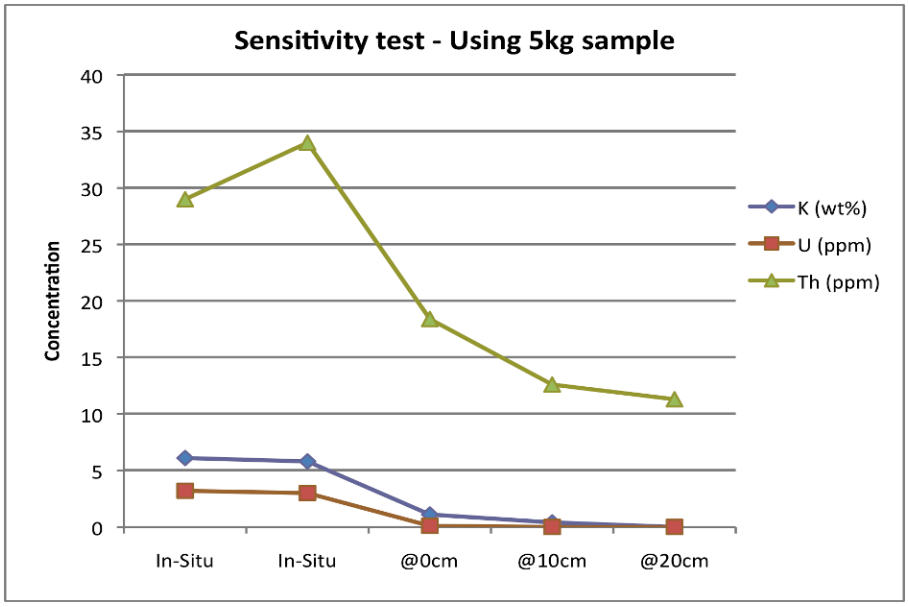

Figure A2.20 – Sensitivity anlysis of a 5kg granite (from Granite Island), resulting in significantly lower readings when compared to the in-situ analysis. This Figure also demonstrates that the further the detector is from the sample, the lower the detected concentrations are.

A2.5 – South Australian Heat Flow Anomaly 'ground correlation'

Matthews (2009) describes the South Australian Heat Flow Anomaly

(SAHFA) as a proterozoic geological region made up of high (4.01μWm^{-3}) heat

producing Gawler Range Volcanics and other various inliers, covered by low thermal conductivity sedimentary rocks. In addition Matthews & Beardsmore (2007) add heat flow data for South Australian rocks, and state that Delamerian associated granitoids produce radiogenic heat rates between 2.3 and 10.5μWm^{-3}, with the average being 5.5μWm^{-3}. Information such as this, integrated with Minty *et al*. (2009)'s Radiometric Map of Australia are the basis for a 'ground correlation' with the portable GRS, to ascertain the quality of the airborne radiometric data.

Figure 2.60 – Radiometric map of Australia, reproduced from Minty et al. (2009).

The radiometric map was manipulated to display a ternary image of the three RHPE concentrations (red = potassium, green = thorium, blue = uranium), along with a false colour image of uranium concentrations in the Arkaroola/Mt. Painter area, northern Flinders Ranges (Figure 2.61).

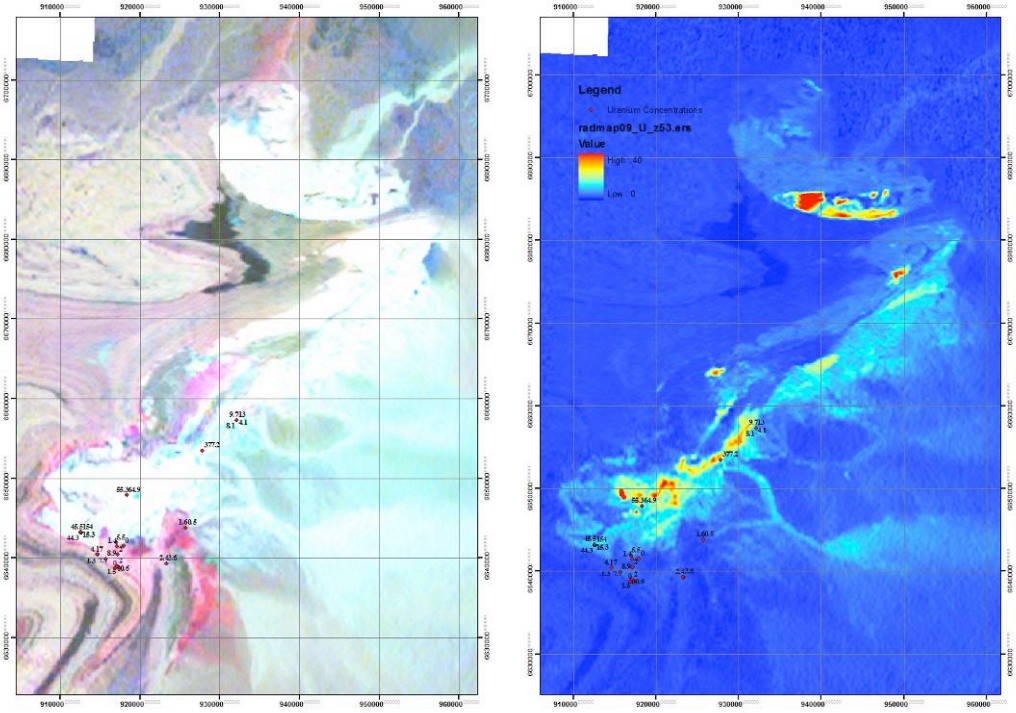

Figure 2.61 – Ternary and false colour image of the Arkaroola/Mt. Painter area. GRS uranium assay readings and locations are plotted on the maps.

The results from the portable GRS assays are plotted in table A2.6 and Figure A2.62, along with the average of the uranium concentration from the surrounding pixels at the locality. There is only a moderate correlation between the ground assays and the airborne radiometric map, which is substantially far from a one to one correlation.

Sample Number	K	±1σ	Th	±1σ	U	±1σ	Radiometrics U	Difference
305	8.7	0.5	88.4	2.5	16.0	1.1	**6.9**	**9.11**
302	5.8	0.5	107.6	2.7	16.8	1.2	**12.3**	**4.47**
298	3.5	0.6	113.1	2.8	19.0	1.3	**11.2**	**7.76**
299	1.9	0.5	98.9	2.5	23.2	1.3	**12.3**	**10.88**
297	4.4	0.6	104.2	2.6	26.0	1.4	**12.3**	**13.66**
301	5.1	0.9	177.9	4.1	44.2	2.2	**12.3**	**31.86**
303	5.3	1.0	200.0	4.5	44.7	2.4	**12.3**	**32.45**
300	5.4	1.4	171.8	4.2	139.0	4.1	**12.3**	**126.71**
318	1.8	0.1	18.9	0.8	3.8	0.4	**2.6**	**1.20**
319	1.7	0.1	10.5	0.6	4.6	0.3	**2.6**	**2.05**
314	4.9	0.2	17.6	1.0	4.3	0.5	**3.1**	**1.22**
313	6.5	0.2	14.7	1.0	4.4	0.4	**3.1**	**1.29**
312	5.8	0.2	15.0	0.8	4.5	0.4	**3.1**	**1.38**
326	5.5	0.2	2.8	0.5	3.7	0.3	**3.1**	**0.65**
328	5.7	0.2	5.5	0.5	6.2	0.3	**3.1**	**3.08**
324	3.1	0.1	13.5	0.7	8.3	0.4	**3.1**	**5.16**
323	2.8	0.1	14.0	0.7	8.8	0.5	**3.1**	**5.68**
325	4.8	0.2	16.1	0.8	16.6	0.6	**3.1**	**13.47**
327	3.7	0.3	28.2	1.4	25.7	1.1	**3.1**	**22.63**
332	0.3	0.6	119.6	3.0	7.9	1.2	**9.7**	**-1.83**
334	0.3	0.4	84.5	2.2	10.9	1.0	**9.7**	**1.16**
331	0.2	0.5	96.5	2.8	10.9	1.2	**9.7**	**1.21**
333	0.5	0.7	153.3	4.2	14.7	1.7	**9.7**	**5.03**
321	0.0	0.1	8.4	0.6	1.5	0.3	**2.3**	**-0.80**
320	0.2	0.1	6.8	0.6	2.5	0.3	**2.3**	**0.24**
311	0.7	0.1	6.5	0.5	1.7	0.3	**2.9**	**-1.17**
336	0.8	0.9	183.9	5.4	15.2	2.1	**9.7**	**5.53**
335	0.3	1.2	254.6	5.6	21.6	2.5	**9.7**	**11.88**
322	2.5	2.3	23.5	2.0	329.3	7.7	**21.8**	**307.51**
317	0.1	0.0	7.3	0.6	0.0	0.2	**2.4**	**-2.38**
310	3.3	0.2	7.2	1.3	0.5	0.5	**2.4**	**-1.92**
309	1.5	0.1	8.7	0.8	0.5	0.3	**1.9**	**-1.39**
304	0.8	0.1	5.2	0.6	2.3	0.3	**3.1**	**-0.78**
306	1.4	0.1	15.2	1.0	6.4	0.5	**6.9**	**-0.54**
307	3.4	0.7	101.3	2.6	52.6	1.9	**15.3**	**37.33**
308	1.4	0.6	82.7	3.1	59.7	2.3	**15.3**	**44.38**
329	0.7	0.1	2.3	0.4	9.0	0.4	**3.7**	**5.34**
330	0.9	0.1	2.9	0.4	10.6	0.5	**3.7**	**6.85**
315	5.0	0.2	25.5	1.0	4.5	0.4	**3.6**	**0.87**
316	6.6	0.2	19.6	1.0	8.6	0.5	**3.6**	**4.95**

Table A2.6 – 'Ground correlation' between the radiometric map and results from the portable GRS.

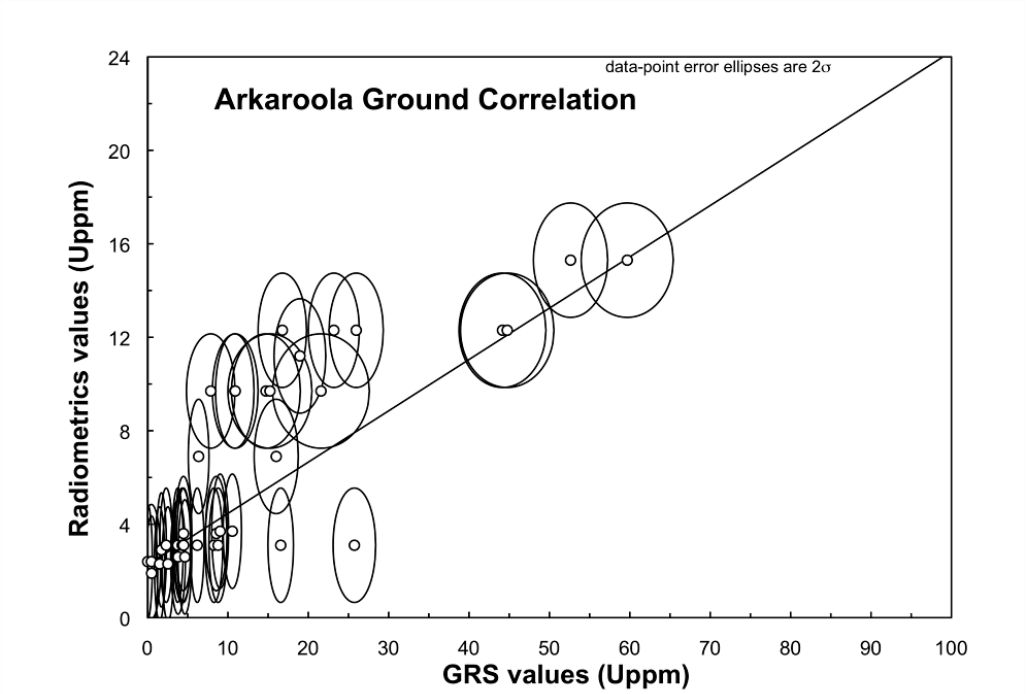

Figure 2.62 – Ground values vs. Radiometrics values, adopting a ± 1 standard deviation, to display a moderate correlation.

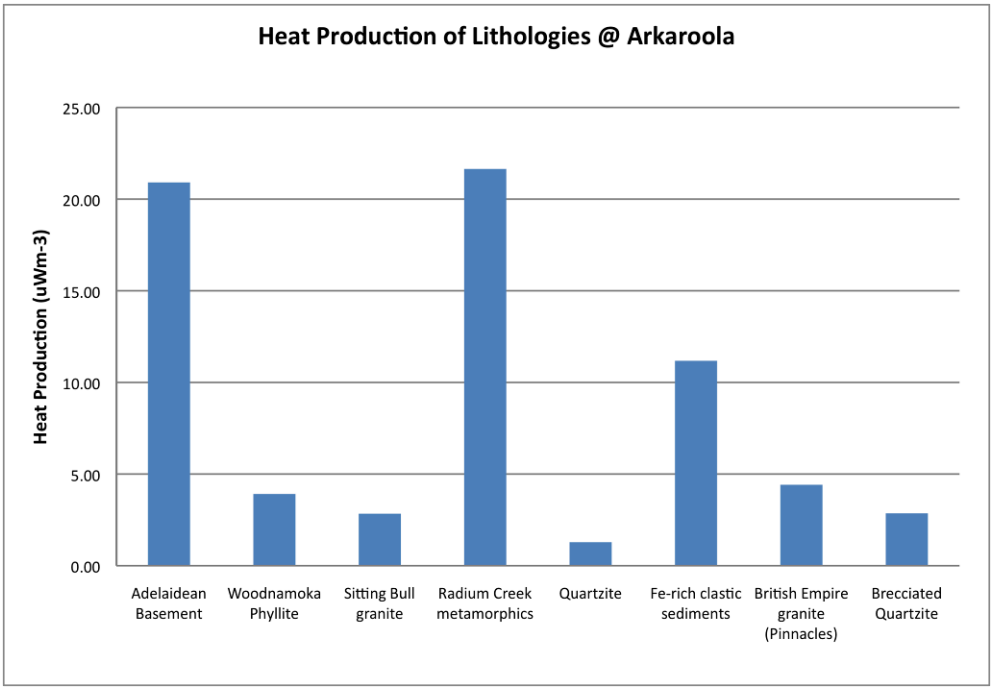

Figure 2.63 – Calculated RHP of each lithological unit at Arkaroola.

Appendix 3: Heat production data

Table A3.1 - Heat Production Measurements from the Eastern Ghats. Rows are sorted by lithology.

Heat production calculator - The Eastern Ghats

No.	Assay	K	±1s	Th	±1s	U	±1s	ΔTime (Ma)	heat from U	±1s	heat from Th	±1s	heat from K	±1s	Total HP	±1s	#	Th/U	Loc.	Rock Type
218	300	4.0	0.12	4.6	0.1	1.2	0.2	0	0.32	0.06	0.34	0.01	0.39	0.01	1.05	0.06	0.1	3.8	134	?
219	300	2.5	0.09	6.1	0.1	0.9	0.2	0	0.23	0.06	0.44	0.01	0.24	0.01	0.91	0.06	0.1	6.9	134	?
220	300	3.1	0.10	5.5	0.1	1.2	0.2	0	0.33	0.06	0.40	0.01	0.30	0.01	1.02	0.06	0.1	4.4	134	?
209	300	4.4	0.68	145.2	1.0	6.2	1.4	0	1.62	0.38	10.55	0.07	0.43	0.07	12.60	0.39	0.1	23.5	127	Bt/Qtz/Kspar enclave
240	300	2.3	0.15	24.8	0.3	4.2	0.4	0	1.11	0.11	1.80	0.02	0.23	0.01	3.14	0.11	0.1	5.8	148	Calc-Silicate
23	300	3.0	0.09	1.9	0.1	0.9	0.2	0	0.24	0.05	0.14	0.01	0.29	0.01	0.67	0.05	0.1	2.1	6	Charnockite
24	300	0.9	0.14	26.6	0.3	5.0	0.5	0	1.31	0.12	1.93	0.02	0.09	0.01	3.33	0.12	0.1	5.3	7	Charnockite
25	300	3.1	0.22	42.9	0.4	3.5	0.5	0	0.93	0.14	3.11	0.03	0.31	0.02	4.35	0.14	0.1	12.1	7	Charnockite
33	300	3.7	0.11	1.6	0.1	1.0	0.2	0	0.25	0.05	0.12	0.01	0.36	0.01	0.73	0.05	0.1	1.7	13	Charnockite
36	300	2.1	0.08	6.8	0.1	0.4	0.2	0	0.10	0.05	0.49	0.01	0.21	0.01	0.80	0.06	0.1	17.5	15	Charnockite
42	300	2.7	0.20	38.3	0.4	2.2	0.5	0	0.58	0.12	2.78	0.03	0.27	0.02	3.63	0.13	0.1	17.3	19	Charnockite
43	300	3.2	0.19	34.1	0.3	2.8	0.5	0	0.73	0.12	2.47	0.02	0.31	0.02	3.52	0.12	0.1	12.2	19	Charnockite
46	300	0.7	0.05	4.9	0.1	0.1	0.2	0	0.02	0.05	0.36	0.01	0.07	0.01	0.45	0.05	0.1	78.4	21	Charnockite
57	300	2.1	0.17	31.9	0.3	2.0	0.4	0	0.51	0.11	2.32	0.02	0.21	0.02	3.04	0.11	0.1	16.3	27	Charnockite
58	300	2.6	0.19	35.7	0.3	2.4	0.5	0	0.63	0.12	2.59	0.03	0.25	0.02	3.48	0.12	0.1	14.8	27	Charnockite
124	300	4.1	0.12	1.9	0.1	1.1	0.2	0	0.28	0.05	0.14	0.01	0.40	0.01	0.82	0.05	0.1	1.8	59	Charnockite
126	300	4.6	0.13	2.6	0.1	1.0	0.2	0	0.27	0.05	0.19	0.01	0.45	0.01	0.91	0.05	0.1	2.5	59	Charnockite
127	300	7.2	0.18	-0.6	0.0	1.9	0.2	0	0.49	0.05	-0.05	0.00	0.71	0.02	1.15	0.06	0.1	-0.3	60	Charnockite
128	300	6.2	0.19	17.4	0.2	2.7	0.3	0	0.70	0.09	1.27	0.02	0.61	0.02	2.58	0.09	0.1	6.5	60	Charnockite
133	300	0.8	0.05	-0.2	0.0	-0.6	0.1	0	-0.16	0.04	-0.02	0.00	0.08	0.00	-0.10	0.04	0.1	0.4	62	Charnockite
134	300	4.2	0.12	2.8	0.1	1.4	0.2	0	0.38	0.05	0.21	0.01	0.41	0.01	1.00	0.06	0.1	2.0	62	Charnockite
143	300	3.4	0.11	9.2	0.2	1.1	0.2	0	0.29	0.06	0.67	0.01	0.33	0.01	1.29	0.06	0.1	8.5	67	Charnockite
144	300	3.0	0.09	4.4	0.1	0.6	0.2	0	0.15	0.05	0.32	0.01	0.29	0.01	0.77	0.05	0.1	7.5	67	Charnockite
214	300	3.3	0.15	22.8	0.3	1.6	0.3	0	0.42	0.09	1.66	0.02	0.33	0.01	2.40	0.09	0.1	14.3	133	Charnockite
215	300	2.3	0.08	5.4	0.1	1.1	0.2	0	0.30	0.06	0.39	0.01	0.23	0.01	0.92	0.06	0.1	4.7	133	Charnockite
216	300	2.0	0.08	7.1	0.1	0.8	0.2	0	0.21	0.06	0.52	0.01	0.20	0.01	0.93	0.06	0.1	8.8	133	Charnockite
217	300	3.0	0.09	1.1	0.1	0.7	0.2	0	0.17	0.05	0.08	0.00	0.30	0.01	0.55	0.05	0.1	1.6	133	Charnockite
221	300	1.5	0.07	8.8	0.2	0.0	0.2	0	0.00	0.06	0.64	0.01	0.15	0.01	0.78	0.06	0.1	0.0	135	Charnockite
222	300	1.3	0.06	1.3	0.1	-0.1	0.2	0	-0.03	0.04	0.09	0.00	0.13	0.01	0.19	0.04	0.1	-9.9	136	Charnockite
224	300	1.3	0.06	2.2	0.1	-0.2	0.2	0	-0.05	0.04	0.16	0.01	0.13	0.01	0.23	0.04	0.1	-10.9	136	Charnockite
250	300	4.3	0.13	12.3	0.2	1.0	0.3	0	0.25	0.07	0.90	0.01	0.42	0.01	1.57	0.07	0.1	12.8	153	Charnockite
251	300	6.3	0.16	2.6	0.1	1.4	0.2	0	0.37	0.05	0.19	0.01	0.62	0.02	1.18	0.06	0.1	1.9	153	Charnockite
97	300	1.5	0.22	43.9	0.4	4.8	0.6	0	1.25	0.15	3.19	0.03	0.14	0.02	4.58	0.15	0.1	9.2	45	Felsic gneiss
98	300	2.4	0.30	63.6	0.5	3.2	0.7	0	0.85	0.18	4.62	0.04	0.23	0.03	5.70	0.19	0.1	19.6	45	Felsic gneiss
99	300	0.5	0.17	32.6	0.5	2.8	0.6	0	0.72	0.15	2.37	0.03	0.05	0.02	3.14	0.16	0.1	11.8	46	Felsic gneiss
100	300	2.9	0.20	33.6	0.4	3.1	0.6	0	0.80	0.15	2.44	0.03	0.29	0.02	3.53	0.15	0.1	11.0	46	Felsic gneiss
101	300	2.7	0.19	34.3	0.3	4.1	0.5	0	1.07	0.13	2.49	0.02	0.27	0.02	3.83	0.13	0.1	8.4	46	Felsic gneiss
102	300	0.1	0.12	22.8	0.3	3.1	0.4	0	0.81	0.10	1.65	0.02	0.01	0.01	2.47	0.11	0.1	7.4	46	Felsic gneiss
225	300	0.6	0.12	22.9	0.3	1.7	0.4	0	0.44	0.09	1.66	0.02	0.06	0.01	2.16	0.10	0.1	13.6	137	Felsic gneiss
226	300	0.3	0.12	24.3	0.3	2.5	0.4	0	0.67	0.10	1.77	0.02	0.03	0.01	2.46	0.11	0.1	9.6	137	Felsic gneiss
227	300	4.4	0.16	21.9	0.3	2.2	0.4	0	0.58	0.09	1.59	0.02	0.43	0.02	2.61	0.10	0.1	9.9	138	Felsic gneiss
228	300	4.7	0.13	4.1	0.1	1.3	0.2	0	0.34	0.06	0.30	0.01	0.46	0.01	1.10	0.06	0.1	3.2	138	Felsic gneiss
231	300	1.4	0.15	29.1	0.3	1.0	0.4	0	0.27	0.10	2.11	0.02	0.13	0.01	2.52	0.10	0.1	27.9	142	Felsic gneiss
237	300	5.2	0.17	18.8	0.2	2.0	0.3	0	0.54	0.08	1.36	0.02	0.51	0.02	2.41	0.09	0.1	9.2	147	Felsic gneiss
238	300	4.3	0.13	6.2	0.1	1.8	0.2	0	0.48	0.06	0.45	0.01	0.42	0.01	1.35	0.06	0.1	3.4	147	Felsic gneiss
246	300	3.9	0.12	8.1	0.2	1.2	0.2	0	0.30	0.06	0.59	0.01	0.38	0.01	1.27	0.06	0.1	7.0	152	Felsic gneiss
80	300	5.8	0.37	71.1	0.5	4.6	0.8	0	1.20	0.20	5.16	0.04	0.57	0.04	6.94	0.21	0.1	15.5	37	Felsic intrusion
79	300	5.1	0.28	52.6	0.4	3.0	0.6	0	0.78	0.15	3.82	0.03	0.50	0.03	5.10	0.16	0.1	17.7	37	Felsic vein
92	300	1.7	0.17	34.5	0.3	1.1	0.4	0	0.28	0.11	2.51	0.02	0.16	0.02	2.95	0.12	0.1	32.2	43	Gneissic quartzite
93	300	2.1	0.18	34.9	0.3	1.4	0.4	0	0.35	0.11	2.54	0.03	0.20	0.02	3.09	0.12	0.1	25.9	43	Gneissic quartzite
154	300	0.3	0.17	36.1	0.4	2.4	0.5	0	0.62	0.12	2.62	0.03	0.03	0.02	3.27	0.13	0.1	15.2	80	Gt/Sill gneiss
155	300	2.1	0.16	30.4	0.3	1.4	0.4	0	0.37	0.11	2.21	0.02	0.21	0.02	2.79	0.11	0.1	21.5	80	Gt/Sill gneiss
239	300	2.6	0.13	19.4	0.2	1.5	0.3	0	0.39	0.08	1.41	0.02	0.25	0.01	2.05	0.09	0.1	12.9	81	Gt/Sill gneiss
115	300	2.0	0.08	6.9	0.1	-0.3	0.2	0	-0.09	0.05	0.50	0.01	0.19	0.01	0.60	0.05	0.1	-20.2	53	Gt/Sill/Crd gneiss
116	300	2.7	0.09	4.0	0.1	0.4	0.2	0	0.10	0.05	0.29	0.01	0.27	0.01	0.66	0.05	0.1	10.4	53	Gt/Sill/Crd gneiss
117	300	2.3	0.08	6.2	0.1	0.1	0.2	0	0.01	0.05	0.45	0.01	0.22	0.01	0.69	0.05	0.1	114.0	53	Gt/Sill/Crd gneiss
156	300	4.1	0.20	33.3	0.3	3.3	0.5	0	0.87	0.12	2.42	0.02	0.40	0.02	3.69	0.12	0.1	10.0	81	Gt/Sill/Crd gneiss
157	300	2.9	0.15	24.9	0.3	2.1	0.4	0	0.55	0.10	1.81	0.02	0.29	0.01	2.65	0.10	0.1	11.9	81	Gt/Sill/Crd gneiss
158	300	5.3	0.30	56.4	0.5	4.2	0.6	0	1.11	0.17	4.10	0.03	0.52	0.03	5.72	0.17	0.1	13.4	81	Gt/Sill/Crd gneiss
159	300	2.7	0.28	57.2	0.5	2.2	0.6	0	0.59	0.16	4.16	0.03	0.27	0.03	5.01	0.17	0.1	25.6	81	Gt/Sill/Crd gneiss
47	300	3.6	0.11	7.3	0.1	1.2	0.2	0	0.31	0.06	0.53	0.01	0.35	0.01	1.20	0.06	0.1	6.1	22	K-spar Megacrystic granite
48	300	3.7	0.12	8.2	0.2	1.4	0.2	0	0.35	0.06	0.60	0.01	0.36	0.01	1.32	0.06	0.1	6.1	22	K-spar Megacrystic granite
49	300	3.8	0.12	7.7	0.2	1.2	0.2	0	0.30	0.06	0.56	0.01	0.38	0.01	1.24	0.06	0.1	6.6	22	K-spar Megacrystic granite
50	300	4.0	0.13	12.7	0.2	1.0	0.3	0	0.25	0.07	0.92	0.01	0.40	0.01	1.57	0.07	0.1	13.3	23	K-spar Megacrystic granite
51	300	2.7	0.12	16.9	0.2	1.4	0.3	0	0.36	0.08	1.23	0.02	0.26	0.01	1.85	0.08	0.1	12.4	24	K-spar Megacrystic granite
52	300	2.1	0.11	16.8	0.2	1.4	0.3	0	0.37	0.08	1.22	0.02	0.21	0.01	1.80	0.08	0.1	12.0	24	K-spar Megacrystic granite
54	300	3.6	0.11	8.5	0.2	1.0	0.2	0	0.26	0.06	0.62	0.01	0.35	0.01	1.23	0.06	0.1	8.6	25	K-spar Megacrystic granite
67	300	3.6	0.11	8.2	0.2	1.5	0.2	0	0.41	0.06	0.60	0.01	0.35	0.01	1.35	0.07	0.1	5.3	30	K-spar Megacrystic granite
68	300	3.4	0.11	10.0	0.2	1.7	0.3	0	0.45	0.07	0.72	0.01	0.34	0.01	1.51	0.07	0.1	5.8	30	K-spar Megacrystic granite
69	300	3.8	0.12	8.0	0.2	1.4	0.2	0	0.37	0.06	0.58	0.01	0.38	0.01	1.33	0.06	0.1	5.6	31	K-spar Megacrystic granite
70	300	3.3	0.11	6.6	0.1	1.5	0.2	0	0.40	0.06	0.48	0.01	0.33	0.01	1.21	0.06	0.1	4.3	32	K-spar Megacrystic granite
71	300	4.4	0.13	9.1	0.2	1.7	0.3	0	0.44	0.07	0.66	0.01	0.44	0.01	1.53	0.07	0.1	5.5	32	K-spar Megacrystic granite
72	300	3.5	0.11	4.0	0.1	1.1	0.2	0	0.29	0.05	0.29	0.01	0.34	0.01	0.93	0.06	0.1	3.6	33	K-spar Megacrystic granite
73	300	3.6	0.11	5.8	0.1	1.7	0.2	0	0.44	0.06	0.42	0.01	0.36	0.01	1.21	0.06	0.1	3.5	34	K-spar Megacrystic granite
135	300	3.6	0.11	6.3	0.1	0.8	0.2	0	0.20	0.06	0.46	0.01	0.35	0.01	1.01	0.06	0.1	8.2	22	K-spar Megacrystic granite
136	300	4.1	0.20	32.4	0.3	3.9	0.5	0	1.03	0.12	2.35	0.02	0.40	0.02	3.79	0.12	0.1	8.2	64	K-spar Megacrystic granite
137	300	4.2	0.19	30.7	0.3	4.2	0.5	0	1.09	0.12	2.23	0.02	0.41	0.02	3.74	0.12	0.1	7.4	64	K-spar Megacrystic granite
153	300	3.3	0.12	14.5	0.2	1.0	0.3	0	0.26	0.07	1.05	0.02	0.32	0.01	1.63	0.07	0.1	14.9	79	K-spar Megacrystic granite

160	300	2.1	0.13	22.5	0.3	1.1	0.3	0	0.28	0.09	1.64	0.02	0.21	0.01	2.12	0.09	0.1	21.2	95	K-spar Megacrystic granite
161	300	1.9	0.13	22.0	0.3	0.9	0.3	0	0.25	0.09	1.60	0.02	0.19	0.01	2.04	0.09	0.1	23.5	95	K-spar Megacrystic granite
162	300	3.2	0.10	7.1	0.1	0.8	0.2	0	0.22	0.06	0.52	0.01	0.31	0.01	1.05	0.06	0.1	8.5	96	K-spar Megacrystic granite
188	300	3.6	0.12	10.9	0.2	1.0	0.2	0	0.27	0.06	0.79	0.01	0.36	0.01	1.42	0.07	0.1	10.5	112	K-spar Megacrystic granite
190	300	3.8	0.19	31.2	0.3	2.5	0.4	0	0.65	0.11	2.26	0.02	0.38	0.02	3.30	0.12	0.1	12.5	114	K-spar Megacrystic granite
191	300	3.5	0.14	18.5	0.2	1.7	0.3	0	0.46	0.08	1.34	0.02	0.35	0.01	2.15	0.09	0.1	10.6	115	K-spar Megacrystic granite
206	300	4.4	0.65	138.8	0.9	7.0	1.3	0	1.84	0.35	10.08	0.06	0.43	0.06	12.35	0.36	0.1	19.8	127	K-spar Megacrystic granite
207	300	4.8	0.59	125.6	0.8	5.8	1.2	0	1.51	0.31	9.13	0.06	0.47	0.06	11.11	0.33	0.1	21.8	127	K-spar Megacrystic granite
208	300	5.0	0.60	128.6	0.8	5.5	1.2	0	1.45	0.32	9.34	0.06	0.50	0.06	11.29	0.33	0.1	23.2	127	K-spar Megacrystic granite
241	300	4.2	0.16	23.5	0.3	1.7	0.4	0	0.45	0.09	1.70	0.02	0.41	0.02	2.57	0.10	0.1	13.5	149	K-spar Megacrystic granite
242	300	3.9	0.15	20.6	0.3	1.0	0.3	0	0.26	0.08	1.50	0.02	0.38	0.01	2.14	0.09	0.1	21.0	149	K-spar Megacrystic granite
12	300	1.0	0.08	13.4	1.0	0.6	0.3	0	0.15	0.07	0.97	0.07	0.10	0.01	1.22	0.10	0.1	24.0	1	Khondalite
13	300	1.5	0.09	13.6	1.0	0.5	0.3	0	0.13	0.07	0.99	0.07	0.15	0.01	1.27	0.10	0.1	26.4	1	Khondalite
14	300	2.7	0.10	11.1	0.2	1.3	0.3	0	0.35	0.07	0.81	0.01	0.26	0.01	1.42	0.07	0.1	8.3	1	Khondalite
15	300	1.4	0.06	4.6	0.1	0.6	0.2	0	0.17	0.05	0.34	0.01	0.13	0.01	0.64	0.06	0.1	7.3	2	Khondalite
16	300	1.4	0.06	3.8	0.1	0.2	0.2	0	0.05	0.05	0.27	0.01	0.13	0.01	0.46	0.05	0.1	19.7	2	Khondalite
17	300	1.6	0.08	9.7	0.2	0.8	0.2	0	0.21	0.06	0.71	0.01	0.16	0.01	1.08	0.07	0.1	12.2	2	Khondalite
18	300	1.2	0.09	14.4	0.2	1.4	0.3	0	0.38	0.08	1.04	0.02	0.12	0.01	1.54	0.08	0.1	10.0	2	Khondalite
20	300	2.5	0.17	30.6	0.3	2.4	0.4	0	0.63	0.11	2.22	0.02	0.25	0.02	3.11	0.11	0.1	12.6	4	Khondalite
21	300	6.4	0.20	19.3	0.2	4.7	0.4	0	1.24	0.10	1.40	0.02	0.63	0.02	3.26	0.11	0.1	4.1	5	Khondalite
22	300	2.8	0.19	34.9	0.3	3.2	0.5	0	0.84	0.12	2.54	0.03	0.27	0.02	3.65	0.13	0.1	11.0	5	Khondalite
29	300	2.8	0.26	50.1	0.4	5.2	0.6	0	1.37	0.16	3.64	0.03	0.28	0.03	5.29	0.17	0.1	9.6	11	Khondalite
32	300	1.6	0.10	9.3	0.2	1.0	0.4	0	0.26	0.09	0.68	0.02	0.16	0.01	1.10	0.09	0.1	9.2	12	Khondalite
37	300	4.4	0.57	122.3	0.8	6.2	1.2	0	1.61	0.31	8.88	0.06	0.44	0.06	10.93	0.32	0.1	19.9	17	Khondalite
38	300	4.6	0.46	95.3	0.7	4.4	0.9	0	1.14	0.25	6.92	0.05	0.45	0.04	8.51	0.26	0.1	21.9	17	Khondalite
39	300	4.7	0.59	124.5	0.8	8.7	1.2	0	2.27	0.32	9.04	0.06	0.47	0.06	11.78	0.33	0.1	14.4	17	Khondalite
40	300	2.5	0.23	45.7	0.4	4.6	0.6	0	1.20	0.15	3.32	0.03	0.24	0.02	4.76	0.16	0.1	10.0	18	Khondalite
41	300	4.7	0.30	56.3	0.5	5.7	0.7	0	1.50	0.17	4.09	0.03	0.46	0.03	6.04	0.18	0.1	9.9	18	Khondalite
66	300	3.7	0.13	16.0	0.2	1.2	0.3	0	0.32	0.08	1.17	0.02	0.36	0.01	1.84	0.08	0.1	13.3	29	Khondalite
75	300	1.7	0.17	34.6	0.3	1.5	0.4	0	0.39	0.11	2.51	0.02	0.17	0.02	3.07	0.12	0.1	23.2	35	Khondalite
76	300	1.8	0.24	50.4	0.4	3.3	0.6	0	0.88	0.15	3.66	0.03	0.17	0.02	4.71	0.16	0.1	15.1	36	Khondalite
77	300	0.1	0.20	41.8	0.4	2.4	0.5	0	0.63	0.13	3.04	0.03	0.01	0.02	3.68	0.14	0.1	17.5	36	Khondalite
78	300	4.9	0.20	30.4	0.3	2.2	0.4	0	0.57	0.11	2.21	0.02	0.48	0.02	3.26	0.11	0.1	13.9	37	Khondalite
81	300	5.5	0.28	50.0	0.4	3.8	0.6	0	1.01	0.15	3.63	0.03	0.54	0.03	5.17	0.16	0.1	13.0	37	Khondalite
82	300	1.9	0.17	34.3	0.3	2.2	0.4	0	0.58	0.12	2.49	0.02	0.18	0.02	3.25	0.12	0.1	15.4	38	Khondalite
83	300	2.5	0.20	39.1	0.4	2.7	0.5	0	0.70	0.13	2.84	0.03	0.25	0.02	3.78	0.13	0.1	14.7	38	Khondalite
84	300	2.6	0.19	35.5	0.3	2.2	0.5	0	0.59	0.12	2.58	0.03	0.26	0.02	3.42	0.12	0.1	15.8	39	Khondalite
86	300	4.7	0.23	38.9	0.4	3.5	0.5	0	0.92	0.13	2.83	0.03	0.46	0.02	4.21	0.14	0.1	11.0	39	Khondalite
103	300	3.4	0.19	33.9	0.3	1.9	0.4	0	0.50	0.11	2.46	0.02	0.34	0.02	3.30	0.12	0.1	17.9	47	Khondalite
104	300	3.3	0.25	48.5	0.4	2.3	0.5	0	0.59	0.14	3.52	0.03	0.32	0.02	4.44	0.15	0.1	21.4	47	Khondalite
105	300	2.4	0.18	35.7	0.4	1.4	0.4	0	0.36	0.11	2.59	0.03	0.23	0.02	3.19	0.12	0.1	26.0	47	Khondalite
106	300	1.9	0.17	32.9	0.3	1.5	0.4	0	0.39	0.11	2.39	0.02	0.18	0.02	2.97	0.11	0.1	21.9	48	Khondalite
107	300	0.9	0.19	41.0	0.4	1.9	0.5	0	0.49	0.13	2.98	0.03	0.09	0.02	3.56	0.13	0.1	21.9	48	Khondalite
108	300	2.8	0.23	46.0	0.4	3.1	0.5	0	0.82	0.14	3.34	0.03	0.28	0.02	4.44	0.15	0.1	14.7	49	Khondalite
109	300	2.9	0.51	111.2	0.7	3.2	1.1	0	0.85	0.28	8.08	0.05	0.29	0.05	9.21	0.29	0.1	34.2	49	Khondalite
110	300	3.5	0.33	68.1	0.5	3.9	0.7	0	1.02	0.19	4.95	0.04	0.35	0.03	6.32	0.20	0.1	17.5	49	Khondalite
118	300	2.0	0.22	45.1	0.4	2.9	0.5	0	0.76	0.14	3.28	0.03	0.19	0.02	4.24	0.15	0.1	15.5	55	Khondalite
120	300	3.0	0.21	41.6	0.4	2.0	0.5	0	0.51	0.13	3.02	0.03	0.29	0.02	3.83	0.13	0.1	21.3	55	Khondalite
121	300	1.3	0.16	32.1	0.3	0.8	0.4	0	0.22	0.11	2.33	0.02	0.13	0.02	2.67	0.11	0.1	38.9	55	Khondalite
145	300	0.8	0.05	4.1	0.1	-0.1	0.2	0	-0.04	0.05	0.30	0.01	0.08	0.00	0.34	0.05	0.1	-30.5	76	Khondalite
146	300	1.3	0.06	6.4	0.1	-0.2	0.2	0	-0.04	0.05	0.47	0.01	0.13	0.01	0.55	0.05	0.1	-38.5	76	Khondalite
147	300	3.2	0.15	25.1	0.3	0.8	0.3	0	0.20	0.09	1.82	0.02	0.32	0.02	2.34	0.09	0.1	32.6	76	Khondalite
189	300	3.2	0.18	32.6	0.3	2.6	0.4	0	0.68	0.11	2.37	0.02	0.31	0.02	3.36	0.12	0.1	12.6	113	Khondalite
194	300	4.3	0.18	27.4	0.3	2.5	0.4	0	0.67	0.10	1.99	0.02	0.42	0.02	3.08	0.11	0.1	10.8	37	Khondalite
244	300	3.2	0.19	33.3	0.3	2.7	0.4	0	0.70	0.12	2.42	0.02	0.32	0.02	3.43	0.12	0.1	12.6	151	Khondalite
245	300	2.9	0.18	32.5	0.3	1.8	0.4	0	0.48	0.11	2.36	0.02	0.29	0.02	3.13	0.11	0.1	17.7	151	Khondalite
247	300	5.2	0.32	61.7	0.5	3.0	0.7	0	0.80	0.17	4.48	0.04	0.51	0.03	5.79	0.18	0.1	20.2	152	Khondalite
248	300	5.1	0.34	67.6	0.5	2.0	0.7	0	0.53	0.18	4.91	0.04	0.50	0.03	5.94	0.19	0.1	33.8	152	Khondalite
249	300	4.6	0.14	14.0	0.2	1.4	0.3	0	0.37	0.07	1.02	0.02	0.45	0.01	1.83	0.08	0.1	10.0	152	Khondalite
187	300	4.9	0.16	16.4	0.2	1.9	0.3	0	0.50	0.08	1.19	0.02	0.48	0.02	2.17	0.08	0.1	8.7	111	Leptynite
125	300	10.7	0.28	15.9	0.2	6.1	0.4	0	1.61	0.11	1.15	0.02	1.05	0.03	3.81	0.11	0.1	2.6	59	Leucogranite
132	300	0.5	0.05	5.6	0.1	0.0	0.2	0	0.00	0.05	0.40	0.01	0.05	0.00	0.45	0.05	0.1	-335.6	62	Mafic gneiss
223	300	1.0	0.05	-1.0	0.0	-0.2	0.1	0	-0.05	0.04	-0.07	0.00	0.10	0.00	-0.02	0.04	0.1	4.9	136	Mafic gneiss
59	300	3.1	0.16	27.8	0.3	1.8	0.4	0	0.48	0.10	2.02	0.02	0.31	0.02	2.81	0.11	0.1	15.0	28	Melted K-spar granite
60	300	2.7	0.33	70.5	0.5	2.8	0.7	0	0.72	0.19	5.12	0.04	0.27	0.03	6.11	0.20	0.1	25.5	28	Melted K-spar granite
61	300	2.6	0.41	88.2	0.6	4.6	0.9	0	1.21	0.23	6.41	0.05	0.25	0.04	7.87	0.24	0.1	19.1	28	Melted K-spar granite
62	300	4.2	0.38	79.2	0.6	3.7	0.8	0	0.96	0.21	5.75	0.04	0.42	0.04	7.13	0.22	0.1	21.6	28	Melted K-spar granite
63	300	4.2	0.27	51.5	0.4	3.5	0.6	0	0.92	0.16	3.74	0.03	0.42	0.03	5.07	0.16	0.1	14.7	28	Melted K-spar granite
64	300	2.6	0.27	56.2	0.5	2.1	0.6	0	0.56	0.16	4.08	0.03	0.25	0.03	4.90	0.17	0.1	26.3	28	Melted K-spar granite
65	300	2.6	0.40	84.7	0.6	4.3	0.9	0	1.12	0.23	6.15	0.04	0.26	0.04	7.53	0.23	0.1	19.9	28	Melted K-spar granite
138	300	2.7	0.28	58.6	0.5	3.1	0.6	0	0.82	0.17	4.25	0.03	0.26	0.03	5.34	0.17	0.1	18.7	28	Melted K-spar granite
139	300	3.7	0.38	79.2	0.6	4.0	0.8	0	1.06	0.21	5.75	0.04	0.37	0.04	7.17	0.22	0.1	19.6	28	Melted K-spar granite
94	300	1.3	0.07	5.9	0.1	0.9	0.2	0	0.25	0.06	0.43	0.01	0.13	0.01	0.80	0.06	0.1	6.3	44	Melted Khondalite
95	300	2.2	0.14	23.9	0.3	1.4	0.4	0	0.37	0.09	1.74	0.02	0.22	0.01	2.33	0.10	0.1	17.2	44	Melted Khondalite
96	300	1.4	0.07	7.7	0.2	0.5	0.2	0	0.12	0.06	0.56	0.01	0.14	0.01	0.82	0.06	0.1	16.6	44	Melted Khondalite
31	300	1.7	0.12	22.1	0.3	1.1	0.3	0	0.28	0.09	1.61	0.02	0.17	0.01	2.05	0.09	0.1	20.9	12	Metapelite
55	300	2.6	0.17	30.8	0.3	1.1	0.4	0	0.30	0.10	2.24	0.02	0.25	0.02	2.79	0.11	0.1	27.4	26	Migmatitic gneiss
56	300	1.9	0.17	32.4	0.3	1.7	0.4	0	0.44	0.11	2.35	0.02	0.19	0.02	2.98	0.11	0.1	19.3	26	Migmatitic gneiss
140	300	3.2	0.20	37.3	0.4	2.9	0.5	0	0.76	0.13	2.71	0.03	0.31	0.02	3.78	0.13	0.1	12.9	66	Migmatitic gneiss
141	300	2.0	0.18	34.6	0.3	1.3	0.4	0	0.35	0.11	2.51	0.02	0.20	0.02	3.06	0.12	0.1	26.1	26	Migmatitic gneiss

142	300	1.7	0.19	38.6	0.4	1.7	0.5	0	0.43	0.12	2.81	0.03	0.17	0.02	3.41	0.13	0.1	23.3	35	Migmatitic gneiss
74	300	5.2	0.27	50.2	0.4	3.3	0.6	0	0.86	0.15	3.65	0.03	0.51	0.03	5.02	0.16	0.1	15.3	34	Pegmatite melt vein
85	300	1.4	0.09	14.2	0.2	1.9	0.3	0	0.49	0.08	1.03	0.02	0.14	0.01	1.66	0.08	0.1	7.5	39	Qtz vein
119	300	1.6	0.19	39.2	0.4	2.2	0.5	0	0.59	0.13	2.85	0.03	0.16	0.02	3.59	0.13	0.1	17.4	55	Qtz vein
19	300	3.9	0.18	28.2	0.3	3.1	0.4	0	0.81	0.11	2.05	0.02	0.38	0.02	3.24	0.11	0.1	9.2	3	Qtz/Feldspar vein
34	300	5.8	0.62	132.7	0.8	4.9	1.2	0	1.28	0.33	9.64	0.06	0.57	0.06	11.49	0.34	0.1	27.1	13	Qtz/mica vein
89	300	0.2	0.15	31.4	0.3	1.9	0.4	0	0.50	0.11	2.28	0.02	0.02	0.01	2.81	0.12	0.1	16.4	41	Quartzite
90	300	1.1	0.21	42.9	0.4	2.6	0.5	0	0.69	0.14	3.12	0.03	0.11	0.02	3.91	0.14	0.1	16.4	42	Quartzite
91	300	0.6	0.14	29.3	0.3	2.1	0.4	0	0.56	0.11	2.13	0.02	0.05	0.01	2.74	0.11	0.1	13.6	42	Quartzite
122	300	0.0	0.08	15.4	0.2	1.8	0.3	0	0.48	0.08	1.12	0.02	0.00	0.01	1.60	0.08	0.1	8.4	58	Quartzite
123	300	0.0	0.07	12.5	0.2	0.6	0.3	0	0.15	0.07	0.91	0.01	0.00	0.01	1.06	0.07	0.1	22.1	58	Quartzite
148	300	4.9	0.78	169.6	1.0	8.1	1.6	0	2.11	0.41	12.31	0.07	0.48	0.08	14.91	0.43	0.1	21.0	77	Quartzo-feldspathic gneiss
149	300	4.9	0.64	136.9	0.9	6.6	1.3	0	1.73	0.34	9.94	0.06	0.48	0.06	12.16	0.35	0.1	20.7	77	Quartzo-feldspathic gneiss
150	300	4.4	0.50	105.1	0.7	6.0	1.0	0	1.57	0.27	7.63	0.05	0.43	0.05	9.64	0.28	0.1	17.5	77	Quartzo-feldspathic gneiss
163	300	3.6	0.29	56.7	0.5	3.7	0.6	0	0.98	0.17	4.12	0.03	0.36	0.03	5.46	0.17	0.1	15.1	97	Quartzo-feldspathic gneiss
164	300	5.0	0.49	99.8	0.7	8.8	1.0	0	2.30	0.27	7.24	0.05	0.49	0.05	10.04	0.28	0.1	11.3	97	Quartzo-feldspathic gneiss
165	300	3.9	0.29	56.9	0.5	3.5	0.6	0	0.92	0.17	4.14	0.03	0.38	0.03	5.43	0.17	0.1	16.3	97	Quartzo-feldspathic gneiss
166	300	4.4	0.23	40.2	0.4	3.9	0.5	0	1.02	0.14	2.92	0.03	0.43	0.02	4.37	0.14	0.1	10.3	97	Quartzo-feldspathic gneiss
167	300	4.3	0.24	43.9	0.4	5.0	0.6	0	1.30	0.15	3.19	0.03	0.42	0.02	4.91	0.15	0.1	8.8	97	Quartzo-feldspathic gneiss
168	300	4.5	0.26	47.5	0.4	4.8	0.6	0	1.25	0.15	3.45	0.03	0.44	0.03	5.15	0.16	0.1	10.0	98	Quartzo-feldspathic gneiss
169	300	3.0	0.23	44.0	0.4	3.1	0.5	0	0.81	0.14	3.20	0.03	0.30	0.02	4.30	0.14	0.1	14.3	98	Quartzo-feldspathic gneiss
170	300	3.5	0.15	21.2	0.3	2.0	0.3	0	0.53	0.09	1.54	0.02	0.35	0.01	2.41	0.09	0.1	10.5	99	Quartzo-feldspathic gneiss
171	300	3.1	0.34	71.1	0.5	3.5	0.7	0	0.93	0.20	5.16	0.04	0.31	0.03	6.40	0.20	0.1	20.1	99	Quartzo-feldspathic gneiss
172	300	5.7	0.18	21.6	0.3	1.5	0.3	0	0.38	0.09	1.57	0.02	0.56	0.02	2.51	0.09	0.1	14.7	100	Quartzo-feldspathic gneiss
173	300	3.4	0.15	15.5	0.3	1.0	0.4	0	0.25	0.10	1.13	0.02	0.33	0.01	1.71	0.10	0.1	16.1	100	Quartzo-feldspathic gneiss
174	300	4.4	0.36	72.0	0.5	5.1	0.7	0	1.35	0.19	5.23	0.04	0.43	0.04	7.00	0.20	0.1	14.0	101	Quartzo-feldspathic gneiss
175	300	4.0	0.14	15.2	0.2	1.5	0.3	0	0.40	0.08	1.11	0.02	0.40	0.01	1.90	0.08	0.1	9.9	102	Quartzo-feldspathic gneiss
178	300	5.0	0.36	70.0	0.5	7.9	0.8	0	2.08	0.21	5.08	0.04	0.49	0.04	7.65	0.22	0.1	8.8	106	Quartzo-feldspathic gneiss
179	300	5.0	0.34	63.9	0.5	9.8	0.8	0	2.58	0.21	4.64	0.04	0.49	0.03	7.72	0.21	0.1	6.5	106	Quartzo-feldspathic gneiss
180	300	8.3	0.34	54.4	0.5	5.4	0.6	0	1.40	0.17	3.95	0.03	0.82	0.03	6.17	0.17	0.1	10.1	106	Quartzo-feldspathic gneiss
181	300	4.7	0.44	87.8	0.6	9.1	1.0	0	2.38	0.25	6.38	0.05	0.47	0.04	9.23	0.26	0.1	9.7	107	Quartzo-feldspathic gneiss
182	300	5.3	0.49	97.6	0.7	12.3	1.1	0	3.24	0.28	7.09	0.05	0.52	0.05	10.85	0.29	0.1	7.9	107	Quartzo-feldspathic gneiss
183	300	5.2	0.32	57.8	0.5	7.9	0.7	0	2.08	0.19	4.20	0.03	0.51	0.03	6.78	0.19	0.1	7.3	107	Quartzo-feldspathic gneiss
184	300	3.5	0.27	54.1	0.5	3.0	0.6	0	0.78	0.16	3.93	0.03	0.35	0.03	5.06	0.16	0.1	18.2	108	Quartzo-feldspathic gneiss
185	300	3.3	0.17	29.7	0.3	1.7	0.4	0	0.45	0.10	2.15	0.02	0.33	0.02	2.93	0.11	0.1	17.3	108	Quartzo-feldspathic gneiss
193	300	5.0	0.22	36.8	0.4	2.7	0.5	0	0.71	0.12	2.68	0.03	0.49	0.02	3.87	0.13	0.1	13.7	117	Quartzo-feldspathic gneiss
195	300	4.5	0.22	38.2	0.4	1.6	0.5	0	0.43	0.12	2.77	0.03	0.45	0.02	3.65	0.12	0.1	23.4	119	Quartzo-feldspathic gneiss
196	300	5.2	0.19	25.2	0.3	1.9	0.4	0	0.49	0.10	1.83	0.02	0.51	0.02	2.83	0.10	0.1	13.5	119	Quartzo-feldspathic gneiss
197	300	5.0	0.25	45.5	0.4	3.1	0.5	0	0.82	0.14	3.31	0.03	0.49	0.03	4.61	0.15	0.1	14.6	120	Quartzo-feldspathic gneiss
201	300	2.8	0.32	67.1	0.5	3.9	0.7	0	1.03	0.19	4.88	0.04	0.28	0.03	6.19	0.20	0.1	17.1	128	Quartzo-feldspathic gneiss
202	300	3.0	0.38	78.6	0.6	4.9	0.8	0	1.28	0.22	5.71	0.04	0.30	0.04	7.29	0.22	0.1	16.1	128	Quartzo-feldspathic gneiss
205	300	5.0	0.27	51.1	0.4	2.6	0.6	0	0.69	0.15	3.71	0.03	0.49	0.03	4.89	0.16	0.1	19.3	129	Quartzo-feldspathic gneiss
212	300	2.9	0.14	23.5	0.3	1.2	0.3	0	0.33	0.09	1.70	0.02	0.28	0.01	2.31	0.09	0.1	18.9	132	Quartzo-feldspathic gneiss
213	300	3.1	0.15	23.3	0.3	2.3	0.4	0	0.60	0.10	1.69	0.02	0.30	0.01	2.60	0.10	0.1	10.1	132	Quartzo-feldspathic gneiss
229	300	-0.3	0.10	14.9	0.2	7.2	0.4	0	1.89	0.12	1.08	0.02	-0.03	0.01	2.95	0.12	0.1	2.1	141	Quartzo-feldspathic gneiss
230	300	0.0	0.17	35.7	0.4	1.5	0.5	0	0.40	0.12	2.60	0.03	0.00	0.02	3.00	0.12	0.1	23.7	141	Quartzo-feldspathic gneiss
232	300	1.7	0.30	63.1	0.5	5.1	0.7	0	1.34	0.19	4.59	0.04	0.16	0.03	6.09	0.19	0.1	12.4	143	Quartzo-feldspathic gneiss
233	300	1.8	0.17	31.5	0.3	3.3	0.4	0	0.86	0.12	2.29	0.02	0.17	0.02	3.32	0.12	0.1	9.6	144	Quartzo-feldspathic gneiss
234	300	2.2	0.17	31.1	0.3	3.4	0.4	0	0.90	0.12	2.26	0.02	0.21	0.02	3.37	0.12	0.1	9.1	144	Quartzo-feldspathic gneiss
235	300	3.0	0.21	40.2	0.4	3.7	0.5	0	0.98	0.14	2.92	0.03	0.30	0.02	4.20	0.14	0.1	10.7	144	Quartzo-feldspathic gneiss
236	300	2.6	0.19	35.5	0.3	2.9	0.5	0	0.76	0.12	2.58	0.03	0.25	0.02	3.59	0.13	0.1	12.3	145	Quartzo-feldspathic gneiss
243	300	4.2	0.30	60.0	0.5	3.5	0.7	0	0.93	0.17	4.36	0.04	0.42	0.03	5.71	0.18	0.1	16.9	150	Quartzo-feldspathic gneiss
186	300	0.4	0.04	2.6	0.1	-0.2	0.2	0	-0.04	0.05	0.19	0.01	0.04	0.00	0.18	0.05	0.1	-15.4	111	UHT Granulite
199	300	0.2	0.04	2.5	0.1	-0.4	0.2	0	-0.11	0.04	0.18	0.01	0.02	0.00	0.10	0.04	0.1	-6.2	128	UHT Granulite
200	300	0.7	0.05	4.5	0.1	0.7	0.2	0	0.19	0.06	0.32	0.01	0.07	0.00	0.58	0.06	0.1	6.0	128	UHT Granulite
203	300	1.2	0.06	3.3	0.1	0.3	0.2	0	0.07	0.05	0.24	0.01	0.12	0.01	0.43	0.05	0.1	12.4	129	UHT Granulite
204	300	4.4	0.15	19.3	0.2	1.2	0.3	0	0.30	0.08	1.40	0.02	0.43	0.02	2.14	0.08	0.1	16.6	129	UHT Granulite
26	300	0.0	0.18	38.5	0.4	2.9	0.5	0	0.76	0.13	2.79	0.03	0.00	0.02	3.55	0.13	0.1	13.3	8	Weathered
27	300	-0.1	0.17	37.3	0.4	1.8	0.5	0	0.49	0.12	2.71	0.03	-0.01	0.02	3.18	0.13	0.1	20.2	8	Weathered
28	300	0.9	0.15	30.4	0.3	1.5	0.4	0	0.39	0.11	2.21	0.02	0.09	0.01	2.69	0.11	0.1	20.2	9	Weathered
30	300	1.5	0.08	11.0	0.2	-0.2	0.2	0	-0.06	0.06	0.80	0.01	0.15	0.01	0.89	0.06	0.1	-48.8	11	Weathered
35	300	1.7	0.13	24.4	0.3	2.1	0.4	0	0.56	0.10	1.77	0.02	0.16	0.01	2.49	0.10	0.1	11.4	14	Weathered
44	300	0.8	0.14	29.0	0.3	1.3	0.4	0	0.34	0.10	2.10	0.02	0.08	0.01	2.52	0.11	0.1	22.4	20	Weathered
45	300	0.4	0.13	26.9	0.3	1.3	0.4	0	0.34	0.10	1.95	0.02	0.04	0.01	2.33	0.10	0.1	21.0	20	Weathered
87	300	0.9	0.22	45.5	0.4	2.5	0.5	0	0.67	0.14	3.30	0.03	0.08	0.02	4.06	0.15	0.1	17.8	40	Weathered
112	300	0.0	0.17	35.9	0.3	1.2	0.4	0	0.31	0.12	2.61	0.03	0.00	0.02	2.91	0.12	0.1	30.6	52	Weathered
113	300	0.1	0.22	49.1	0.4	1.5	0.6	0	0.39	0.14	3.56	0.03	0.01	0.02	3.96	0.15	0.1	33.3	52	Weathered
151	300	2.0	0.18	34.8	0.4	2.3	0.5	0	0.61	0.12	2.53	0.03	0.20	0.02	3.34	0.12	0.1	15.0	78	Weathered
152	300	0.6	0.13	26.4	0.3	1.2	0.4	0	0.31	0.10	1.92	0.02	0.06	0.01	2.29	0.10	0.1	22.3	78	Weathered
192	300	1.7	0.18	33.5	0.4	1.6	0.5	0	0.42	0.14	2.44	0.03	0.16	0.02	3.02	0.14	0.1	20.9	116	Weathered
210	300	0.0	0.13	27.1	0.3	2.0	0.4	0	0.52	0.10	1.97	0.02	0.00	0.01	2.48	0.11	0.1	13.8	130	Weathered
211	300	0.3	0.15	31.3	0.3	1.5	0.4	0	0.39	0.11	2.27	0.02	0.02	0.01	2.68	0.11	0.1	21.2	131	Weathered

Appendix 4: Thermal Conductivity Measurements and Data

A4.1 – Sample preparation

Samples were selected to represent the major lithological units present in the Eastern Ghats. These included charnockites, khondalites, felsic to mafic gneisses, a prevalent K-feldspar megacrystic granite and a UHT granulite. Sample locations are displayed below in A4.1, and the mineralogy for these units are outlined in appendix 1.

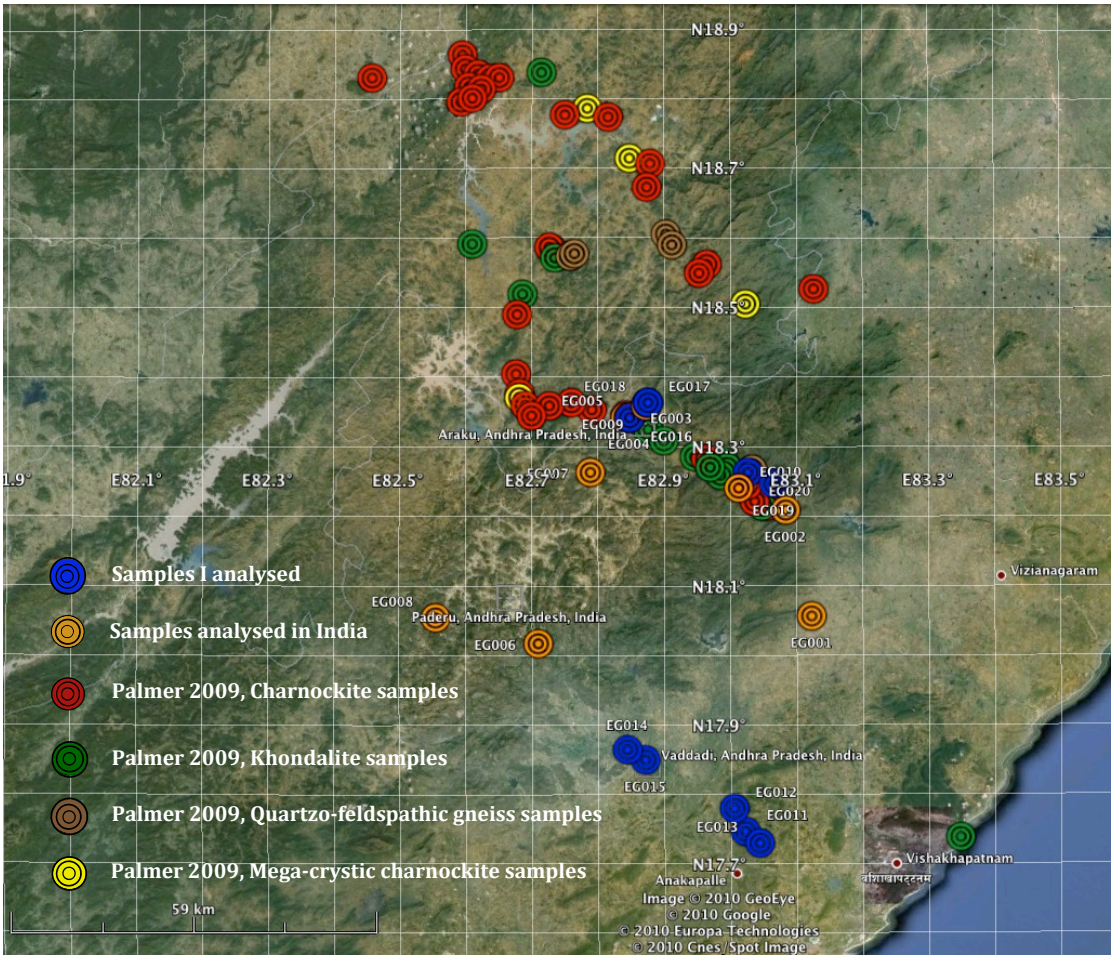

Figure A4.1 – Sample locations for thermal conductivity readings conducted in this study, and also sample locations from Palmer (2009).

Whole rock samples were collected from outcrop rather than drill-core, and immediately posed a problem of identifying the best method of cutting them to give

consistent conductivity measurements. Subsequent to conversations with Hot Dry Rocks Pty Ltd about ideal sample shapes and sizes, it became apparent that cylindrical samples were not obligatory; as the calculations took into account the samples surface area and thickness. Following this, I cut each sample into as many cubes that would allow using a 10 inch diamond–impregnated saw blade mounted on a Latham Allegro Supercut core cutting saw; making sure that each face was greater than 6.25cm^2. This process was carried out so that measurements of anisotropy could be conducted on two opposing surfaces of the sample. Some samples were cut into rectangular prisms along and against the axis of mineral lineation, because the sample geometry prevented cubes being cut. The rectangular prisms allowed for faster preparation, and still conveyed the integrity of the anisotropy ratios. Photographic records of the samples before and after cutting are set out in appendix 1.

After the samples were cut and I was confident that the faces were parallel to within <1mm, each face was thoroughly polished to ensure maximum contact with the brass plates in the PEDB. This was accomplished using the University of Adelaide's lap wheels using coarse 200-grit powder on a wet glass plate, and finished with a fine 600-grit powder.

It was recommended to me to saturate the samples in water and place in a vacuum in an autoclave for 24 hours prior to sample testing, however this process was designed for porous sedimentary rocks where thermal conductivity differs significantly due to the saturating fluids' influence. Ray *et al*. (2007) articulates that saturation of their hard and massive metamorphic samples with water prior to measurement was not considered. Concurrently, after running tests on whether this applied to my samples, I found that there was a negligible difference in thermal conductivity after saturating the samples.

The sample is smeared with a small amount of petroleum jelly on either face to allow for maximum physical contact, and foam pads were placed around the sample to minimise heat loss from the side (Figures A4.2 and A4.3).

Figure A4.2 – The vertical section of the PEDB apparatus, showing the sample in place between the two brass plates.

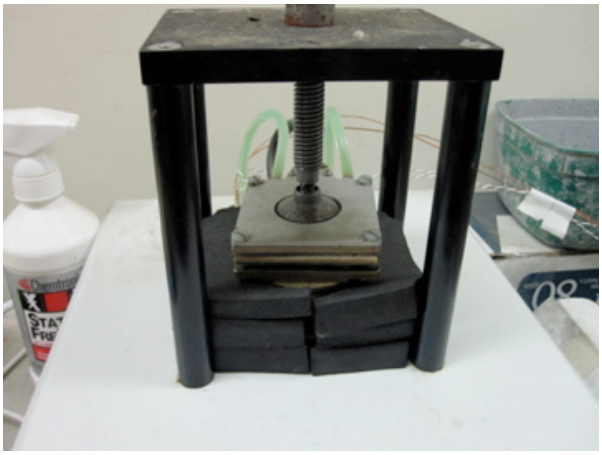

Figure A4.3 – During temperature measurements foam padding as added to the outside of the sample to reduce lateral radiative heat loss.

A4.2 – PEDB Principles

The PEDB apparatus measures thermal conductivity by computing the change in temperature across a sample using thermocouples, as a hot plate induces heat flow downwards through the sample towards a cold plate. The bar is made up in a vertical arrangement where the top and bottom sections of the bar are hollow brass cylinders, through which water is circulated. Thermostatically controlled baths maintain the

water solution flowing through the top and bottom cylindrical plates at constant temperatures of approximately 31 ^{o}C and 16^{o}C, respectively. The brass plates have low thermal conductivity polycarbonate discs inserted into the middle with two solid brass plates attached to that, with the sample in the middle, held there by a screw-type clamp plate that applies a small retaining pressure. The vertical sequence of those elements from the top is: brass disc, polycarbonate disc, brass disc, sample, brass disc, polycarbonate disc, brass disc.

Heat flows in a downward direction and temperature is measured at four points along the length of the bar assembly with four thermocouples placed in the centre of the four respective brass discs. Calculation of the unknown thermal conductivity of a sample relies on three assumptions: (1) Every pair of discs have identical thermal properties. (2) Heat conduction along the bar assembly is considered 100% efficient, with no radial loss of heat. (3) There is no thermal gradient in the brass sections of the instrument. The thermocouples are connected to a thermocouple data logger from Pico Technology, which is connected to Microsoft Excel to give a readout of the temperature difference at each second.

The following equations were supplied by the manufacturer to be used with the PEDB apparatus to calculate thermal conductivity.

$$\Delta T = \frac{(T_2 - T_3)}{(T_1 - T_2) + (T_3 - T_4)} \qquad \text{(Equation A4.1)}$$

Where ΔT is the temperature difference, and $T_1 - T_4$ are the brass plates from the upper plate to the lowest plate. The ΔT value is found from the Picolog software and entered into a spreadsheet.

The geometry of samples is measured and a hypothetical diameter is calculated (due to the fact the software is catering for cylindrical samples) by the following equation:

$$D = 2\sqrt{\frac{A}{\pi}} \qquad \text{(Equation A4.2)}$$

Where D is the diameter and A is the surface area.

The slope is given by:

$$Slope = \alpha D^2 + \beta D + \chi \qquad \text{(Equation A4.3)}$$

Where α, β and χ are constants given by the manufacturer and are shown in table A4.1.

Calibration constants		
	A =	0.5986
	B =	-86.164
	C =	6849.8
	D (25.4mm) =	-356
	D (37mm) =	-396.323
	D (48mm) =	-364.041
	D (60mm) =	-309.092

Table A4.1 – Calibration constants from manufacturer.

The 'resistance over area' is:

$$R/A = \Delta T \times slope + \delta \qquad \text{(Equation A4.4)}$$

Where δ is another constant that depends on the sample diameter.

The thermal conductivity is therefore given by:

$$k = (1 \times 10^6) \times \frac{L}{R/A \times A} \qquad \text{(Equation A4.5)}$$

Where L is the width of the sample.

A4.3 – Calibration of the PEDB

Calibration of the PEDB apparatus was essential in verifying the validity of the results obtained. Two test samples were used, one a fused silica disc of known conductivity of 1.36$Wm^{-1}K^{-1}$, the other a shale sample of conductivity 4.8$Wm^{-1}K^{-1}$.

Tests were conducted on these samples at the start of every day of testing, to ensure consistent and comparable data.

A4.4 - Taking thermal conductivity measurements

Once preparation of the sample was completed and the apparatus was calibrated, measurements were ready to be taken. First the samples' thickness and surface area were measured and entered into the a spreadsheet (table A4.2). It was then determined whether the sample would need a single (isotropic) or two measurements (anisotropic) taken. The only true isotropic rock unit was the massive charnockite, however the foliation found in the khondalites and the k-feldspar megacrystic granite was regularly hard to find, if not absent. But for the purpose of identifying an upper and lower margin of conductivity, they were classed as foliated.

The sample was placed in the PEDB apparatus, the clamp shut to finger tightness, and the Picolog software was then started. For each thermal conductivity measurement I ran the software for approximately 1200 seconds at 1 sample per second, or until the ΔT value had reached equilibrium. The last 50 values for ΔT were averaged and equations A4.1 – A4.5 were used to calculate thermal conductivity. Three repeat measurements were made for each sample, and a geometric mean was calculated. An uncertainty from the machine was calculated for each measurement, which depended on the magnitude of the ΔT value.

For each whole rock sample collected, several blocks were cut for thermal conductivity measurements, and an average geometric value was derived for each whole rock and an estimate of its standard deviations (see appendix 5 for error propagation). If there was more than one whole rock sample of a certain lithology, then an average geometric value and error were calculated, so as to produce one

conductivity estimate for the lithological unit. This value was used in the thermal conductivity plot (Figure 4.20), along with the estimated value for a comparison.

Table A4.2

Thermal conductivity calculations
Eastern Ghats - India

Calibration constants

A =	0.5986
B =	-86.164
C =	6849.8
D (25.4mm) =	-356
D (37mm) =	-396.323
D (48mm) =	-364.041
D (60mm) =	-309.092

where: ***slope*** = **A** x (diameter)^2 + **B** x (diameter) + **C**

where: **R/A** = ***slope*** x **Delta T** + **D**

Conductivity = 1000000 x **thickness** / [(**R/A**) x **surface area**]

Delta T		Uncertainty (%)
0.0	-0.5	10%
0.5	-0.9	5%
0.9	-3	3.5%
3.0	-3.5	5%
3.5	-->	10%

Sample	Thickness	Surface area	Diameter	Delta T	Slope	R/A	Conductivity	
Round sample	15	1963.495408	50	1.6	4038.1	6105	1.25	0.035
Other shape	15	1963.5	50.00005846	1.6	4038.1	6105	1.25	0.035

All values in $Wm^{-1}K^{-1}$

Sample	Delta T	Thickness (mm)	Surface area (mm)	Diameter mm	Slope	R/A	Conductivity	Uncertainty	Geometric Mean	Analytical Error	Avg of GeoMean	Total Error			Total for Charnockite Mean	Error
EG001A	1.645	25	1656	45.92	4155.4	6472	2.33	0.035					Charnockite	Massive	2.40	0.204
	1.640	25	1656	45.92	4155.4	6451	2.34	0.035	2.339	0.048						
	1.637	25	1656	45.92	4155.4	6438	2.34	0.035								
EG001B	1.700	22	1458	43.09	4248.6	6859	2.20	0.035								
	1.785	22	1458	43.09	4248.6	7220	2.09	0.035	2.188	0.104						
	1.645	22	1458	43.09	4248.6	6625	2.28	0.035			2.27	0.102				
EG001C	1.412	23	1850	48.53	4078.0	5394	2.30	0.035								
	1.412	23	1850	48.53	4078.0	5394	2.30	0.035	2.232	0.130						
	1.546	23	1850	48.53	4078.0	5940	2.09	0.035								
EG001D	1.458	24	1900	49.18	4059.9	5555	2.27	0.035								
	1.400	24	1900	49.18	4059.9	5320	2.37	0.035	2.325	0.069						
	1.426	24	1900	49.18	4059.9	5424	2.33	0.035								
EG002A	1.698	26	1750	47.20	4116.3	6626	2.24	0.035					Charnockite	Massive		
	1.625	26	1750	47.20	4116.3	6325	2.35	0.035	2.271	0.082						
	1.712	26	1750	47.20	4116.3	6683	2.22	0.035								
EG002B	1.685	25	1725	46.87	4126.4	6589	2.20	0.035								
	1.759	25	1725	46.87	4126.4	6894	2.10	0.035	2.172	0.076						
	1.672	25	1725	46.87	4126.4	6535	2.22	0.035			2.34	0.200				
EG002C	1.489	26	1690	46.39	4140.9	5802	2.65	0.035								
	1.469	26	1690	46.39	4140.9	5719	2.69	0.035	2.654	0.064						
	1.506	26	1690	46.39	4140.9	5872	2.62	0.035								
EG002D	1.482	23	1840	48.40	4081.7	5685	2.20	0.035								
	1.427	23	1840	48.40	4081.7	5460	2.29	0.035	2.252	0.066						
	1.439	23	1840	48.40	4081.7	5509	2.27	0.035								
EG004A	1.498	28	2025	50.78	4018.0	5655	2.45	0.035					Charnockite	Massive		
	1.458	28	2025	50.78	4018.0	5494	2.52	0.035	2.494	0.066						
	1.455	28	2025	50.78	4018.0	5482	2.52	0.035								
EG004B	1.249	25	1960	49.96	4039.3	4681	2.72	0.035								
	1.203	25	1960	49.96	4039.3	4495	2.84	0.035	2.690	0.172						
	1.345	25	1960	49.96	4039.3	5069	2.52	0.035			2.59	0.147				
EG004C	1.489	26	1840	48.40	4081.7	5714	2.47	0.035								
	1.412	26	1840	48.40	4081.7	5399	2.62	0.035	2.487	0.131						
	1.546	26	1840	48.40	4081.7	5946	2.38	0.035								
EG004D	1.248	25	1980	50.21	4032.6	4669	2.70	0.035								
	1.319	25	1980	50.21	4032.6	4955	2.55	0.035	2.683	0.139						
	1.208	25	1980	50.21	4032.6	4507	2.80	0.035								

003A	1.712	45	2075	51.40	4002.4	6488	3.34	0.035					Mafic Gneiss
With Foln	1.697	45	2075	51.40	4002.4	6428	3.37	0.035	3.347	0.072			
	1.720	45	2075	51.40	4002.4	6520	3.33	0.035					
003B	1.658	48	2360	54.82	3925.3	6144	3.31	0.035					
With Foln	1.692	48	2360	54.82	3925.3	6278	3.24	0.035	3.246	0.090	**3.30**	**0.058**	With Foln
	1.718	48	2360	54.82	3925.3	6380	3.19	0.035					
003C	1.598	53	2785	59.55	3841.5	5775	3.30	0.035					
With Foln	1.608	53	2785	59.55	3841.5	5813	3.27	0.035	3.298	0.071			
	1.585	53	2785	59.55	3841.5	5725	3.32	0.035					
003A	2.648	46	2100	51.71	3994.9	10214	2.14	0.035					
Against Foln	2.591	46	2100	51.71	3994.9	9987	2.19	0.035	2.119	0.097			
	2.801	46	2100	51.71	3994.9	10826	2.02	0.035					
003B	2.569	50	2455	55.91	3903.6	9664	2.11	0.035					
Against Foln	2.690	50	2455	55.91	3903.6	10137	2.01	0.035	2.141	0.163	**2.06**	**0.149**	Against Foln
	2.345	50	2455	55.91	3903.6	8790	2.32	0.035					
003C	2.865	54	2819	59.91	3836.2	10627	1.80	0.035					
Against Foln	2.519	54	2819	59.91	3836.2	9299	2.06	0.035	1.934	0.135			
	2.659	54	2819	59.91	3836.2	9836	1.95	0.035					
005A	1.498	52	2650	58.09	3864.5	5425	3.62	0.035					Granitic gneiss
With foln	1.546	52	2650	58.09	3864.5	5611	3.50	0.035	3.652	0.194			
	1.413	52	2650	58.09	3864.5	5097	3.85	0.035			**3.61**	**0.131**	With Foln
005B	1.502	53	2710	58.74	3853.9	5425	3.61	0.035					
With Foln	1.549	53	2710	58.74	3853.9	5606	3.49	0.035	3.569	0.101			
	1.498	53	2710	58.74	3853.9	5409	3.62	0.035					
005C	2.156	51	2650	58.09	3864.5	7968	2.42	0.035					
Against Foln	2.178	51	2650	58.09	3864.5	8053	2.39	0.035	2.442	0.086			
	2.069	51	2650	58.09	3864.5	7632	2.52	0.035			**2.59**	**0.174**	Against Foln
005D	1.954	53	2710	58.74	3853.9	7167	2.73	0.035					
Against Foln	1.892	53	2710	58.74	3853.9	6928	2.82	0.035	2.729	0.108			
	2.018	53	2710	58.74	3853.9	7413	2.64	0.035					
006A	1.648	51	2620	57.76	3870.1	6014	3.24	0.035					Sill/Gt gneiss
With Foln	1.594	51	2620	57.76	3870.1	5805	3.35	0.035	3.275	0.094			
	1.648	51	2620	57.76	3870.1	6014	3.24	0.035					
006B	1.945	53	2684	58.46	3858.4	7141	2.77	0.035					
With Foln	1.849	53	2684	58.46	3858.4	6770	2.92	0.035	2.765	0.159	**2.95**	**0.263**	With Foln
	2.048	53	2684	58.46	3858.4	7538	2.62	0.035					
006C	1.849	49	2513	56.57	3891.2	6831	2.85	0.035					
With Foln	1.948	49	2513	56.57	3891.2	7216	2.70	0.035	2.804	0.105			
	1.847	49	2513	56.57	3891.2	6823	2.86	0.035					
006A	2.548	51	2600	57.54	3873.9	9507	2.06	0.035					
Against Foln	2.469	51	2600	57.54	3873.9	9201	2.13	0.035	2.014	0.148			
	2.819	51	2600	57.54	3873.9	10556	1.86	0.035					
006B	2.648	50	2690	58.52	3857.4	9850	1.89	0.035					
Against Foln	2.641	50	2690	58.52	3857.4	9823	1.89	0.035	1.899	0.042	**2.06**	**0.175**	Against Foln
	2.608	50	2690	58.52	3857.4	9696	1.92	0.035					
006C	2.548	52	2489	56.29	3896.2	9564	2.18	0.035					
Against Foln	2.418	52	2489	56.29	3896.2	9057	2.31	0.035	2.252	0.077			
	2.458	52	2489	56.29	3896.2	9213	2.27	0.035					

007A	1.713	50	2450	55.85	3904.7	6325	3.23	0.035					Megacrystic Granite
With Foln	1.794	50	2450	55.85	3904.7	6641	3.07	0.035	3.194	0.127			K-spar/Gt gneiss
	1.684	50	2450	55.85	3904.7	6211	3.29	0.035					
007B	2.294	49	2365	54.87	3924.1	8638	2.40	0.035					
With Foln	2.145	49	2365	54.87	3924.1	8053	2.57	0.035	2.494	0.102	**2.91**	**0.330**	With Foln
	2.194	49	2365	54.87	3924.1	8245	2.51	0.035					
007C	1.869	53	2504	56.46	3893.1	6912	3.06	0.035					
With Foln	1.849	53	2504	56.46	3893.1	6834	3.10	0.035	3.056	0.04			
	1.901	53	2504	56.46	3893.1	7037	3.01	0.035					
007A	2.946	51	2468	56.06	3900.7	11128	1.86	0.035					
Against Foln	2.819	51	2468	56.06	3900.7	10632	1.94	0.035	1.897	0.04			
	2.895	51	2468	56.06	3900.7	10929	1.89	0.035					
007B	3.005	50	2523	56.68	3889.1	11323	1.75	0.05					
Against Foln	3.016	50	2523	56.68	3889.1	11366	1.74	0.05	1.747	0.00	**1.85**	**0.087**	Against Foln
	3.009	50	2523	56.68	3889.1	11338	1.75	0.05					
007C	2.946	54	2540	56.87	3885.7	11083	1.92	0.035					
Against Foln	2.906	54	2540	56.87	3885.7	10928	1.95	0.035	1.918	0.03			
	2.989	54	2540	56.87	3885.7	11250	1.89	0.035					
008A	1.800	52	1854	48.59	4076.5	6974	4.02	0.035					Quartzo-feldspathic gneiss
With Foln	1.850	52	1854	48.59	4076.5	7177	3.91	0.035	3.971	0.06			* Biotite - rich
	1.816	52	1854	48.59	4076.5	7039	3.98	0.035					
008B	1.746	50	1570	44.71	4194.0	6959	4.58	0.035					
With Foln	1.789	50	1570	44.71	4194.0	7139	4.46	0.035	4.591	0.14	**4.20**	**0.304**	With Foln
	1.689	50	1570	44.71	4194.0	6720	4.74	0.035					
008C	1.905	51	1649	45.82	4158.5	7558	4.09	0.035					
With Foln	1.946	51	1649	45.82	4158.5	7728	4.00	0.035	4.049	0.05			
	1.923	51	1649	45.82	4158.5	7633	4.05	0.035					
008A	2.846	50	1780	47.61	4104.5	11317	2.48	0.035					
With Foln	2.859	50	1780	47.61	4104.5	11371	2.47	0.035	2.503	0.05			
	2.765	50	1780	47.61	4104.5	10985	2.56	0.035					
008B	2.978	49	1645	45.77	4160.2	12025	2.48	0.035					
With Foln	2.916	49	1645	45.77	4160.2	11767	2.53	0.035	2.495	0.03	**2.58**	**0.129**	Against Foln
	2.978	49	1645	45.77	4160.2	12025	2.48	0.035					
008C	3.015	53	1545	44.35	4205.7	12316	2.79	0.05					
With Foln	3.056	53	1545	44.35	4205.7	12489	2.75	0.05	2.747	0.04			
	3.098	53	1545	44.35	4205.7	12665	2.71	0.05					
009A	1.269	49	2350	54.70	3927.7	4620	4.51	0.035					Quartzo-feldspathic gneiss
With Foln	1.248	49	2350	54.70	3927.7	4538	4.60	0.035	4.418	0.23			
	1.369	49	2350	54.70	3927.7	5013	4.16	0.035					
009B	1.208	50	2413	55.43	3912.9	4363	4.75	0.035					
With Foln	1.261	50	2413	55.43	3912.9	4570	4.53	0.035	4.545	0.20	**4.65**	**0.305**	With Foln
	1.308	50	2413	55.43	3912.9	4754	4.36	0.035					
009C	1.159	48	2256	53.60	3951.3	4215	5.05	0.035					
With Foln	1.169	48	2256	53.60	3951.3	4255	5.00	0.035	4.999	0.05			
	1.180	48	2256	53.60	3951.3	4298	4.95	0.035					
009A	2.018	49	2354	54.75	3926.7	7560	2.75	0.035					
With Foln	2.191	49	2354	54.75	3926.7	8239	2.53	0.035	2.614	0.12			
	2.158	49	2354	54.75	3926.7	8110	2.57	0.035					
009B	2.069	49	2384	55.09	3919.6	7746	2.65	0.035					
With Foln	1.989	49	2384	55.09	3919.6	7432	2.77	0.035	2.727	0.06	**2.75**	**0.147**	Against Foln
	1.990	49	2384	55.09	3919.6	7436	2.76	0.035					
009C	1.849	47	2280	53.88	3945.1	6930	2.97	0.035					
With Foln	1.948	47	2280	53.88	3945.1	7321	2.82	0.035	2.898	0.08			
	1.890	47	2280	53.88	3945.1	7092	2.91	0.035					

Appendix 5: Error Propagation

A5.1 General equations for error Propagation

Function	Variance
$f = aA$	$\sigma_f^2 = a^2\sigma_A^2$
$f = aA \pm bB$	$\sigma_f^2 = a^2\sigma_A^2 + b^2\sigma_B^2 \pm 2ab\,\mathrm{COV}_{AB}$
$f = AB$	$\left(\frac{\sigma_f}{f}\right)^2 = \left(\frac{\sigma_A}{A}\right)^2 + \left(\frac{\sigma_B}{B}\right)^2 + 2\frac{\sigma_A\sigma_B}{AB}\rho_{AB}$
$f = \frac{A}{B}$	$\left(\frac{\sigma_f}{f}\right)^2 = \left(\frac{\sigma_A}{A}\right)^2 + \left(\frac{\sigma_B}{B}\right)^2 - 2\frac{\sigma_A\sigma_B}{AB}\rho_{AB}$
$f = aA^{\pm b}$	$\frac{\sigma_f}{f} = b\frac{\sigma_A}{A}$
$f = a\ln(\pm bA)$	$\sigma_f = a\frac{\sigma_A}{A}$
$f = ae^{\pm bA}$	$\frac{\sigma_f}{f} = b\sigma_A$
$f = a^{\pm bA}$	$\frac{\sigma_f}{f} = b\ln(a)\sigma_A$

A5.2 - Error Propagation through matrix multiplication

For matrix multiplication, A=BC (A=m by p, B=m by n, C=n by p) is defined by:

$$a_{ij} = \sum_{k=1}^{n} b_{ik}c_{kj} \qquad \text{(Equation A.51)}$$

If the variance of the terms in B and C are known, then from the above (excluding covariance terms, as these are negligible for uncorrelated variables), it follows that the variance matrix of A (a^2) is defined by:

$$\alpha_{ij}^2 = \sum_{k=1}^{n}\left(\left(\frac{\beta_{ik}}{b_{ik}}\right)^2 + \left(\frac{\chi_{kj}}{c_{kj}}\right)^2\right)\left(b_{ik}c_{kj}\right)^2 \qquad \text{(Equation A.52)}$$

A5.3 - Error propagation during the inversion of a 3x3 symmetric matrix.

The Inverse of a matrix A, can be defined as…

A^{-1} = adjoint(A)/determinant(A).

The determinant of a 3 × 3 matrix:

$$A = \begin{bmatrix} a & b & c \\ d & e & f \\ g & h & i \end{bmatrix}$$

is given by

$$\det(A) = aei + bfg + cdh - afh - bdi - ceg. \qquad \text{(Equation A5.3)}$$

A5.4 - Error of the determinant

For each term (e.g. *aei*, absolute variance = (sum of fractional variance)*(term)^2.

Variance of det(A) for a 3 x 3 =

$$\left|\alpha^2\right| = \left(\left(\frac{\alpha_{11}}{a_{11}}\right)^2 + \left(\frac{\alpha_{22}}{a_{22}}\right)^2 + \left(\frac{\alpha_{33}}{a_{33}}\right)^2\right) * \left(a_{11}a_{22}a_{33}\right)^2 + \ldots \qquad \text{(Equation A5.4)}$$

A5.5 - Adjoint of Matrix

The Adjoint or Adjugate Matrix of a square matrix is the transpose of the *co-factors* of A.

To calculate the adjoint of matrix we follow the procedure

a) Calculate the Minor for each element of the matrix.

b) Form Cofactor matrix from the minors calculated.

c) Transpose the cofactor cofactor matrix.

For an example we will use a matrix A

$$\text{Matrix A} = \begin{vmatrix} a11 & a12 & a13 \\ a21 & a22 & a23 \\ a31 & a32 & a33 \end{vmatrix}$$

Step 1: Calculate Minors for each element

The minor for an element is the determinant of the elements that do not fall in the same row or column as the minor column of the minor element.

$$\text{Minor of a11} = M_{11} = \begin{vmatrix} a11 & a12 & a13 \\ a21 & a22 & a23 \\ a31 & a32 & a33 \end{vmatrix} = \begin{vmatrix} a22 & a23 \\ a32 & a33 \end{vmatrix} = \mathbf{a22xa33 - a32xa23}$$

$$\text{Minor of a12} = M_{12} = \begin{vmatrix} a11 & a12 & a13 \\ a21 & a22 & a23 \\ a31 & a32 & a33 \end{vmatrix} = \begin{vmatrix} a21 & a23 \\ a31 & a33 \end{vmatrix} = \mathbf{a21xa33 - a31xa23}$$

$$\text{Minor of a21} = M_{21} = \begin{vmatrix} a11 & a12 & a13 \\ a21 & a22 & a23 \\ a31 & a32 & a33 \end{vmatrix} = \begin{vmatrix} a12 & a13 \\ a32 & a33 \end{vmatrix} = \mathbf{a12xa33 - a32xa13}$$

Similarly

$M_{22} = \mathbf{a11xa33 - a31xa13}$ $M_{23} = \mathbf{a11xa32 - a31xa12}$

$M_{31} = \mathbf{a12xa23 - a22xa13}$ $M_{32} = \mathbf{a11xa23 - a21xa13}$

$M_{33} = \mathbf{a11xa22 - a21xa12}$

Step 2: Form a matrix with the minors calculated

$$\text{Matrix of Minors} = \begin{vmatrix} \mathbf{M_{11}} & \mathbf{M_{12}} & \mathbf{M_{13}} \\ \mathbf{M_{21}} & \mathbf{M_{22}} & \mathbf{M_{23}} \\ \mathbf{M_{31}} & \mathbf{M_{32}} & \mathbf{M_{33}} \end{vmatrix}$$

Step 3: Finding the cofactor from minors

Cofactor: A signed minor is called cofactor. The cofactor of the element in the i^{th} row, j^{th} column is denoted by $\mathbf{C_{ij}}$

$\mathbf{C_{ij}} = (-1)^{i+j} M_{ij}$

Matrix of Cofactors =

$C_{11} = 1 \times M_{11}$	$C_{12} = (-1) \times M_{12}$	$C_{13} = 1 \times M_{13}$
$C_{21} = (-1) \times M_{21}$	$C_{22} = 1 \times M_{22}$	$C_{23} = (-1) \times M_{23}$
$C_{31} = 1 \times M_{31}$	$C_{32} = (-1) \times M_{32}$	$C_{33} = 1 \times M_{33}$

So,

$\mathbf{C_{11}}$	$\mathbf{C_{12}}$	$\mathbf{C_{13}}$
$\mathbf{C_{21}}$	$\mathbf{C_{22}}$	$\mathbf{C_{23}}$
$\mathbf{C_{31}}$	$\mathbf{C_{32}}$	$\mathbf{C_{33}}$

=

$\mathbf{M_{11}}$	$\mathbf{-M_{12}}$	$\mathbf{M_{13}}$
$\mathbf{-M_{21}}$	$\mathbf{M_{22}}$	$\mathbf{-M_{23}}$
$\mathbf{M_{31}}$	$\mathbf{-M_{32}}$	$\mathbf{M_{33}}$

Step 4: Calculate adjoint of matrix

To calculate adjoint of matrix, transpose the cofactor matrix. i.e convert the elements in first row to first column, second row to second column, third row to third column.

Adjoint of Matrix =

$\mathbf{C_{11}}$	$\mathbf{C_{21}}$	$\mathbf{C_{31}}$
$\mathbf{C_{12}}$	$\mathbf{C_{22}}$	$\mathbf{C_{32}}$
$\mathbf{C_{13}}$	$\mathbf{C_{23}}$	$\mathbf{C_{33}}$

To find the inverse divide all the terms by the determinan.

A5.6 - Errors on the Adjoint

Errors on the adjoint are equivalent to the errors on the determinant of the 2 by 2 matrix that was used to form the element minors.

Hence, the variance of the minors m^2

$$\mu_{ij}^2 = \left(\left(\frac{\alpha_{km}}{a_{km}}\right)^2 + \left(\frac{\alpha_{\ln}}{a_{\ln}}\right)^2\right) * \left(a_{km}a_{\ln}\right)^2 + \left(\left(\frac{\alpha_{lm}}{a_{lm}}\right)^2 + \left(\frac{\alpha_{kn}}{a_{kn}}\right)^2\right) * \left(a_{lm}a_{kn}\right)^2,$$

$$Where \quad l \neq i \neq k, k \neq l, and \quad m \neq j \neq n, m \neq n, \qquad \text{(Equation A5.5)}$$

Therefore the variances of the inverse are given by…

$$\alpha_{ij}^2 = \left(\frac{\mu_{ji}^2}{m_{ji}^2} + \frac{\det(\alpha^2)}{\det(A)^2} \right) * \left(\frac{m_{ji}}{\det(A)} \right)^2$$

(Equation A5.6)